

# Exploration of Fluxonium Parameters for Capacitive Cross-Resonance Gates

Eugene Y. Huang<sup>1,\*</sup> and Christian Kraglund Andersen<sup>1,†</sup>

<sup>1</sup>*QuTech and Kavli Institute of Nanoscience, Delft University of Technology, 2628 CJ, Delft, The Netherlands*  
(Dated: March 19, 2026)

We study the cross-resonance effect in capacitively-coupled fluxonium qubits and devise a simple formula for their maximum  $ZX$  interaction strength. By going beyond the perturbative regime, we find that a CNOT gate can generally be realized in under 200 ns with residual  $ZZ$  limited to 50 kHz, for fluxonium qubits with frequencies below 1 GHz. Our analysis relies on a semi-analytical method: we first numerically diagonalize the Floquet Hamiltonian of the strongly-driven control qubit and then perturbatively incorporate the weak qubit-qubit coupling to obtain an effective Hamiltonian. We also derive frequency collision windows around harmful control-target and control-spectator transitions. For large fluxonium devices, we predict a collision-free yield that is considerably less sensitive to junction variability compared to transmons in the same layout. These results support the viability of an all-fluxonium cross-resonance architecture with only capacitive couplings.

## I. INTRODUCTION

Superconducting qubits are an established platform for quantum information processing. To date, the most common architectures are based on the transmon qubit [1], with the largest devices integrating over a hundred such qubits on a single chip [2–4]. However, native gate errors necessitate the use of error-correction protocols to build fault-tolerant logical qubits from a large number of physical qubits [3–7]. Given current error rates, running useful quantum algorithms would require millions of physical qubits [8–10] and it remains unclear how this could be realized with existing technology [11–13]. Further improvements to gate fidelity and architectural scalability could significantly reduce the overhead for quantum error correction and advance the prospects for future fault-tolerant quantum computers, motivating the continued research into alternative superconducting qubits [14–21].

The fluxonium qubit is one such alternative that has seen rapid adoption, thanks in part to its compatibility with transmon-style circuit-QED designs [22, 23], using the same capacitively coupled resonator for dispersive readout [26, 27] and a single-axis drive for qubit control [28, 29]. Single- and two-qubit gates have recently been demonstrated on fluxonium qubits with errors below  $10^{-3}$  [29–32], matching the performance of the best two-qubit transmon devices [33, 34]. Additionally, the highly nonlinear fluxonium potential confers a large anharmonicity that can mitigate leakage and, thus, improve error-correction performance [4, 35]. Further benefits of the fluxonium qubit include reduced dielectric loss due to its smaller charge dipole moment [23–25], and suppressed Purcell decay into its readout resonator, owing to its typically sub-gigahertz qubit frequency [36, 37].

Existing fluxonium processors are, however, largely confined to two-qubit systems while experimental and theoretical work continues to explore the most effective

strategies for scaling, leveraging tunable interactions [38–41], auxiliary coupler states [31, 42–47] or even hybrid architectures combining both fluxoniums and transmons [45, 48]. On the other hand, the most straightforward two-qubit gate schemes require only fixed direct couplings, with static interactions activated by microwave drives or baseband flux pulses [32, 49–55], a strategy also favored in earlier generations of transmon processors [61–66]. We consider flux pulsing undesirable as it displaces the fluxonium from its half-flux bias point (where its spectrum is symmetric), leaving it sensitive to dephasing from flux noise [51, 67]. Moreover, baseband flux pulses are often severely distorted as they propagate towards the qubit, necessitating careful characterization and precompensation [68, 69]. Drive-activated interactions, on the other hand, are relatively easy to calibrate and preserve the qubits at their operational bias point.

Among the possible drive-activated gates between qubits with fixed couplings, the cross-resonance (CR) gate is, arguably, the simplest in terms of implementation [53–60]. In the CR gate, both qubits are driven at the resonance frequency of one qubit in the pair, reusing the single-axis drive lines shared with single-qubit control. This hardware-efficient architecture was used to realize a record 1121 transmon qubits on a single chip [70]. However, the small anharmonicity inherent to transmons lead eventually to unavoidable frequency collisions, impeding further scaling of this architecture [72, 73]. Given the fluxonium qubit’s significantly higher anharmonicity, a natural question to ask is whether the CR architecture is implementable with fluxoniums and how large such devices could scale.

The CR gate can be applied between fluxonium qubits coupled either capacitively or inductively [32, 49]. While inductive coupling offers a larger on-off ratio for the effective two-qubit interaction, it is difficult to engineer in a scalable manner due to the small size of typical flux loops [23, 32, 52]. In comparison, the capacitor pads of a fluxonium, while smaller than those of transmons, can easily interface with coupling elements [31, 43]. For this reason, we focus on capacitive couplings, despite their theoretical drawbacks, with the aim of exploring the potential of

\* e.y.huang@tudelft.nl

† c.k.andersen@tudelft.nl

the *simplest* multi-fluxonium design.

The rest of the paper is organized as follows. In Section II, we introduce the model Hamiltonian that forms the basis of our analysis, consisting of two capacitively coupled fluxonium qubits with one qubit driven and the other idle. In Section III, we determine the maximum speed at which two-qubit gates can be performed while keeping residual always-on interactions below an acceptable threshold. Our semi-analytical approach allows us to investigate the dynamics under strong CR drives beyond the perturbative regime, where we observe a universal saturation in the effective two-qubit interaction strength. This observation enables us to empirically derive a simple yet accurate formula for the minimum time required to implement a CNOT gate, valid for strong drive amplitudes. In Section IV, we analyze the primary sources of unintentional resonances, including from spectator qubits, that can induce coherent errors during the CR gate and determine the minimum detuning required to suppress them. These detuning windows are then used in Monte Carlo simulations to calculate the probability of zero frequency collisions in a qubit lattice as a function of system size.

## II. MODEL

The CR effect is a drive activated two-qubit interaction between two transversely coupled qubits. For superconducting qubits, this transverse coupling can be either capacitive or inductive. Specifically, one of the qubits, called the *control*, is driven at the frequency of its coupled neighbor, called the *target*. The resulting interaction rotates the target qubit with a Rabi rate conditional on the state of the control qubit, naturally generating the CNOT gate up to single-qubit gates.

We are interested in the case of pure, direct capacitive coupling, which we model using the Hamiltonian ( $\hbar = 1$ )

$$\hat{H}(\Omega, t) = \hat{H}_c(\Omega, t) + \hat{H}_t + J \hat{n}_c \otimes \hat{n}_t, \quad (1)$$

where  $\hat{H}_c(\Omega, t)$  and  $\hat{H}_t$  act on, respectively, the control and target qubits,  $\Omega$  is the CR drive amplitude,  $J$  is the capacitive coupling strength and  $\hat{n}_q$  is the charge operator of qubit  $q$ . The individual Hamiltonians are

$$\hat{H}_c(\Omega, t) := \hat{H}_c^{\text{idle}} + \Omega \sin(\omega_d t) \hat{n}_c, \quad (2)$$

$$\hat{H}_t := \hat{H}_t^{\text{idle}}, \quad (3)$$

where  $\hat{H}_q^{\text{idle}} = \sum_j E_q^j |j\rangle\langle j|$  is the diagonalized fluxonium Hamiltonian. We refer to the states  $\{|j\rangle\}_{j \in \mathbb{N}_0}$  (where  $\mathbb{N}_0 = \{0, 1, 2, \dots\}$ ) as the bare basis, with corresponding energies  $\{E_q^j\}_{j \in \mathbb{N}_0}$  for qubit  $q$ . We allow the drive amplitude  $\Omega$  to be time-dependent, and write it as  $\Omega(t)$  to indicate this explicitly when needed. No generality is lost by assuming the control qubit is capacitively driven. We show in Appendix A that, in the context of this work, capacitive and inductive driving are equivalent up to a rescaling of drive amplitude.

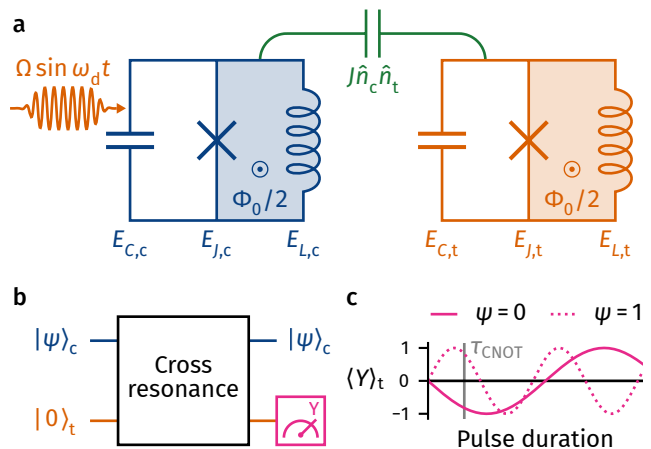


FIG. 1: Overview of the cross-resonance effect between two capacitively-coupled fluxoniums. (a) Circuit diagram showing the control qubit (left, **blue**) driven by a pulse modulated at the frequency of the target qubit (right, **orange**) with peak amplitude  $\Omega$ . Both qubits are half-flux ( $\Phi_0/2$ ) biased and have individual charging energies  $E_{C,q}$ , Josephson energies  $E_{J,q}$  and inductive energies  $E_{L,q}$ , and are coupled via their charge operators  $\hat{n}_q$  with coupling coefficient  $J$ . (b) A CNOT gate is calibrated by first preparing the control qubit in  $|\psi\rangle_c = |0\rangle_c$  or  $|1\rangle_c$  and the target qubit in  $|0\rangle_t$ , and then applying the cross-resonance pulse at a fixed amplitude for varying durations, followed by a measurement of the target qubit along the  $Y$  axis. (c) The control qubit ideally remains in its initial eigenstate while the target qubit rotates about the  $X$  axis (in the  $ZY$  plane) at an angular rate conditional on the control-qubit eigenstate,  $|\psi\rangle_c$ . When the pulse duration is  $\tau_{\text{CNOT}}$ , a net phase difference of  $\pi$  accumulates between the two conditional rotations, realizing the CNOT gate up to single-qubit phases and an additional target-qubit rotation.

The energies  $E_q^j$  and matrix elements  $\langle i | \hat{n}_q | j \rangle$  follow from the fluxonium Hamiltonian [22, 74]

$$\hat{H}_q^{\text{idle}} := 4E_{C,q} \hat{n}_q^2 + \frac{1}{2} E_{L,q} \hat{\varphi}_q^2 - E_{J,q} \cos(\hat{\varphi}_q - \varphi_{\text{ext},q}), \quad (4)$$

where  $\hat{\varphi}_q$  is the phase operator conjugate to  $\hat{n}_q$ . The fluxonium qubit has three design parameters: its charging energy  $E_{C,q}$ , inductive energy  $E_{L,q}$  and Josephson energy  $E_{J,q}$ . Its high-coherence sweet spot is achieved when the flux loop is threaded by half a flux quantum, i.e.,  $\varphi_{\text{ext},q} = \pi$ . Hence, the full design space of the two-qubit circuit is seven-dimensional, comprising  $(\{E_{J,q}, E_{C,q}, E_{L,q}\}, J)$ , see Fig. 1a. The coupling strength  $J$  is indirectly determined by requiring residual  $ZZ$  interactions to be equal to, or below, a designed threshold. The drive amplitude  $\Omega$  should ideally be calibrated to minimize the CNOT gate duration so it is not considered an independent design parameter.

### A. Effective Hamiltonian

Let  $|\tilde{i}\tilde{j}\rangle$  for  $i, j \in \mathbb{N}_0$  be the dressed eigenstates of the *undriven* (but coupled) Hamiltonian  $\hat{H}(\Omega = 0)$  with eigenenergies  $\tilde{E}^{ij}$ . Here, the state  $|\tilde{i}\tilde{j}\rangle$  is defined to be the dressed eigenstate closest to the state  $|ij\rangle$ , found by maximizing the sum of squared overlaps  $\sum_{ij} |\langle ij|\tilde{i}\tilde{j}\rangle|^2$ . The two-qubit computational subspace is spanned by  $|\tilde{0}\tilde{0}\rangle$ ,  $|\tilde{0}\tilde{1}\rangle$ ,  $|\tilde{1}\tilde{0}\rangle$  and  $|\tilde{1}\tilde{1}\rangle$ , and we define the dressed two-qubit Pauli operators as

$$\widehat{AB} := \sum_{ijkl} |\tilde{i}\tilde{j}\rangle \langle ij| \hat{A}_q \hat{B}_q |k\ell\rangle \langle \tilde{k}\tilde{\ell}| \quad (5)$$

for  $A, B \in \{X, Y, Z, I\}$ , where  $\hat{X}_q, \hat{Y}_q, \hat{Z}_q$  and  $\hat{I}_q$  are the Pauli and identity operators acting on qubit  $q$ .

It is conventional to track the qubits in the rotating frame transformed by the change-of-basis unitary

$$\hat{R}(t) := \exp \left[ -it \left( \frac{\bar{\omega}_c}{2} \widehat{ZI} + \frac{\bar{\omega}_t}{2} \widehat{IZ} \right) \right], \quad (6)$$

where

$$\bar{\omega}_c := \frac{1}{2} (\tilde{E}^{10} - \tilde{E}^{00} + \tilde{E}^{11} - \tilde{E}^{01}), \quad (7a)$$

$$\bar{\omega}_t := \frac{1}{2} (\tilde{E}^{01} - \tilde{E}^{00} + \tilde{E}^{11} - \tilde{E}^{10}) \quad (7b)$$

are the averaged qubit frequencies. In the rotating frame, the idle Hamiltonian (in the computational subspace) transforms into

$$\hat{H}_{\text{CR}}(\Omega = 0) := \hat{R}(t) [\hat{H}(\Omega = 0) - i\partial_t] \hat{R}^\dagger(t) \quad (8)$$

$$= \frac{1}{4} \mu_{ZZ}(\Omega = 0) \widehat{ZZ} + \text{const.} \quad (9)$$

where

$$\mu_{ZZ}(\Omega = 0) := (\tilde{E}^{11} - \tilde{E}^{10}) - (\tilde{E}^{01} - \tilde{E}^{00}) \quad (10)$$

is the so-called residual  $ZZ$  rate. This is an undesired always-on interaction that entangles connected qubits when idling or performing other gates. It is an unavoidable nuisance in a CR architecture with only direct capacitive couplings [23, 32, 75–77].

For a nonzero but slowly varying  $\Omega$ , and  $\omega_d = \bar{\omega}_t$ , the rotating frame Hamiltonian can be effectively written as (see Appendix B for the derivation)

$$\begin{aligned} \hat{H}_{\text{CR}}(\Omega) = & \frac{1}{2} \mu_{ZX}(\Omega) \widehat{ZX} + \frac{1}{2} \mu_{IX}(\Omega) \widehat{IX} \\ & + \frac{1}{2} \mu_{ZI}(\Omega) \widehat{ZI} + \frac{1}{2} \mu_{IZ}(\Omega) \widehat{IZ} \\ & + \frac{1}{4} \mu_{ZZ}(\Omega) \widehat{ZZ}. \end{aligned} \quad (11)$$

The coefficients  $\mu_{AB}$  can be calculated perturbatively in  $J$  in terms of matrix elements in the Floquet mode basis

of the driven control qubit,  $\{|\Phi_j(\Omega, t)\rangle\}_{j \in \mathbb{N}_0}$ . These modes satisfy the eigenvalue equation [78, 79]

$$\left( \hat{H}_c(\Omega, t) - i\partial_t \right) |\Phi_j(\Omega, t)\rangle = \epsilon_j(\Omega) |\Phi_j(\Omega, t)\rangle, \quad (12)$$

with boundary condition  $|\Phi_j(\Omega, 0)\rangle = |\Phi_j(\Omega, \frac{2\pi}{\omega_d})\rangle$ . The eigenvalues  $\{\epsilon_j(\Omega)\}_{j \in \mathbb{N}_0}$  are called the Floquet quasienergies. We assign the indices such that  $|\Phi_j(\Omega, t)\rangle$  connects to the single-qubit eigenstate  $|j\rangle$  as  $\Omega \rightarrow 0$ . Because Floquet modes are time-dependent and coperiodic with the drive, the transition moments between Floquet modes have Fourier series expansions:

$$\langle \Phi_j(\Omega, t) | \hat{O}_c | \Phi_i(\Omega, t) \rangle =: \sum_{k \in \mathbb{Z}} O_c^{[k]ji}(\Omega) e^{ik\omega_d t}, \quad (13)$$

where  $\hat{O}_c$  is either the charge  $\hat{n}_c$  or phase operator  $\hat{\varphi}_c$ .

A CNOT gate is realized with the  $ZX$  term of Eq. (11), which rotates the target qubit at an angular rate of  $|\mu_{ZX}|$  and with an orientation that depends on the control qubit state. By timing the CR pulse, one can accumulate a rotation difference of exactly  $\pi$ , which is locally equivalent to the CNOT gate (see Figs. 1b and 1c). Assuming  $J$  can be treated perturbatively, the  $ZX$  strength is

$$\mu_{ZX}(\Omega) = -J \Delta p(\Omega) n_c^{10} n_t^{10} + O(J^3), \quad (14)$$

where  $n_q^{ji} := \langle j | \hat{n}_q | i \rangle$  are the charge matrix elements in the *bare* eigenbasis and

$$\Delta p(\Omega) := \frac{n_c^{[-1]11}(\Omega) - n_c^{[-1]00}(\Omega)}{n_c^{10}} \quad (15)$$

is the *conditional polarization*, normalized by the charge dipole moment. The numerator involves the Fourier coefficients of Eq. (13) and represents the difference between the drive-induced mean charge polarizations of the 1 and 0 states, oscillating at the  $-\omega_d$  harmonic. Equation (14) tells us that the conditional polarization  $\Delta p$  is directly proportional to the effective  $ZX$  strength. From this perspective, the mechanism of the CR effect is intuitive. Driving the control qubit off-resonantly forces charge oscillations with an *initial-state dependent* amplitude; and since the control and target qubits are coupled via their charge operators, the target is resonantly driven by the oscillating control-qubit polarization.

We note that the unwanted  $\mu_{ZZ}$  coefficient scales as  $J^2$  whereas  $\mu_{ZX}$  is first order in  $J$ . Hence, the CR architecture is practicable because  $\mu_{ZZ}$  can be made small while  $\mu_{ZX}$  remains sufficient to perform a CNOT gate within a reasonable time. The other coefficients of Eq. (11) do not significantly hinder gate fidelity either. The unconditional drive  $\mu_{IX}$  can take arbitrary values if we add an additional in-phase drive directly on the target qubit [57, 80, 81]. The dynamic target-qubit detuning  $\mu_{IZ}$  can be mitigated with either a constant drive detuning, resonant target driving [81], or an echo sequence [57]. The control-qubit detuning  $\mu_{ZI}$  commutes with the other interactions and can therefore be corrected with a virtual- $Z$  before or after the CNOT gate [82].

## B. Drive-induced decoherence

Maximizing the  $ZX$  interaction during the CR gate requires strongly driving the control qubit, which can significantly alter its coherence properties from its undriven behavior [60, 83–85]. Let  $\rho$  be the density matrix of the two-fluxonium system. When weakly coupled to an environment, the density matrix evolves according to the generic master equation [84]

$$\frac{d\rho}{dt} = \sum_n \Gamma_n \mathbb{D}[\hat{L}_n]\rho \quad (16)$$

where  $\mathbb{D}[\hat{L}]\rho = \hat{L}\rho\hat{L}^\dagger - (\hat{L}^\dagger\hat{L}\rho + \rho\hat{L}^\dagger\hat{L})/2$  is the Lindblad superoperator and  $\hat{L}_n$  are the jump operators through which the system couples with the environment, with corresponding rates  $\Gamma_n$ .

In the uncoupled case,  $J = 0$ , we consider decay, excitation and dephasing of the target qubit, described by the jump operators

$$\hat{L}_t^{1\rightarrow 0} = |0\rangle\langle 1|, \quad (17)$$

$$\hat{L}_t^{0\rightarrow 1} = |1\rangle\langle 0|, \quad (18)$$

$$\hat{L}_t^\phi = \frac{|0\rangle\langle 0| - |1\rangle\langle 1|}{2}, \quad (19)$$

with associated rates  $\Gamma_t^{1\rightarrow 0}$ ,  $\Gamma_t^{0\rightarrow 1}$  and  $\Gamma_t^\phi$  respectively. Heating into higher excited states is negligible at millikelvin temperatures. For the control qubit, its jump operators are expressed in terms of the Floquet modes (evaluated at  $t = 0$ ) as

$$\hat{L}_c^{i\rightarrow j}(\Omega) = |\Phi_j(\Omega)\rangle\langle\Phi_i(\Omega)|, \quad (20)$$

$$\hat{L}_c^\phi(\Omega) = \frac{|\Phi_0(\Omega)\rangle\langle\Phi_0(\Omega)| - |\Phi_1(\Omega)\rangle\langle\Phi_1(\Omega)|}{2}, \quad (21)$$

with associated rates  $\Gamma_c^{i\rightarrow j}(\Omega)$  and  $\Gamma_c^\phi(\Omega)$ , respectively. Because the control qubit is strongly driven, heating into higher excited states cannot be ignored even in a zero-temperature environment.

A CNOT gate implemented using a square pulse with amplitude  $\Omega$  has the duration  $t_g(\Omega) = \frac{1}{2}\pi/|\mu_{ZX}(\Omega)|$ ; therefore, its average incoherent gate infidelity  $\varepsilon^{\text{incoh}}(\Omega)$  can be approximated by [86]

$$\varepsilon^{\text{incoh}} = \varepsilon_c^{\text{incoh}} + \varepsilon_t^{\text{incoh}}, \quad (22)$$

$$\varepsilon_c^{\text{incoh}} = \frac{2}{5}(\Gamma_c^1 + \Gamma_c^\phi)t_g + \frac{1}{2}\Gamma_c^\ell t_g, \quad (23)$$

$$\varepsilon_t^{\text{incoh}} = \frac{2}{5}(\Gamma_t^1 + \Gamma_t^\phi)t_g, \quad (24)$$

where  $\Gamma_q^1 := \Gamma_q^{0\rightarrow 1} + \Gamma_q^{1\rightarrow 0}$  is qubit  $q$ 's relaxation rate and  $\Gamma_c^\ell := \sum_{j=2}^{\infty} (\Gamma_c^{0\rightarrow j} + \Gamma_c^{1\rightarrow j})$  is the control qubit's leakage rate. In a very simple model where the control qubit is susceptible only to dielectric loss into a zero-temperature bath, its dissipation rates are given by ( $\Omega$ -dependence

omitted) [83, 84]

$$\Gamma_c^{i\rightarrow j} = \sum_{k\in\mathbb{Z}} |n_c^{[k]ji}|^2 S(k\omega_d + \epsilon_j - \epsilon_i), \quad (25)$$

$$\Gamma_c^\phi = \sum_{k\in\mathbb{Z}} \frac{1}{2} |n_c^{[k]11} - n_c^{[k]00}|^2 S(k\omega_d), \quad (26)$$

where

$$S(\omega) = \begin{cases} 16E_{C,c} \tan \delta & \text{for } \omega > 0, \\ 0 & \text{for } \omega \leq 0 \end{cases} \quad (27)$$

is the noise spectral density representing the lossy capacitor with loss tangent  $\tan \delta$  at *zero temperature*. We use this idealized noise model to regularize the problem of finding an optimal drive amplitude since  $|\mu_{ZX}(\Omega)|$  can become very large when the Floquet qubit modes hybridize with the plasmon modes. These modes are highly susceptible to dielectric losses and, hence, should be avoided in a real implementation. Minimizing  $\varepsilon_c^{\text{incoh}}(\Omega)$  rather than maximizing  $|\mu_{ZX}(\Omega)|$  is thus the better suited objective. Nevertheless, both goals are equivalent for small drive amplitudes. We emphasize that the errors estimated with this simple model should *not* be interpreted as a realistic incoherent error budget.

## III. PARAMETERS FOR FAST GATES

The objective of this section is to find design parameters that maximize the  $ZX$  interaction given a fixed  $ZZ$  budget. In Subsection III A, we study the maximum conditional polarization  $\Delta p$  for the control qubit only. In Subsection III B, we explore the minimum CNOT gate time landscape as a function of the control and target fluxonium parameters, at a fixed  $ZZ$  budget. Finally, in Subsection III C, we present time-domain simulations that numerically verify the predicted CNOT speed.

We primarily consider only a fixed  $E_{L,q}/E_{J,q}$  ratio of 0.25 to reduce the dimensionality of the optimization problem. There is an *approximate* one-dimensional symmetry in fluxonium parameters where the eigenstates for other  $E_{L,q}/E_{J,q}$  ratios between 0.1 and 0.5 are approximately related by a rescaling of coordinates, see Appendix C. In essence, we expect the  $ZX$  and  $ZZ$  rates for two different parameter sets to be roughly equal provided the control and target qubits across the two configurations have similar frequency and anharmonicity.

### A. Control-qubit conditional polarizability

We first focus on a typical fluxonium with parameters:  $E_{J,c}/2\pi = 4$  GHz,  $E_{C,c}/2\pi = 1$  GHz and  $E_{L,c}/2\pi = 1$  GHz, which yield a qubit frequency of  $\omega_c^{10}/2\pi \approx 582$  MHz. As shown in Fig. 2a, we calculate the conditional polarization  $\Delta p$  at a fixed drive frequency  $\omega_d$ . Here, the drive amplitude  $\Omega$  is normalized by  $\omega_c^{10}/|n_c^{10}|$

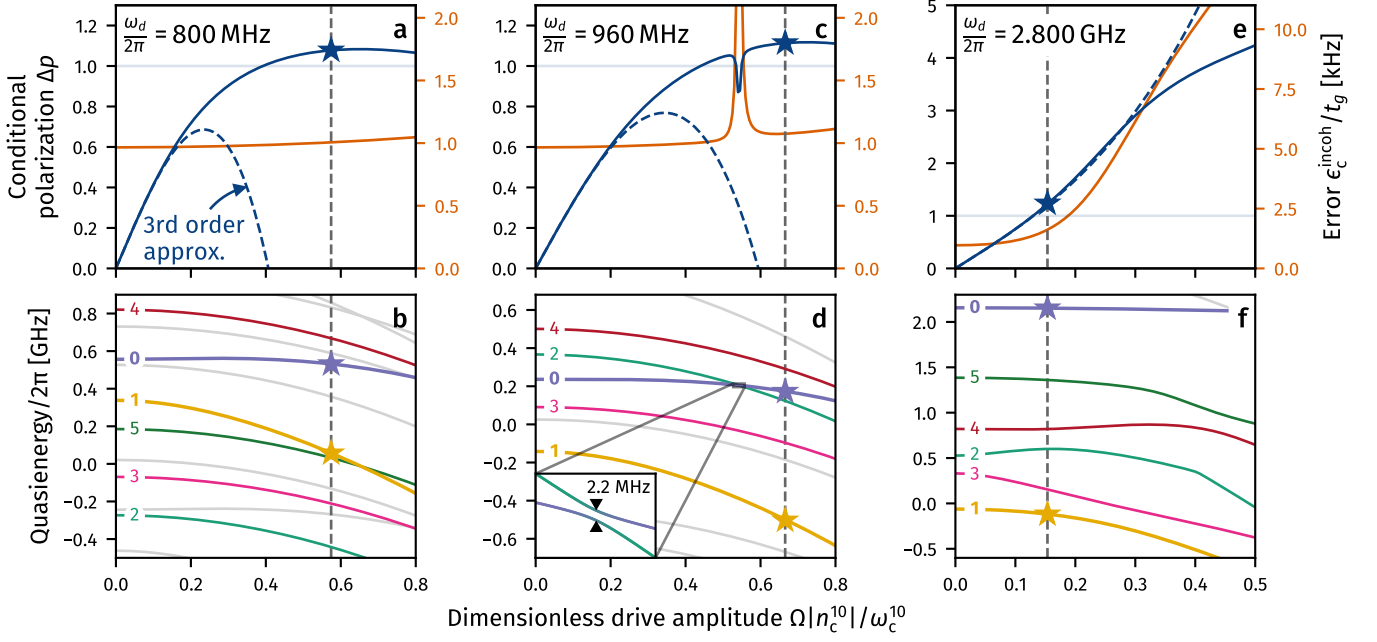


FIG. 2: (a, c, e) Conditional polarization  $\Delta p$  (**blue**) and incoherent error rate  $\varepsilon_c^{\text{incoh}}/t_g$  (**orange**) as a function of the dimensionless drive amplitude  $\Omega|n_c^{10}|/\omega_c^{10}$  for representative drive frequencies (top left label). The numerically obtained  $\Delta p$  (**solid blue**) is compared with the third-order perturbative result (**dashed blue**). (b, d, f) Floquet quasienergy spectrum of the off-resonantly-driven control fluxonium, also as a function of  $\Omega|n_c^{10}|/\omega_c^{10}$  with the same drive frequency as the top panel. Levels are labeled adiabatically, ignoring “small” avoided crossings, see main text. The **inset** of (d) shows the avoided crossing between the 0 and 2 modes, where the color of each level is based on its cycle-averaged energy. The optimal amplitude (**star ★**) minimizes  $\varepsilon_c^{\text{incoh}} \propto \varepsilon_c^{\text{incoh}}/(t_g \Delta p)$ . The control fluxonium has parameters  $E_{J,c}/2\pi = 4$  GHz,  $E_{C,c}/2\pi = 1$  GHz and  $E_{L,c}/2\pi = 1$  GHz.

to make a clear comparison to typical amplitudes used in single-qubit gates. For example,  $\Omega|n_c^{10}|/\omega_c^{10} = 0.5$  generates a  $\pi$  rotation in one Larmor period for a resonant capacitive drive. Therefore, typically  $\Omega|n_c^{10}|/\omega_c^{10} \sim 0.1$  when performing single-qubit gates [28, 29, 87]. Given a drive frequency  $\omega_d$ , we determine the optimal drive amplitude  $\Omega^*$  (marked by the star in Fig. 2a) such that the incoherent CNOT error contribution  $\varepsilon_c^{\text{incoh}}(\Omega^*)$  is minimized. Moving on, we define  $\Delta p^* := \Delta p(\Omega^*)$ . Note the dimensionless optimal amplitude  $\Omega^*|n_c^{10}|/\omega_c^{10}$  and conditional polarization  $\Delta p^*$  are constant under uniform rescaling of  $E_{C,c}$ ,  $E_{L,c}$ ,  $E_{J,c}$  and  $\omega_d$ .

Figure 2a exemplifies the simplest case, for a drive frequency of  $\omega_d/2\pi = 800$  MHz, where  $\Delta p$  increases with  $\Omega$  at first, but eventually reaches a local maximum. In other words, increasing  $\Omega$  beyond this point will *increase* the duration necessary to generate the CNOT gate. This saturation characteristic is also present in transmons and C-shunted flux qubits [88–91]. The dashed line in Fig. 2a shows the value of  $\Delta p$  calculated from perturbatively obtained Floquet modes, up to  $O(\Omega^3)$ . Although initially agreeing with the numerical result, the perturbative model fails to accurately predict both the maximum  $\Delta p$  or the value of  $\Omega$  at which it occurs. The solid orange line in Fig. 2a is the incoherent error contribution

from the control qubit due to dielectric loss into a zero-temperature bath, as defined in Section II B, assuming a dielectric loss tangent of  $\tan \delta = 10^{-6}$  [30, 36, 95]. It is divided by the total gate duration and expressed as a rate in kHz since  $t_g$  depends not only on  $\Delta p$  but also linearly on  $J$  and  $n_t^{10}$ . To be more precise, the optimal amplitude is found by

$$\Omega^* := \arg \min_{\Omega} \frac{\varepsilon_c^{\text{incoh}}(\Omega)}{t_g(\Omega)\Delta p(\Omega)}, \quad (28)$$

although this is equivalent to minimizing  $\varepsilon_c^{\text{incoh}}(\Omega)$  since  $t_g(\Omega) \propto 1/\Delta p(\Omega)$ .

As previously mentioned, we evaluate the incoherent errors in the basis of the Floquet modes, thus, it is insightful to also consider the quasienergy spectrum, see Fig. 2b. We label the quasienergy levels, similar to Ref. [98], whereby  $\Omega$  is increased in small steps and the newly calculated Floquet modes are labeled according to their maximum cycle-averaged overlap with the previous modes. This labeling is not exactly adiabatic, as apparent from the crossing between modes 1 and 5. Here, the gap size is numerically computed to be very small (less than one hertz). Thus, for all intents and purposes, this is a level crossing rather than an anti-crossing. In general, our state identification algorithm

ignores quasienergy gaps less than  $2\pi \times 10$  MHz by lifting the near degeneracy using the cycle-averaged energy quantum number [99, 100]. For a realistic ramp rate, the qubit will traverse diabatically with high probability so these collisions do not contribute meaningfully to the coherent error budget. Exact level crossings occur between the colored levels and their gray replicas in another Brillouin zone since they belong to distinct two-fold symmetry groups, as explained in Appendix D.

While Figs. 2a and 2b show the typical situation where there is a clear optimal  $\Delta p^*$ , the behavior in other instances can be more complicated. See, for example, Figs. 2c and 2d, where  $\omega_d/2\pi = 960$  MHz. Here, the small avoided crossing between modes 0 and 2, with a gap of  $2\pi \times 2.2$  MHz, causes a small drop in  $\Delta p$  while significantly increasing the incoherent errors due to hybridization with the leakage modes. Additionally, in Figs. 2e and 2f, where  $\omega_d/2\pi = 2.8$  GHz, there is a large avoided crossing between modes 1 and 3 around  $\Omega|n_c^{10}|/\omega_c^{10} \approx 0.2$ . The optimal drive strength  $\Omega^*$  occurs at a relatively modest value before  $\Delta p$  has plateaued due to the large monotonic increase in the incoherent error at stronger drive. This last case is an explicit example where the optimal drive amplitude does *not* maximize  $\Delta p$ .

More generally, we notice that the optimal conditional polarization decreases significantly when  $\omega_d$  is below  $\omega_c^{10}$ , see Fig. 3a, which in turn leads to slow gates and therefore large incoherent errors, see Fig. 3b. This establishes a clear preferred direction for the CR gate: the control qubit should be the lower frequency qubit of the pair. When  $\omega_d$  is just above  $\omega_c^{10}$ , we have  $|\Delta p^*| \approx 1$ . The conditional polarization remains above unity until  $\omega_d$  approaches half of the control fluxonium's  $0 \rightarrow 2$  frequency, due to the hybridization caused by two-photon resonances. At even higher frequencies, around  $\omega_d/2\pi \approx 2.6$  GHz,  $|\Delta p^*|$  peaks at roughly 1.4. The incoherent error is larger for higher drive frequencies, but it remains low when we drive away from any resonances. The target qubit can therefore be highly detuned without compromising gate speed. This frequency flexibility stands in contrast to transmons, for which the target qubit should be detuned by no more than the control qubit's anharmonicity to facilitate fast gates [88–90].

Since fluxonium qubits typically have frequencies below 1 GHz to mitigate dielectric loss [36, 95], it is auspicious to design the nominal target-qubit frequencies to sit between  $f_{10}$  and  $f_{20}/4$  in Fig. 3. This frequency interval can be broadened by raising the control qubit's anharmonicity, for example, by increasing  $E_{J,c}/E_{C,c}$ . With this insight in mind, we see in Fig. 4a that a larger  $E_{J,c}/E_{C,c}$  ratio leads to a wider frequency interval where  $|\Delta p^*| > 1$ . This arises from two complementary causes. First, the qubit frequency is lower for a larger Josephson energy. Second, the energy levels of the higher excited states increase as a function of the Josephson energy, widening the wedge between  $f_{10}$  and  $f_{20}/4$ . Consequently, a large  $E_{J,c}/E_{C,c}$  ratio reduces the probability of frequency collisions in the sub-gigahertz band.

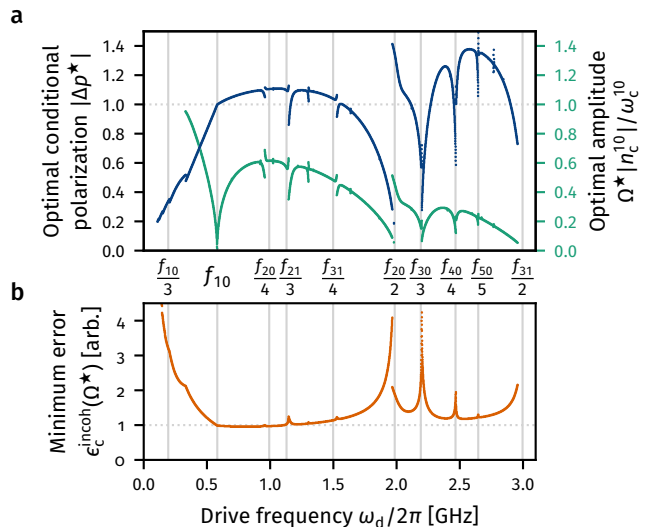


FIG. 3: (a) Optimal conditional polarization magnitude  $|\Delta p^*|$  (**blue**) and corresponding optimal drive amplitude  $\Omega^*$  (**green**), as a function of the drive frequency  $\omega_d$ . The absolute value of  $\Delta p^*$  is plotted since its sign flips at  $\omega_d = \omega_c^{10}$ . The amplitude is optimized to minimize the error contribution  $\epsilon_c^{\text{incoh}}(\Omega^*)$ , shown in (b). Resonances with bare transition frequencies (**vertical lines**) are annotated with  $f_{ij} := (E_c^i - E_c^j)/2\pi$ . The control fluxonium has the same parameters as in Fig. 2.

We further notice that changing  $E_{L,c}/E_{J,c}$  does not qualitatively affect our observations, see Fig. 4b for  $E_{L,c}/E_{J,c} = 0.10$  and a renormalized  $E_{C,c}/2\pi = 1.3$  GHz. The  $E_{J,c}/E_{C,c}$  range is rescaled to span from 1 to 4 so that the control-qubit frequencies stay comparable to those in Fig. 4a. When the drive frequency is below  $f_{20}/2$ , the heatmap in both Figs. 4a and 4b looks very similar. The resonances above  $f_{20}/2$  differ noticeably because smaller Josephson and inductive energies compress the higher energy levels, producing a more crowded spectrum. Although the high frequency behavior of  $|\Delta p^*|$  is less relevant for the CR effect between sub-gigahertz fluxoniums, this detail is relevant for CR gates between a control fluxonium and a target transmon [45, 48], or a microwave oscillator [101].

Conveniently, within the frequency range of interest, the approximation  $|\Delta p^*| \approx 1$  holds reasonably well. Combining this with Eq. (14), we arrive at a simple formula for the minimum CNOT gate time between any two capacitively-coupled fluxoniums in terms of the coupling strength and their charge dipole moments:

$$\tau_{\text{CNOT}}^* = \frac{\pi/2}{J|n_c^{10}n_t^{10}|}. \quad (29)$$

This speed limit is easy to evaluate, valid beyond simple perturbative approximations and, thus, different to the limit given in Ref. [80]. In particular, Ref. [80] assumes  $\Omega/(\omega_t^{10} - \omega_c^{10})$  is small and that gate speed is primarily

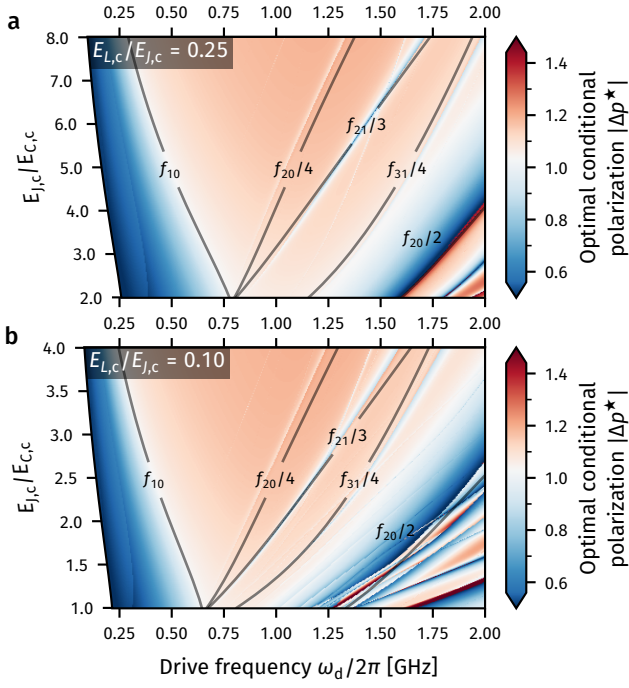


FIG. 4: Optimal conditional polarization  $|\Delta p^*|$  as a function of the drive frequency  $\omega_d$  and the control fluxonium Josephson-to-charging energy ratio  $E_{J,c}/E_{C,c}$ , while fixing  $E_{L,c}/E_{J,c} = (0.25, 0.10)$  and  $E_{C,c}/2\pi = (1.0, 1.3)$  GHz in panels (a, b), respectively. The lower frequency cutoff is equal to one third of the control-qubit frequency. Resonances with bare transition (**black curves**) are annotated with  $f_{ij} := (E_c^i - E_c^j)/2\pi$ .

limited by off-resonant driving of the control qubit.

## B. CNOT duration landscape

Increasing the coupling strength  $J$  decreases the duration of the CNOT gate, as per the speed-limit formula in Eq. (29). In practice, however, we also need to keep the residual  $ZZ$  rate below a certain threshold, which indirectly determines the value of  $J$ . By fixing  $E_{L,q}/E_{J,q} = 0.25$  for both control and target fluxoniums, and their qubit frequencies to  $\omega_c^{10}/2\pi = 500$  MHz and  $\omega_t^{10}/2\pi = 800$  MHz, we reduce the number of free system parameters to just two. Thus, we can directly extract the expected CNOT time  $\tau_{\text{CNOT}}^*$  as a function of the control and target  $E_{J,q}/E_{C,q}$  ratios. We confirm in Appendix E that the CNOT time is largely independent of the precise control and target qubit frequencies we have chosen.

With our fixed parameters, and  $|\mu_{ZZ}|/2\pi = 50$  kHz, Fig. 5a shows  $\tau_{\text{CNOT}}^*$  lies in the range of 130 ns to 230 ns. In particular, for  $E_{J,q}/E_{C,q} \lesssim 4$ , we see  $\tau_{\text{CNOT}}^*$  is lower than 150 ns. In general, smaller  $E_{J,q}/E_{C,q}$  ratios lead to faster CNOT gates; but a small control-qubit  $E_{J,c}/E_{C,c}$  decreases its anharmonicity, thereby in-

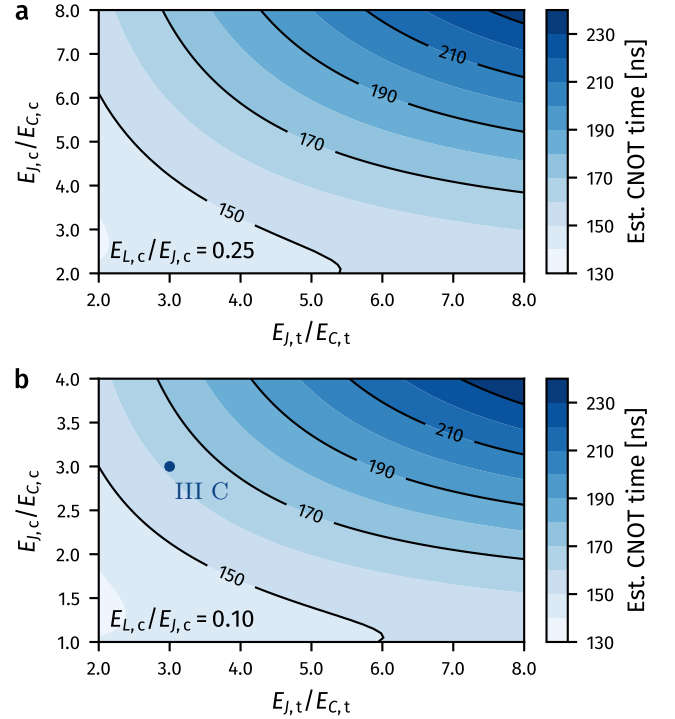


FIG. 5: Estimated CNOT time for two capacitively-coupled fluxonium qubits with frequencies  $\omega_{(c,t)}^{10}/2\pi = (500, 800)$  MHz and a coupling strength  $J$  determined by  $|\mu_{ZZ}|/2\pi = 50$  kHz, for varying Josephson-to-charging energy ratios  $E_{J,q}/E_{C,q}$ . The inductive-to-Josephson energy ratio of the target fluxonium is  $E_{L,t}/E_{J,t} = 0.25$  in both panels and that of the control is (a)  $E_{L,c}/E_{J,c} = 0.25$  and (b) 0.10. The round **marker** in (b) corresponds to the system parameters used in Section III C.

creasing the likelihood that the CR drive accidentally excites leakage transitions. A relatively fast CNOT under 170 ns is still achievable with  $E_{J,c}/E_{C,c} = 8$ , provided that  $E_{J,t}/E_{C,t} < 3$ . In Fig. 5b, we again notice that for  $E_{L,c}/E_{C,c} = 0.10$ , we find similar CNOT times compared to the  $E_{L,c}/E_{C,c} = 0.25$  case in Fig. 5a, after appropriately rescaling the control qubit  $E_{J,c}$ .

The key takeaway from this subsection and Subsection III A is as follows. To minimize frequency collisions and maximize CNOT speed, the control qubit should have a *low frequency* and a *high anharmonicity* (large  $E_{J,c}/E_{C,c}$ ), whereas the target qubit should have a *higher frequency* and a *lower anharmonicity* (smaller  $E_{J,t}/E_{C,t}$ ).

## C. Time-domain simulation

To complement the semi-analytical analysis, we now verify the gate performance with numerical time-domain simulations. For simplicity, we focus only on a single example system given by the Hamiltonian parameters in

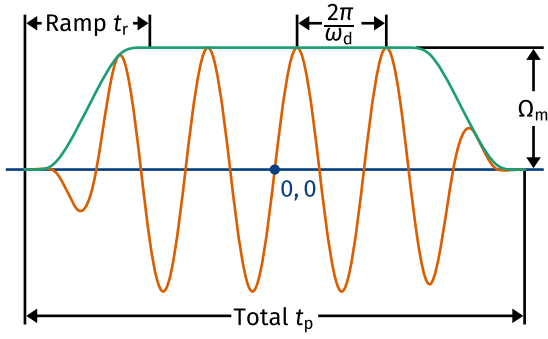


FIG. 6: Soft square CR pulse used to drive the control qubit in time-domain simulations. The non-zero pulse duration is  $t_p$  which includes two Planck-taper ramps of duration  $t_r$  each from zero to a midpoint plateau amplitude of  $\Omega_m$ . The envelope (**green**) is modulated by  $\sin(\omega_d t)$  to synthesize the microwave signal (**orange**). The equation for the envelope is given in Eq. (30).

	$E_{J,q}/2\pi$ [GHz]	$E_{C,q}/2\pi$ [GHz]	$E_{L,q}/2\pi$ [GHz]	$J/2\pi$ [MHz]
Control	5.60	1.87	0.56	
Target	3.52	1.18	0.88	97

TABLE I: Hamiltonian parameters used in the time-domain simulations of Section III C. The bare control-qubit frequency is 502 MHz and the bare target-qubit frequency is 805 MHz. The  $ZZ$  rate is  $\mu_{ZZ}/2\pi \approx -50$  kHz.

Table I. The Hilbert space is truncated down to 32 dimensions, consisting of the dressed product states with 8 control fluxonium and 4 target fluxonium levels. In this system, the bare control-qubit frequency is 502 MHz and the bare target-qubit frequency is 805 MHz. The residual  $ZZ$  rate is  $\mu_{ZZ}/2\pi \approx -50$  kHz. The inductive-to-Josephson energy ratios are  $E_{L,c}/E_{J,c} = 0.10$  and  $E_{L,t}/E_{J,t} = 0.25$  and the Josephson-to-charging energy ratios for both fluxoniums are  $E_{J,q}/E_{C,q} \approx 3$ . These system parameters correspond to the marker in Fig. 5b.

The CR drive is modulated by a soft square envelope, shown pictorially in Fig. 6, or in equation form,

$$\Omega(t) = \Omega_m \times \begin{cases} 1 & |t| \leq \frac{t_p}{2} - t_r, \\ \mathcal{R}\left(|t| - \frac{t_p}{2}\right) & \frac{t_p}{2} - t_r < |t| < \frac{t_p}{2}, \\ 0 & \text{otherwise,} \end{cases} \quad (30)$$

where

$$\mathcal{R}(t) := \left[ 1 + \exp\left(\frac{t_r}{t_r - t} - \frac{t_r}{t}\right) \right]^{-1} \quad (31)$$

is a Planck-tapered ramp function varying from 1 to 0 over  $0 < t < t_r$ . The gate is therefore active over the

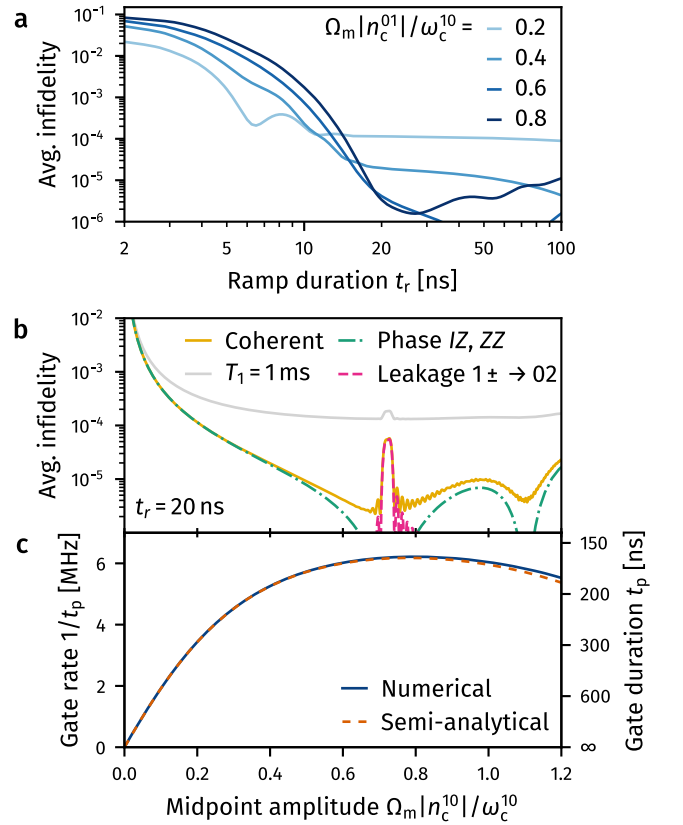


FIG. 7: (a) Optimized average CNOT infidelity as a function of both the ramp duration  $t_r$  and midpoint amplitude  $\Omega_m$ . (b) Optimized infidelity and (c) corresponding gate rate (inverse gate duration  $1/t_p$ ) as a function of  $\Omega_m$  for fixed  $t_r = 20$  ns. The coherent error (**solid yellow**) in (b) is decomposed into phase error (from  $IZ$  and  $ZZ$ , **dash-dotted green**) and leakage error (**dashed pink**). Incoherent error (**solid gray**) is added assuming  $T_1 = 1$  ms. The numerically optimized gate rate (**solid blue**) in (c) is compared to the semi-analytically derived, Eq. (14), gate rate (**dashed orange**).

interval  $[-t_p/2, +t_p/2]$ . The smooth ramps aim to ensure the 0 and 1 states of the control qubit are adiabatically transported to their corresponding Floquet modes.

After computing the full gate unitary, we truncate it down to a  $4 \times 4$  matrix acting on the computational subspace. This sub-matrix is further transformed into a rotating frame where the target-qubit frequency is reduced by the *drive frequency*  $\omega_d$  (as opposed to the average target-qubit frequency). From this, we calculate the average infidelity to the CNOT gate after applying compensating  $Z$  and  $X$  rotations on the control and target qubits, respectively; see Appendix F for details.

The simulations show significant control-qubit errors for ramps shorter than 20 ns, see Fig. 7a. Here, the total pulse duration  $t_p$  and drive frequency  $\omega_d$  are optimized at each point to minimize infidelity. For longer ramps,

we generally observe coherent errors below  $10^{-4}$  for a range of drive amplitudes. Moreover, we see that smaller amplitude gates possess larger infidelity because the ratio of the  $ZZ$  to  $ZX$  strength is larger, which tilts the target qubit's rotation axis away from the equator.

For a fixed ramp duration  $t_r = 20$  ns, Fig. 7b shows that coherent gate errors below  $10^{-4}$  are consistently achieved across a large range of drive amplitudes. Here, the total coherent error is plotted as the solid yellow line, together with an estimate of the incoherent error shown as the solid gray line. The incoherent error estimate uses the simple formula  $\frac{4}{5}t_p/T_1$  where  $T_1 = 1$  ms [102], which yields a minimum error just above  $10^{-4}$ . More specifically, the total coherent error can be decomposed into a phase error (arising from nonzero  $IZ$  and  $ZZ$  during the gate), plotted in dash-dotted green, or leakage out of the computational subspace, plotted in dashed pink. Leakage in this case is the result of the energies  $\epsilon_1(\Omega) + E_t^1 + 4\omega_d$  and  $\epsilon_0(\Omega) + E_t^2$  coming onto resonance at  $\Omega|n_c^{10}|/\omega_c^{10} \approx 0.7$ , see also the discussion in Section IV and further simulations in Appendix G 2. Residual ripples remain in the coherent error for larger amplitudes because the avoided crossing is traversed once at both the start and end ramps, producing Landau-Zener-Stückelberg interference [103]. The coherent error is generally dominated by phase error, except near  $\Omega_m|n_c^{10}|/\omega_c^{10} = 0.7$  and 1.1, where the phase error drops below  $10^{-9}$ . We hypothesize this occurs because the unconditional drive induced on the target qubit at certain amplitudes cancels the net  $IZ$  and  $ZZ$  components, akin to the rotary pulses of Ref. [81].

Having numerically calculated the CNOT duration, we can verify that the gate rate (inverse of the gate duration) matches with the prediction from Eq. (14), see Fig. 7c. The predicted gate rate for a time-varying pulse is determined by averaging the semi-analytic expression for the  $ZX$  rate in Eq. (14) over the pulse shape. Both the numerical and semi-analytical results agree very well at low amplitudes, but deviate up to 3% at the largest amplitudes considered. The fastest gate is achieved in 161 ns, in accordance with the estimates of Fig. 5b. Although  $\Delta p$  often saturates above unity, the crude approximation of Eq. (29), which takes  $\Delta p^* = 1$ , is accurate in this instance because the underestimation can be viewed as a correction factor to account for a finite ramp duration.

#### IV. FREQUENCY COLLISIONS

Driving the control qubit at the amplitude needed to saturate the  $ZX$  rate can induce undesired multiphoton transitions, as anticipated in Fig. 7b. These transitions stem from resonances between Floquet quasienergies and should be avoided. In this section, we establish general guidelines for choosing fluxonium parameters that circumvent unwanted resonances and ensure that fast CNOT gates between qubit pairs remain feasible, even in the presence of random fabrication disorder.

Using the insights from Section III, we fix the control-qubit parameters to  $E_{J,c}/2\pi = 4.0$  GHz,  $E_{C,c}/2\pi = 1.2$  GHz and  $E_{L,c}/2\pi = 0.4$  GHz. These parameters produce a low-frequency control qubit with a high anharmonicity, providing a wide range for positioning the target-qubit frequencies. Moreover, a small  $E_{L,c}/E_{J,c}$  ratio minimizes relaxation via inductive losses, see Appendix C. To analyze potential frequency collisions, we use an effective energy spectral density description of the driven control qubit's charge operator. Throughout this section, we consider a frequency collision to be an unwanted resonant interaction inducing a coherent error exceeding  $10^{-4}$ . This threshold reflects the approximate incoherent error expected from a 100 ns gate applied between qubits with a 1 ms lifetime.

##### A. Control-qubit leakage

To simulate the control-qubit transition probabilities, we use the envelope from Eq. (30). In this numerical simulation, the fluxonium is truncated to its lowest six eigenstates. Because the transition probabilities are susceptible to interference effects that depend on the pulse duration  $t_p$ , we wish to somehow average  $t_p$  away. This effective phase averaging is emulated by evolving unitarily during the ramp portions of the envelope, and applying a completely dephasing channel in the basis of Floquet modes during the plateau.

To determine what midpoint amplitude  $\Omega_m$  to use, we first solve the inverse problem of finding the amplitude required to achieve a given conditional polarization  $|\Delta p|$  for a range of drive frequencies, see Fig. 8a. Here, the solid contour lines are overlaid to show where  $|\Delta p|$  is equal to steps between 0.4 and 1.0. Notice that  $|\Delta p|$  is not well defined near certain resonances (avoided crossings in the quasienergy spectrum). These resonances are annotated with the notation  $i^k \rightarrow j$  meaning a  $k$ -photon transition from  $i$  to  $j$ . The resonances bend with drive amplitude because the energies of the dressed initial and final states are Stark shifted. Given a desired  $|\Delta p|$ , we use an arbitrary spline fit to the contour lines to map a drive frequency  $\omega_d$  to a drive amplitude  $\Omega_m$ . As already discussed in Section III A, driving below the control-qubit frequency results in slow gates. Thus, we do not consider this case any further.

Having constructed a map from  $\omega_d$  to  $\Omega_m$ , we can now calculate the probability for the control qubit to transition out of its initial state as a function of  $\omega_d$  and  $|\Delta p(\Omega_m)|$ , this is shown in Fig. 8b as an average over initial 0 and 1 states. The filled shaded blue curves correspond to fixing the ramp duration to 20 ns, with  $|\Delta p(\Omega_m)|$  indicated by its fill color. The widest peak is, as expected, the  $0 \leftrightarrow 1$  transition when the control qubit is driven near resonance. Other major leakage transitions only occur when  $\omega_d/2\pi > 1$  GHz. We also consider a slightly longer ramp of 50 ns (shown in dotted orange). We see that the width of its  $0 \leftrightarrow 1$  peak roughly halves

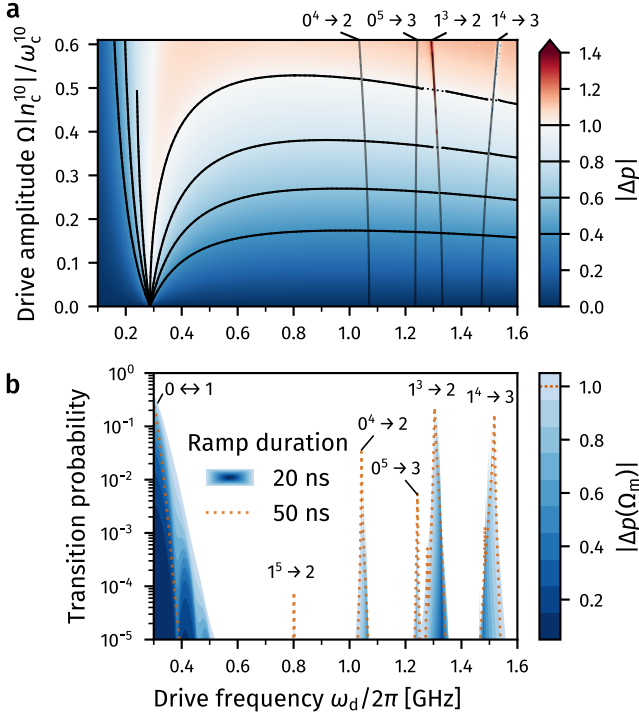


FIG. 8: (a) Control-qubit conditional polarization  $|\Delta p|$  as a function of drive frequency  $\omega_d$  and amplitude  $\Omega$ . The contour lines of  $|\Delta p|$  (solid black) for 0.8 and 1.0 do not extend to the lower drive frequencies because these values are not attained there. Avoided crossings in the Floquet quasienergy spectrum occur along the near-vertical **translucent** lines. The energy levels participating in the avoided crossing is annotated on the top spine with the superscript indicating the transition photon order. The contour lines are intentionally undefined near avoided crossings because they would otherwise introduce large discontinuities. Spline fits to the solid lines (dotted) are used to interpolate across the gaps. (b) Control-qubit transition probability averaged over initial 0 and 1 states, after applying a Planck-tapered square pulse with ramp duration 20 ns (filled blue) or 50 ns (dotted orange) with drive frequency  $\omega_d$  and midpoint amplitude  $\Omega_m$ , such that the midpoint conditional polarization  $|\Delta p(\Omega_m)|$  is constant. The **blue shading** indicates the value of  $|\Delta p(\Omega_m)|$  for the 20 ns ramp, whereas  $|\Delta p(\Omega_m)| = 1.0$  for the 50 ns ramp. The transitions associated with each peak are annotated in the same format as (a). Control-qubit parameters are  $E_J/2\pi = 4.0$  GHz,  $E_C/2\pi = 1.2$  GHz and  $E_L/2\pi = 0.4$  GHz.

compared to the 20 ns case. This is intuitive since, for a first-order transition, the peak width is expected to be inversely proportional to the ramp duration. By contrast, the peak widths of the higher-order leakage transitions show little difference between the two ramp durations.

We summarize the observed collision bounds in Table II for the longer ramp duration of 50 ns and for

$\Delta p = 0.8$  and 1.0. The longer ramp is chosen here to minimize the bounds on the  $0 \leftrightarrow 1$  collision. The bounds on the multiphoton processes are asymmetric around the bare transition frequency because the energies of the involved states are Stark shifted by the strong drive. A lower bound for the  $0 \leftrightarrow 1$  transition is not provided since we do not consider CR drives below the control-qubit frequency. For the target qubit, which is ideally sub-gigahertz, the only relevant unwanted transition is the  $0 \leftrightarrow 1$  bitflip. Thus, based on suppressing control-qubit transitions alone, Table II suggests that the target-qubit frequency can sit between 362 MHz and 1 GHz, for a drive amplitude enabling  $\Delta p = 0.8$ .

Transition	Bare frequency [MHz]	Bounds [MHz]	
		$\Delta p = 0.8$	$\Delta p = 1.0$
$0 \leftrightarrow 1$	286	+76	+86
$1^3 \rightarrow 2$	1332	-32, +5	-48, +6
$0^4 \rightarrow 2$	1070	-19, -8	-36, -9
$1^4 \rightarrow 3$	1472	+6, +37	+6, +61
$0^5 \rightarrow 3$	1235	+2, +6	+0, +12
$1^5 \rightarrow 2$	799		+1, +3

TABLE II: Frequency collision bounds on control-qubit transitions extracted from Fig. 8b with a probability threshold of  $10^{-4}$ . The bounds are expressed as a pair of lower, upper detunings relative to the bare frequency.

## B. Effective energy spectral density

In this section, we briefly introduce the *effective energy spectral density* (effective ESD) of the control fluxonium's charge operator, which will allow us to visualize the frequency bands that may drive undesired two-body transitions. The effective ESD arises naturally in the interaction picture of the individual Hamiltonians, whose time-evolution unitaries are

$$\hat{U}_c(t_1, t_0) = \mathcal{T} \exp\left(-i \int_{t_0}^{t_1} \hat{H}_c(\Omega(t), t) dt\right), \quad (32)$$

$$\hat{U}_t(t_1, t_0) = \exp(-i \hat{H}_t \times (t_1 - t_0)). \quad (33)$$

Recall,  $\hat{H}_c$  and  $\hat{H}_t$  are the individual Hamiltonians of the control and target qubits, respectively. If we assume  $\Omega(t)$  drives the CR gate from the time  $t_i$  to the time  $t_f$ , the change-of-basis unitary into the interaction picture is  $\hat{A}(t) = \hat{A}_c(t) \otimes \hat{A}_t(t)$  where  $\hat{A}_q(t) = \hat{U}_q^\dagger(t, t_i)$ . The *coupled* Hamiltonian in the interaction picture then becomes

$$\hat{H}_I(t) = J \hat{n}_{c,I}(t) \hat{n}_{t,I}(t) \quad (34)$$

where  $\hat{n}_{q,I}(t) := \hat{A}_q(t) \hat{n}_q \hat{A}_q^\dagger(t)$  are the interaction-picture charge operators.

From the interaction-picture Hamiltonian, it is clear that transitions occur due to the coupling  $\hat{n}_{c,I}(t) \hat{n}_{t,I}(t)$ .

Therefore, we can calculate the transition probability from the product state  $|ki\rangle$  to  $|lj\rangle$  within perturbation theory as

$$P^{ki\rightarrow lj} = J^2 |n_t^{ji}|^2 \left| \int_{t_i}^{t_r} n_{c,I}^{\ell k}(t) e^{i\omega_t^{ji} t} dt \right|^2, \quad (35)$$

where  $\omega_q^{ji} := E_q^j - E_q^i$ . Given that  $\Omega(t)$  is explicitly defined to be zero outside the integration domain, we “can” extend the integration limits and simply obtain

$$P^{ki\rightarrow lj} = J^2 |n_t^{ji}|^2 |\mathcal{F}\{n_{c,I}^{\ell k}\}(-\omega_t^{ji})|^2, \quad (36)$$

using the Fourier transform convention  $\mathcal{F}\{f\}(\omega) = \int_{-\infty}^{\infty} f(t) e^{-i\omega t} dt$ . We can simplify Eq. (36) further by averaging (summing) over initial (final) control states:

$$P_t^{i\rightarrow j} = J^2 |n_t^{ji}|^2 \mathcal{E}(-\omega_t^{ji}), \quad (37)$$

where

$$\mathcal{E}(\omega) = \frac{1}{2} \sum_{\ell=0}^{\infty} \sum_{k=0}^1 |\mathcal{F}\{n_{c,I}^{\ell k}\}(\omega)|^2 \quad (38)$$

is the effective energy spectral density of the control fluxonium’s charge operator.

Equation (37) is useful since we have fixed the control-fluxonium parameters, so the effective ESD needs to be computed only once, but the allocation of target-fluxonium parameters remain to be determined. The extension of the integration limits in going from Eq. (35) to Eq. (36) requires careful justification since the integrand does not always decay at long times. For a more rigorous derivation of Eq. (37) using Floquet theory, see Appendix G. To be precise, the ESD we calculate is averaged over all carrier phases as opposed to a fixed sinusoidal carrier.

### C. Control-fluxonium effective ESD

Having established the control-fluxonium ESD as a central quantity of interest, we now distill its main features. We calculate the ESD for an envelope with the Planck-taper ramp function, Eq. (31), with a ramp duration of  $t_r = 50$  ns and visualize it in Fig. 9 as a function of the drive frequency (limiting the calculations above the control-qubit frequency). The plateau duration is idealized to be infinitely long, see Appendix H. Since the charge matrix elements connecting the computational states of a fluxonium typically have less than unit magnitudes, only the visible peaks of Fig. 9 can induce transitions with probability greater than or approximately  $10^{-4}$ . The gray horizontal bands mask the drive frequencies which scatter the control qubit and represent collision windows already documented in Table II. The pair of vertical peaks near  $\omega/2\pi \approx \pm 300$  MHz are the drive-photon unassisted  $0 \leftrightarrow 1$  bitflip transitions of the

control fluxonium. Because the qubit frequency is Stark shifted downwards when driven with a positive detuning, these peaks broaden with increasing  $\Delta p$ . The slanted peaks correspond to drive-photon assisted transitions. The background gradient divides the plot window into intervals of the  $\omega/\omega_d$  ratios, as mapped by the color bar in the bottom left. The gradient steps occur on odd harmonics  $|\omega|/\omega_d \in 2\mathbb{N}_0 + 1$ . The first harmonic  $|\omega| = \omega_d$  is the desired response that resonantly drives the target qubit. However, the third harmonic  $|\omega| = 3\omega_d$ , for instance, is undesired as it may overlap with a neighboring fluxonium’s leakage transition frequency. Recall that our Fourier sign convention implies that negative frequencies of the ESD excite the target fluxonium, whereas positive frequencies de-excite. As such, we see in the top panels of Fig. 9 that multi-photon excitations increase in likelihood with increasing drive strength.

Only exact odd-harmonic peaks are allowed when the fluxonium is biased at half flux due to parity symmetry. Therefore, a peak with an even number of drive photons must also involve a control-fluxonium transition. For instance, in Fig. 9a where  $\Delta p = 0.6$ , there are four peaks between  $\omega_d < |\omega| < 3\omega_d$ . These are the  $\pm 2\omega_d$  bitflip sideband transitions where the control fluxonium undergoes either  $0 \rightarrow 1$  or  $1 \rightarrow 0$ . Additionally, in the top right corner of Fig. 9a, we annotate the  $-2\omega_d + \tilde{\omega}_c^{21}$  leakage sideband. (The tilde signifies the Stark-shifted transition frequency.) As the drive amplitude increases to induce  $\Delta p = 0.8$  in Fig. 9b, another leakage sideband is discernible:  $-3\omega_d + \tilde{\omega}_c^{20}$ . In Fig. 9c where  $\Delta p = 1.0$ , the  $-4\omega_d + \tilde{\omega}_c^{30}$  sideband is visible. As expected, a stronger drive enhances the higher-harmonic responses.

When the control fluxonium has a large anharmonicity, like in this case, the (annotated) leakage sidebands are only relevant when the drive frequency is over one gigahertz. Therefore, the main source of potential frequency collisions are the third harmonics and second-harmonic bitflip sidebands. The third harmonic can be avoided if the target fluxonium’s  $1 \rightarrow 2$  transition is beyond three times the maximum target-qubit frequency (e.g., beyond 3 GHz). Unfortunately, the bitflip sideband for a low frequency drive easily collides with a higher qubit-frequency spectator. Because the sideband frequency is Stark shifted as the drive amplitude is ramped up or down, its collision with a spectator transition can be interpreted as Landau–Zener–Stückelberg interference [103]. Hence, optimal control may nullify this collision by engineering destructive interference. However, investigating this or other pulse optimization techniques lies beyond the scope of this work.

### D. Control–target resonances

Although we can use the ESD along with Eq. (37) to accurately predict leakage probabilities, we choose, for simplicity, to only use the ESD as a guide for deciding which leakage transitions are important. The size

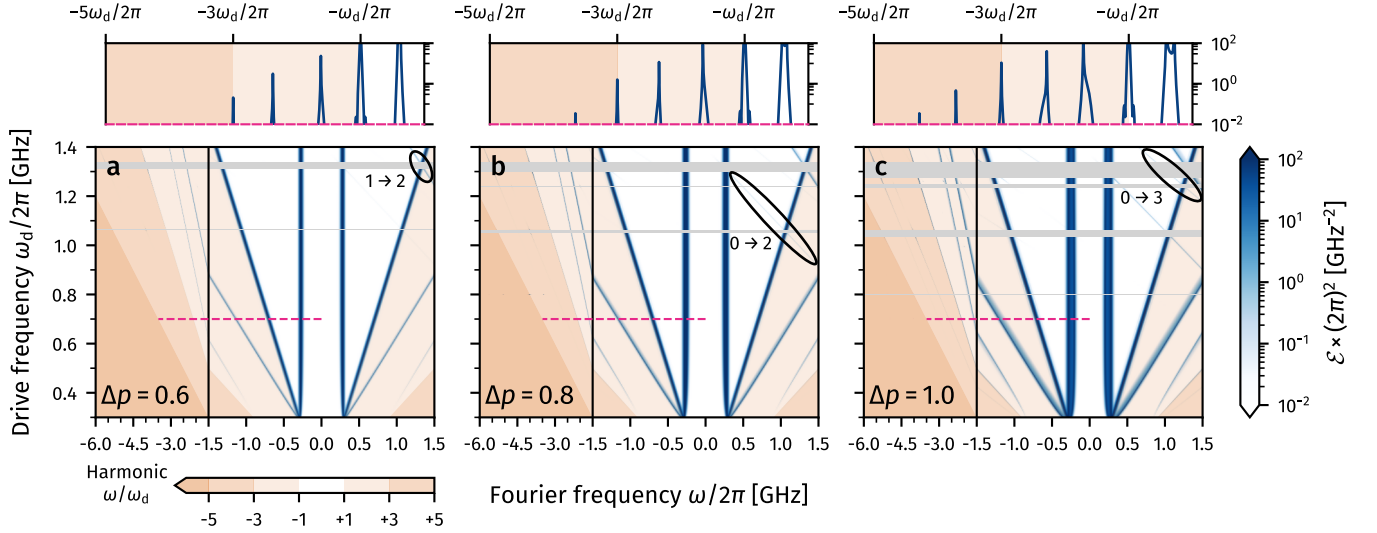


FIG. 9: Effective energy spectral density of the control fluxonium’s charge operator  $\mathcal{E}_c^{nn}$  for conditional polarizations (a)  $\Delta p = 0.6$ , (b)  $\Delta p = 0.8$ , (c)  $\Delta p = 1.0$ . Line cuts at  $\omega_d = 700$  MHz are shown along the top row. The horizontal axis is compressed between  $-6.0$  GHz to  $-1.5$  GHz to conserve space. The gray horizontal bands mask drive frequencies which scatter the control qubit and invalidates the ESD, see Table II. The background gradient partitions the viewport into a range of  $\omega/\omega_d$  ratios, as indicated by the color bar in the bottom left. The gradient steps occur on odd harmonics  $|\omega|/\omega_d \in 2\mathbb{N}_0 + 1$ . Leakage sideband peaks are circled and annotated with the control-fluxonium transition induced. Control-fluxonium parameters are the same as in Fig. 8.

of the collision windows we present here are based on transition probabilities obtained by numerically solving the Schrödinger equation as in Section IV A. We use the envelope from Eq. (30) with a ramp duration of 50 ns and plateau amplitude inducing  $\Delta p = 0.8$ , unless otherwise stated. Again, we ignore interference effects by completely dephasing the system in the basis of Floquet modes, see Section IV A.

We start by simulating the collision probabilities between our control fluxonium, whose parameters we have fixed, and a target fluxonium whose parameters will be randomly sampled with:  $E_{J,t}/2\pi$  between (2 and 10) GHz,  $E_{C,t}/2\pi$  between (1.0 and 1.5) GHz, and  $E_{L,t}/2\pi$  between (0.1 and 2.0) GHz. Further, we retain only instances where  $E_{L,t}/E_{J,t}$  is between 0.1 and 0.5. We also fix  $J/2\pi = 100$  MHz since this leads to a  $\mu_{ZZ}/2\pi$  between (10 and 100) kHz in 90% of instances when uniformly sampling from this parameter space. The  $0 \rightarrow 3$  transition frequency  $\omega_t^{30}/2\pi$  exceeds 5 GHz in 99% of instances, when uniformly sampling. From Fig. 9, we conclude that exciting the target fluxonium to the 3 state is only possible in rare cases. For this reason, the only leakage channel we consider is the  $1 \rightarrow 2$  transition.

Let us first consider the contribution to the average gate infidelity due to the target fluxonium leaking into the 2 state when driving near  $\omega_d \approx \frac{1}{3}\omega_t^{21}$ , see Fig. 10. Because the 0 and 1 states are hybridized by the CR drive  $\omega_d = \omega_t^{10}$ , both initial states are equally likely to be scattered into the 2 state and the error is calculated

as the weighted sum of transition probabilities [80],

$$\frac{1}{4}(P^{00 \rightarrow 02} + P^{01 \rightarrow 02} + P^{10 \rightarrow 12} + P^{11 \rightarrow 12}). \quad (39)$$

In Fig. 10, the data points are projected down onto the span of the two axes and binned into a grid with each pixel taking the maximum value (error contribution) of its bin. The dotted vertical lines in Fig. 10 depicts the collision bounds from Table II for  $\Delta p = 0.8$ . Outside of the dotted bounds, the target-fluxonium leakage is mostly a narrow horizontal peak, as expected from Eq. (37). We notice, in particular, the cases when  $\omega_d/2\pi$  is near 1.070 GHz, 1.332 GHz or 1.472 GHz, which are subharmonics of the  $0 \rightarrow 2$ ,  $1 \rightarrow 2$  and  $1 \rightarrow 3$  transitions of the control qubit, respectively. Significant control-qubit leakage is expected, according to Fig. 8b, when the drive is insufficiently detuned from these subharmonics.

When the detuning between  $3\omega_d$  and  $\omega_t^{21}$  is at least  $\pm 15$  MHz (solid horizontal lines in Fig. 10a) the leakage error is mostly limited below  $10^{-4}$ , except near  $\omega_d/2\pi \approx \frac{1}{3}\omega_t^{21}/2\pi = 1.332$  GHz where a level-repulsion-like feature exists, “pushing” leakage out of the simple boundaries. This behavior is not predicted by Eq. (37). If a very small coupling strength  $J/2\pi = 10$  MHz is chosen instead, see Fig. 10b, the “level repulsion” is no longer significant. This suggests the feature arises from higher-order  $J$  corrections. A single collision bound uniform in  $\omega_d$  is insufficient to fully suppress leakage errors below  $10^{-4}$  for all parameters. However, for simplicity, we assume that excess leakage outside of our chosen bounds in

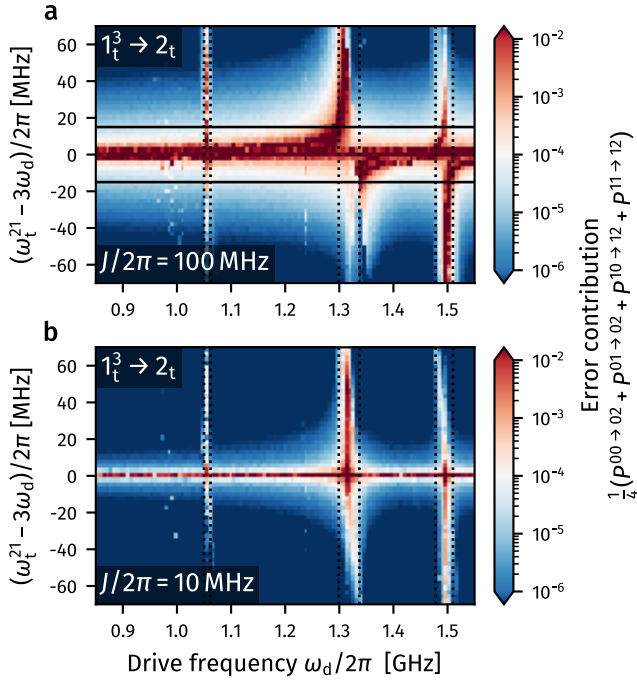


FIG. 10: Target-fluxonium leakage error induced by driving near the third subharmonic of its  $1 \rightarrow 2$  frequency. The CR drive is resonant with the target qubit,  $\omega_d = \omega_t^{10}$ . The vertical axis is the detuning between the transition frequency and the third drive harmonic. The default coupling strength is used in (a) while a weaker strength is used in (b), see lower-left label. **Solid** black lines in (a) define a  $\pm 15$  MHz detuning window, outside of which the error is (generally) below  $10^{-4}$ . **Dotted** black lines reproduce the collision windows from Table II for  $\Delta p = 0.8$ .

Fig. 9c is improbable so that we can keep using univariate bounds. We have, nonetheless, included additional padding around the strict  $10^{-4}$  threshold to mitigate underestimating the likelihood of this collision.

We similarly consider the leakage via the  $01 \rightarrow 12$  and  $11 \rightarrow 02$  transitions, see Figs. 11a and 11b, respectively. These likewise show errors resulting from driving near their fourth subharmonic frequency. The error contributions are, respectively,  $\frac{1}{4}(P^{10 \rightarrow 12} + P^{11 \rightarrow 12})$  and  $\frac{1}{4}(P^{00 \rightarrow 12} + P^{01 \rightarrow 12})$ . The data displayed here is for a higher drive amplitude, inducing  $\Delta p = 1.0$ , to intentionally overestimate this particular collision bound. The vertical axis is the detuning of the fourth drive harmonic  $4\omega_d$  from the bare transition frequency  $\omega_t^{21} \pm \omega_c^{10}$ . Because these transitions involve a control bitflip, the resonance frequency is Stark shifted from the bare frequency, which is why the vertical limits are not symmetric around zero. The collision bounds (solid lines) are curved because they are offset ( $\pm 10$  MHz) from the *Stark-shifted* transition frequency, which is both drive frequency and amplitude dependent.

The Stark shift on the control-qubit frequency is mono-

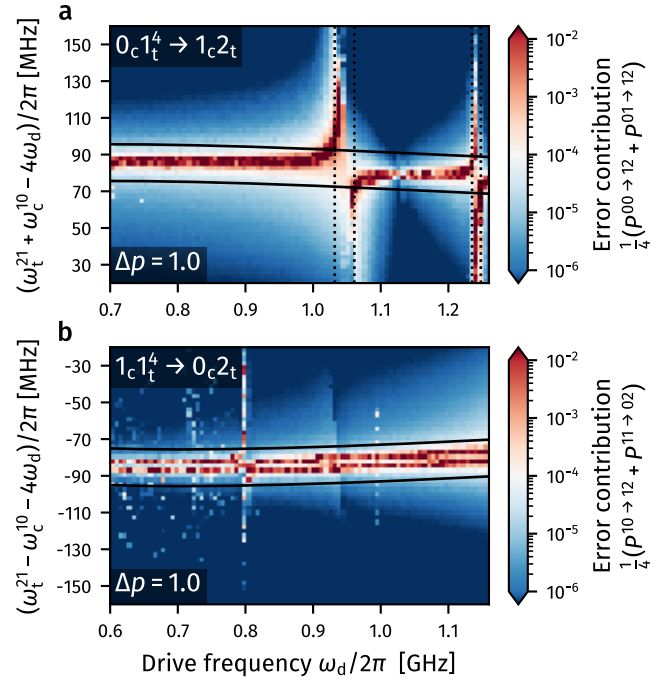


FIG. 11: Target-fluxonium leakage error assisted by (a) a control-qubit excitation and (b) control-qubit decay, induced by driving near the fourth subharmonic of its  $1 \rightarrow 2$  frequency, at a larger drive amplitude inducing  $\Delta p = 1.0$ . The vertical axis is the detuning between the *bare* transition frequency and the fourth drive harmonic. **Solid** black lines define a  $\pm 10$  MHz window centered on the *Stark-shifted* transition frequency. **Dotted** black lines reproduce the collision windows from Table II for  $\Delta p = 1.0$ .

tonic with drive amplitude (to an extent), or equivalently  $\Delta p$ . When  $\Delta p \geq 0.8$ , the qubit frequency shifts by approximately 10 MHz per 0.05 change in  $\Delta p$ . Therefore, the leakage frequency can be detuned from resonance by varying the plateau amplitude. Further, if the collision bounds were derived using  $\Delta p = 0.8$  (see Fig. 20 in Appendix I), they would be even narrower than  $\pm 10$  MHz. A change in  $\Delta p$  of  $\pm 0.05$  is therefore an overestimate. Hence, calibrating the amplitude to avoid these resonances (e.g., avoiding the leakage spike in Fig. 7b) should be straightforward and we do not include them in our final frequency collision model.

Lastly, the transition  $11 \rightarrow 02$  can also be driven at its second subharmonic frequency, but only when  $\omega_d/2\pi \gtrsim 1.1$  GHz. Since we aim to limit qubit frequencies below one gigahertz, it is unlikely this resonance condition will be met. Nevertheless, the detuning  $(\omega_t^{21} - \tilde{\omega}_c^{10} - 2\omega_d)/2\pi$  should be outside of the interval ( $-20$  to  $40$ ) MHz.

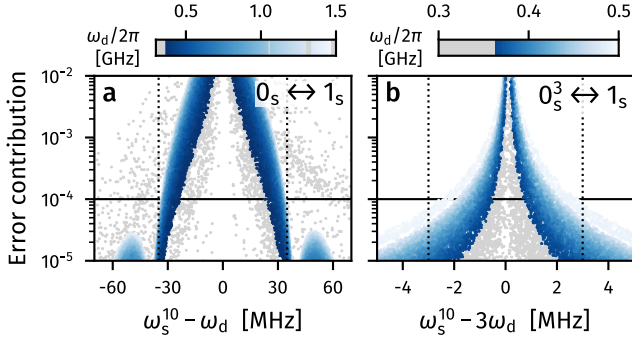


FIG. 12: Spectator bitflip error induced by driving nearly on resonance with (a) the spectator frequency and (b) its third subharmonic. The vertical axis is the error contribution  $\frac{1}{5}(P^{00 \rightarrow 01} + P^{01 \rightarrow 00} + P^{10 \rightarrow 11} + P^{11 \rightarrow 10})$ . The **blue shading** of the scatter points corresponds to the drive frequency, as indicated by the color bar above. The extracted collision bounds (**dotted vertical**) are: (a)  $\pm 35$  MHz and (b)  $\pm 3$  MHz.

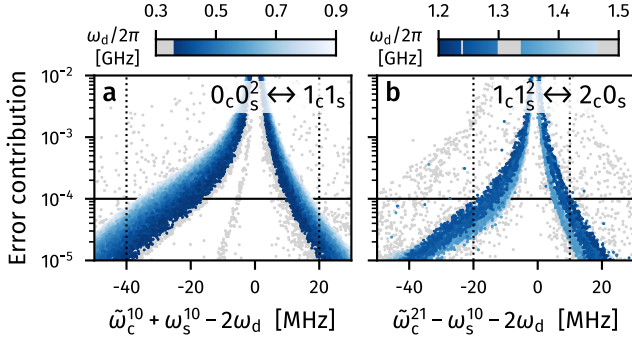


FIG. 13: (a) bSWAP error and (b) spectator-assisted control-leakage error induced when the detuning (horizontal axis) between the Stark-shifted transition frequency and the second drive harmonic is small. The vertical axis in (a) is  $\frac{1}{5}(P^{00 \rightarrow 11} + P^{11 \rightarrow 00})$  and in (b)  $\frac{1}{4}P^{11 \rightarrow 20}$ . The **blue shading** of the scatter points corresponds to the color bar. The extracted collision bounds (**dotted vertical**) are: (a)  $(-40$  to  $+20)$  MHz and (b)  $(-20$  to  $+10)$  MHz.

### E. Control–spectator resonances

The neighbors of a control qubit must have distinct frequencies so that a CR interaction can be enabled with one target while the other spectators ideally undergo an effective identity gate. When the control qubit is driven near the frequency of a spectator, bitflips on the spectator can contribute to the average infidelity of what should be the two-qubit identity. Considering the basis of the control and spectator qubits, we can quantify the infidelity

contribution as [80]

$$\frac{1}{5}(P^{00 \rightarrow 01} + P^{01 \rightarrow 00} + P^{10 \rightarrow 11} + P^{11 \rightarrow 10}), \quad (40)$$

shown in Fig. 12a as a function of drive detuning. Here, each scatter point represents a random spectator whose parameters are drawn from the same domain as the target fluxoniums previously, with a randomly assigned drive frequency. The drive amplitude is again chosen to induce  $\Delta p = 0.8$ . Points with a drive frequency within the collision bounds of Table II are colored gray. The collision bounds (vertical dotted lines) ignore the gray points and are determined to be  $\pm 35$  MHz.

As shown in Fig. 12b, when a spectator’s qubit frequency is far detuned from the CR drive, it can still be resonantly excited by its third harmonic. However, the collision bound,  $\pm 3$  MHz, is very small and this collision is unlikely to transpire since three times the lowest target-qubit frequency will often be over a gigahertz, where no qubits are nominally situated. Therefore, we exclude this resonance in our final collision model.

In addition to errors involving only spectator transitions, there is also the possibility joint control–spectator transitions. For instance, the second drive harmonic can unintentionally generate a bSWAP gate between the control and spectator qubits [55], the error incurred by this is  $\frac{1}{5}(P^{00 \rightarrow 11} + P^{11 \rightarrow 00})$ , see Fig. 13a. The extracted collision bounds for this error channel are  $(-40$  to  $+20)$  MHz. Because this interaction can be activated with a sub-gigahertz spectator by drive frequencies  $\omega_d/2\pi$  below  $\sim 600$  MHz, we unfortunately expect it to be a likely source of collisions.

A decay in the spectator qubit can induce leakage in the control qubit via  $11 \rightarrow 20$ , with collision bounds of  $(-20$  to  $+10)$  MHz between the second drive harmonic and the transition frequency, see Fig. 13b. This collision is unlikely for a control qubit with high anharmonicity since, with our chosen control-qubit parameters, the drive frequency  $\omega_d/2\pi$  needs to be at least 1.2 GHz.

Finally, spectator leakage driven by the third drive harmonic, or by the fourth harmonic and assisted by a control bitflip, has similar behavior to the equivalent channel for target fluxoniums, see Figs. 10 and 11. The error heatmaps are included in Appendix I as Fig. 20 for reference. We extract identical collision bounds of  $\pm 15$  MHz for the detuning  $(\omega_s^{21} - 3\omega_d)/2\pi$  and  $\pm 10$  MHz for  $(\omega_s^{21} \pm \tilde{\omega}_c^{10} - 4\omega_d)/2\pi$ . We do not consider the fourth-harmonic resonance to be a collision since, as previously argued, the resonance can be detuned by adjusting the plateau amplitude. This mitigation strategy should work in the presence of multiple spectators as long as their  $1 \rightarrow 2$  frequencies are spaced apart by tens of megahertz, otherwise tuning the amplitude can bring the drive onto resonance with another spectator’s leakage transition.

Further spectator errors are excluded from the final collision model because their collision bounds are either too small or involve improbably high qubit frequencies, see Appendix I.

## F. Zero-collision yield

An important consideration in fixed-frequency architectures with microwave activated gates is the onset of frequency collisions in larger systems. The case of transmons in a CR architecture has previously been studied using Monte Carlo simulations, which showed that the standard deviation in transmon frequencies must be less than 10 MHz (0.4% relative standard deviation in the critical current density) to effectively scale beyond a thousand qubits, even when targeting a gate error of just  $10^{-2}$  [71–73]. Such stringent fabrication precision is only achievable using junction annealing methods [72, 92, 93].

Here, we show the results of similar Monte Carlo simulations to assess whether frequency collisions ultimately limit the scalability of the fluxonium CR architecture, when targeting a gate error of  $10^{-4}$ . The probability of having zero frequency collisions (the zero-collision yield) is calculated for three different qubit connectivities: square, hexagonal and heavy-hexagonal. Their geometric arrangements and qubit frequency allocation patterns are shown in Fig. 14. The qubits alternate between control and target roles, with only a single low frequency control-qubit species. This ensures that no two adjacent qubits are strongly driven by a CR tone during parallel operation of CNOT gates, which could otherwise lead to additional multi-photon resonances not analyzed in this work. The collision windows from the previous sections let us quickly determine whether a high-fidelity CNOT gate is possible between a control qubit and any of its neighbors by comparing only their (Stark-shifted) transition spectra. Given a graph of connected fluxoniums, we can randomly perturb their nominal parameters and then check for frequency collisions in each control-qubit vertex neighborhood. Table III lists the final simplified collision windows used in the Monte Carlo simulations. Note that the dispersive shift of the 2 state by neighboring qubits is below one megahertz, which is far smaller than the collision bounds.

All three lattices support quantum error correction codes of arbitrarily large distances. However, the control qubit has 4 neighbors in the square lattice, 3 in the hexagonal lattice and 2 in the heavy-hex lattice. The reduced neighbor count is beneficial not only for decreasing the likelihood of frequency collisions, but also for reducing the sum of residual  $ZZ$  interactions and the capacitive loading on each fluxonium. To compare the yield more fairly across the different lattice types, we use the code distance as the common measure of lattice size. For defining the code distance, we use the rotated surface code for the square lattice [104–106] and a time-dynamic embedding of the surface code for the hexagonal lattice [107, 108]. Following Ref. [72], we use the heavy-hexagon code for the heavy-hex lattice, which has a similar (pseudo-)threshold as the surface code [71, 109].

Based on the findings of this work, we pick the nominal target-qubit parameters shown in Table IV. We choose a uniform inductive energy of  $E_{L,t}/2\pi = 1.0$  GHz and

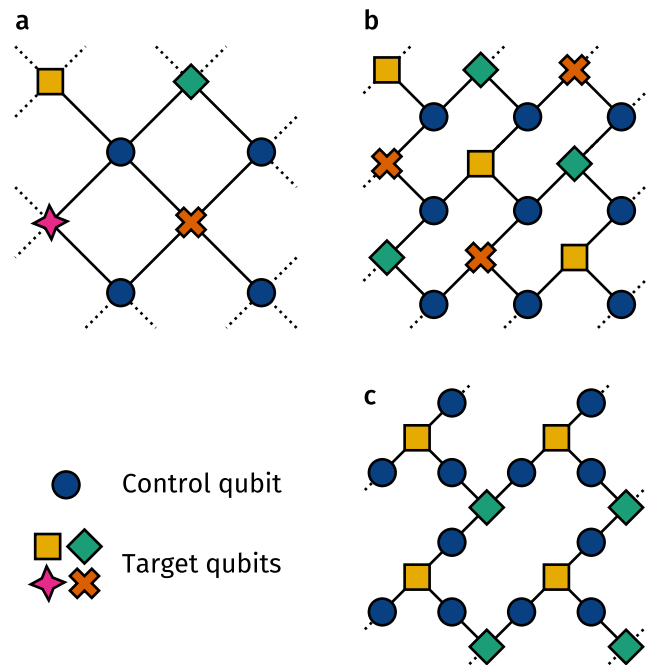


FIG. 14: Qubit frequency allocation on a unit cell of the (a) square lattice, (b) hexagonal lattice and (c) heavy-hex lattice. All control qubits have nominally the same parameters while there are up to four species of target qubits. Edges represent always-on capacitive connections and dotted lines are connections to the adjacent tiles.

vary the Josephson energy to adjust the qubit frequency. The charging energy for the target qubit is also fixed at  $E_{C,t}/2\pi = 1.0$  GHz. The control-qubit parameters remain as  $E_{J,c}/2\pi = 4.0$  GHz,  $E_{C,c}/2\pi = 1.2$  GHz and  $E_{L,c}/2\pi = 0.4$  GHz. The reasoning behind the parameters in Table IV is detailed in Appendix J.

As seen in Fig. 15, our proposed parameters can generally produce high-yield devices up to a distance of 21 for all three lattices considered, provided the relative standard deviation (RSD) in the Josephson energy,  $\sigma(E_J)/\langle E_J \rangle$ , is reasonably low. We assume the qubits'  $E_J$  are normally distributed and that the inductive energies  $E_L$  vary independently and normally with  $\sigma(E_L)/\langle E_L \rangle$  equal to one-tenth of  $\sigma(E_J)/\langle E_J \rangle$  [48]. The capacitive energies  $E_C$  are treated as static. For  $d = 3, 5$  and 21, both the square and hexagonal lattices have 17, 49 and 881 qubits, respectively, whereas the heavy-hex lattice has 23, 65 and 1121. Specifically, for a distance of 21 and a yield exceeding one-half, the RSD must be less than 1.0% for the square lattice, 1.2% for the hexagonal lattice and 2.0% for the heavy-hex lattice. According to Ref. [72], one thousand transmons in a heavy-hex arrangement requires an RSD below 0.3%. Again, we emphasize that our collision windows are derived using a significantly stricter error threshold of  $10^{-4}$ , compared to  $10^{-2}$  in Ref. [72].

Index	Transition	Detuning	Bounds/ $2\pi$ [MHz]
1	$0_i \leftrightarrow 1_i$	$\omega_j^{10} - \omega_d$	$-80, +\infty$
2	$1_i^3 \rightarrow 2_i$	$\tilde{\omega}_i^{21} - 3\omega_d$	$\pm 60$
3	$0_i^4 \rightarrow 2_i$	$\tilde{\omega}_i^{20} - 4\omega_d$	$\pm 80$
4	$0_i^5 \rightarrow 3_i$	$\tilde{\omega}_i^{30} - 5\omega_d$	$\pm 25$
5	$1_j^3 \rightarrow 2_j$	$\omega_j^{21} - 3\omega_d$	$\pm 15$
6	$1_i 1_j^2 \rightarrow 0_i 2_j$	$\omega_j^{21} - \tilde{\omega}_i^{10} - 2\omega_d$	$-20, +40$
7	$1_i 1_j^2 \rightarrow 2_i 0_j$	$\tilde{\omega}_i^{21} - \omega_j^{10} - 2\omega_d$	$-20, +10$
8	$0_k \leftrightarrow 1_k$	$\omega_k^{10} - \omega_d$	$\pm 35$
9	$0_i 0_k^2 \leftrightarrow 1_i 1_k$	$\tilde{\omega}_i^{10} + \omega_k^{10} - 2\omega_d$	$-40, +20$

TABLE III: Collision bounds of likely resonances. The label  $i$  refers to any control qubit in the lattice and  $j$  refers to any of its neighboring qubits. Another neighbor unequal to  $j$  is labeled  $k$ . A cross-resonance drive on  $i$  has frequency  $\omega_d$  which could be the qubit frequency of any of its neighbors. Collisions 1–4 involve only the control-qubit  $i$ , 5–7 involve also a neighbor  $j$  and 8 and 9 involve a spectator  $k \neq j$  with  $\omega_d = \omega_j^{10}$ . All bounds, except 1, 5 and 8, are expressed as detunings relative to the Stark-shifted resonance frequency.

#### Code distance

—  $d=21$     —  $d=5$     —  $d=3$

#### Lattice type

..... Square    - - - Hexagon    — Heavy-hex

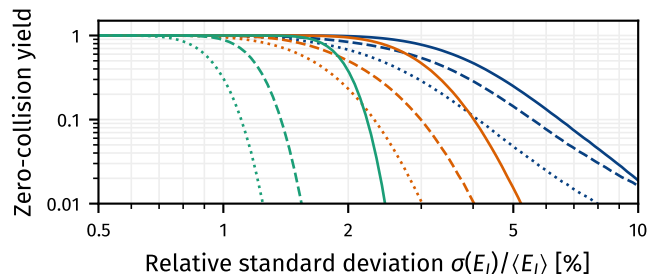


FIG. 15: Monte Carlo simulated zero-collision yield as a function of the relative standard deviation in the Josephson energies  $\sigma(E_J)/\langle E_J \rangle$ . The yield is calculated for code distances  $d = 21$  (green),  $d = 5$  (orange) and  $d = 3$  (blue) for the square lattice (dotted), hexagonal lattice (dashed) and heavy-hex lattice (solid). The data points represent the collision-free fraction of  $10^6$  samples.

Laser annealed transmon junctions have achieved RSD values below 0.5% [72, 93], which would comfortably lead to high-yield devices with our architecture, even for distance 21 layouts. Without post-fabrication tuning, the best room temperature junction resistance RSD is around 2% to 6% [72, 93–97], which is sufficient to reliably produce a distance 3 device. Note, however, that fluxoniums also have smaller junction areas than transmons, and as such, there may be a larger spread in the junction resistance by a factor of two to three [95–97].

Lattice	$E_{J,t}/2\pi$			$E_{C,t}/2\pi$		$E_{L,t}/2\pi$
	[GHz]	[GHz]	[GHz]	[GHz]	[GHz]	
Square	4.6	3.7	3.4	3.1	1.0	1.0
Hexagon	4.5	3.5	3.1		1.0	1.0
Heavy-hex	4.4	3.2			1.0	1.0

TABLE IV: Nominal target-qubit parameters used in the Monte Carlo simulation. The target-qubit frequencies are distributed between 422 MHz to 920 MHz. The control-qubit parameters are:  $E_{J,c}/2\pi = 4.0$  GHz,  $E_{C,c}/2\pi = 1.2$  GHz and  $E_{L,c}/2\pi = 0.4$  GHz, corresponding to a qubit frequency of 286 MHz.

Finally, we note that precise control over the fluxoniums’ inductive energies is not necessary. Only collision types 1, 8 and 9 of Table III contribute significantly to frequency crowding, and these collisions involve only the qubit frequencies. As long as the qubit frequency is tunable via single-junction annealing, scaling the fluxonium CR architecture up to a few thousand qubits will not be hindered by frequency collisions.

## V. CONCLUSION

In this work, we have shown that an all-fluxonium cross-resonance (CR) architecture leveraging only direct capacitive coupling provides a practical and easy to implement path toward larger multi-fluxonium processors. Despite the characteristically small charge dipole moment associated with low-frequency fluxonium qubits, our exploration indicates that a CR-based CNOT gate is generally achievable in 200 ns with a residual  $ZZ$  rate of 50 kHz. Meanwhile, the large anharmonicity of the fluxonium complements the microwave-activated CR architecture by mitigating frequency collisions. Assuming a Josephson energy disorder of 1% (achievable with junction annealing [72, 92, 93]), we find that zero-collision yields remain above 0.5 for square lattices supporting up to a distance-21 rotated surface code. This represents a substantial improvement over an all-transmon square lattice, where, for the same variation in Josephson energies, Ref. [72] calculated a yield below 0.01 already for the much smaller distance-3 layout. Beyond the scalability of the all-fluxonium CR architecture, calibrating the CR-based CNOT gate is also straightforward [57, 110]; our time-domain simulations of a two-fluxonium system show coherent errors comfortably below  $10^{-4}$  when using only soft square pulses.

Our study of the CR effect in the strong driving regime further revealed a universal saturation characteristic in the effective  $ZX$  strength, slightly exceeding the bare qubit-qubit exchange coupling rate  $J|n_c^{10}n_t^{10}|$ . This holds across a wide range of qubit-qubit detunings, provided the lower-frequency qubit acts as the control, in sharp contrast to the narrow straddling regime typically needed

for fast CR gates between transmons [88, 89]. However, the drive amplitude that saturates the  $ZX$  interaction can be up to five times larger than what is used in resonant single-qubit driving. This can lead to non-negligible heating and a degradation in qubit coherence [28, 83]. Such strong driving can also enable multiphoton resonances, which may induce leakage despite the large anharmonicity of the fluxonium. Nevertheless, we still find that the majority of frequency collisions arise from first-order resonances between closely spaced qubit frequencies, which could be effectively minimized by using spectral pulse shaping techniques [111–113].

As a blueprint for future experiments, we propose a lattice of alternating control and target qubits, where the higher-frequency targets serve as auxiliary qubits for parity measurements in a surface code or similar error-correction framework. The measurement fidelity of these higher-frequency auxiliary qubits can then be enhanced by using flux-pulse-assisted readout while avoiding errors from swapping with temporarily resonant neighbors [27].

## ACKNOWLEDGMENTS

The authors acknowledge support from the Dutch Research Council (NWO). Additionally, E.Y.H. acknowledges support from Holland High Tech (TKI).

## DATA AVAILABILITY

All numerical data are archived at 4TU.ResearchData [114] and the code used for generating and visualizing the data is available on GitHub [115].

## Appendix A: Capacitive–inductive drive symmetry

To argue that the results of the main text are independent of whether the control fluxonium is capacitively or inductively driven, we show the charge dipole moments between Floquet modes are *mostly* identical in both cases. The calculations here are carried out in the extended Hilbert space, where the time-periodic Hamiltonian, Eq. (2), is made time independent, see also Eq. (B8), by promoting the time parameter  $t$  to an operator  $\hat{\tau}$ . Its conjugate pair is the frequency operator  $-i\hat{\partial}_\tau$ . Together, they satisfy the canonical commutation relations (CCR) just like  $\hat{\varphi}$  and  $\hat{n}$ :  $[\hat{\tau}, -i\hat{\partial}_\tau] = [\hat{\varphi}, \hat{n}] = i$ . Only the control fluxonium *in isolation* is analyzed in this section, so the ‘c’ subscripts are dropped for simplicity.

The drive term of Eq. (B8) can be absorbed into the charge operator by redefining it as

$$\hat{n}' := \hat{n} + \frac{\Omega_{\text{cap}}}{8E_C} \sin(\omega_d \hat{\tau}), \quad (\text{A1})$$

where we add the subscript ‘cap’ to distinguish this amplitude from the inductive drive amplitude introduced

later. The Floquet Hamiltonian in terms of  $\hat{n}'$  is

$$\hat{\mathcal{H}} = \hat{H}'_0 - i\hat{\partial}_\tau + \frac{\Omega_{\text{cap}}^2}{32E_C} \cos(2\omega_d \hat{\tau}) - \frac{\Omega_{\text{cap}}^2}{32E_C}, \quad (\text{A2})$$

where  $\hat{H}'_0$  is the fluxonium Hamiltonian from Eq. (4) but with  $\hat{n}$  replaced by  $\hat{n}'$ . Because the term absorbed into  $\hat{n}'$  commutes with  $\hat{\varphi}$ , we preserve their CCR:  $[\hat{\varphi}, \hat{n}'] = i$ . However, the frequency operator should be redefined to

$$-i\hat{\partial}'_\tau := -i\hat{\partial}_\tau + \frac{\omega_d \Omega_{\text{cap}}}{8E_C} \cos(\omega_d \hat{\tau}) \hat{\varphi} + \frac{\Omega_{\text{cap}}^2}{32E_C} \cos(2\omega_d \hat{\tau}) \quad (\text{A3})$$

such that it commutes with  $\hat{n}'$ . The last term is included to eliminate the  $\cos(2\omega_d \hat{\tau})$  term in Eq. (A2), which is an unphysical coupling of different harmonics of the same Floquet mode. Its inclusion does not affect the commutativity between  $\hat{n}'$  and  $-i\hat{\partial}'_\tau$ . The Floquet Hamiltonian in terms of the redefined operators becomes

$$\hat{\mathcal{H}} = \hat{H}'_0 - i\hat{\partial}'_\tau + \Omega_{\text{ind}} \cos(\omega_d \hat{\tau}) \hat{\varphi} - 2E_C \left( \frac{\Omega_{\text{ind}}}{\omega_d} \right)^2, \quad (\text{A4})$$

where  $\Omega_{\text{ind}} := -\omega_d \Omega_{\text{cap}} / (8E_C)$  is a rescaled amplitude.

Given the operator pairs  $(\hat{\tau}, -i\hat{\partial}'_\tau)$  and  $(\hat{\varphi}, \hat{n}')$  satisfy the CCR, it follows from the Stone–von Neumann theorem that there exists a unitary  $\hat{U}$  such that [116]

$$\hat{U} \hat{\varphi} \hat{U}^\dagger = \hat{\varphi}, \quad \hat{U} \hat{\tau} \hat{U}^\dagger = \hat{\tau}, \quad (\text{A5a})$$

$$\hat{U} \hat{n}' \hat{U}^\dagger = \hat{n}, \quad \hat{U} (-i\hat{\partial}'_\tau) \hat{U}^\dagger = -i\hat{\partial}_\tau. \quad (\text{A5b})$$

In this case, the unitary can be formulated explicitly as

$$\hat{U} = \exp\left( \frac{i\Omega_{\text{cap}}}{8E_C} \sin(\omega_d \hat{\tau}) \hat{\varphi} + \frac{i\Omega_{\text{cap}}^2}{64E_C \omega_d} \sin(2\omega_d \hat{\tau}) \right). \quad (\text{A6})$$

By Eq. (A5), the transformed Hamiltonian  $\hat{\mathcal{K}} := \hat{U} \hat{\mathcal{H}} \hat{U}^\dagger$  has the same form as Eq. (A4) but with the primed operators replaced with their unprimed counterparts. Physically, this corresponds to inductive driving at a rescaled amplitude  $\Omega_{\text{ind}}$ , up to a global energy shift  $\propto (\Omega_{\text{ind}}/\omega_d)^2$ .

Let  $\epsilon_j + k\omega_d$  and  $|\Phi_{\text{cap}}^{j,k}\rangle$  for  $j \in \mathbb{N}_0, k \in \mathbb{Z}$  be eigenpairs of  $\hat{\mathcal{H}}$ . Since  $\hat{\mathcal{K}}$  is unitarily similar to  $\hat{\mathcal{H}}$ , it shares the same eigenspectrum but with transformed eigenstates,  $|\Phi_{\text{ind}}^{j,k}\rangle = \hat{U} |\Phi_{\text{cap}}^{j,k}\rangle$ . Let  $n_\beta^{[k]ji} = \langle\langle \Phi_\beta^{j,k} | \hat{n} | \Phi_\beta^{i,0} \rangle\rangle$  where  $\beta$  stands for ‘cap’ or ‘ind’. The matrix elements in the two bases can be related by sandwiching Eq. (A1) between bras and kets of the ‘cap’ basis to get

$$n_{\text{ind}}^{[k]ji} = n_{\text{cap}}^{[k]ji} - \frac{i\Omega_{\text{cap}}}{16E_C} \delta_{i,j} (\delta_{k,+1} - \delta_{k,-1}). \quad (\text{A7})$$

The elements only differ when  $i = j$  and  $k = \pm 1$ ; therefore, the relaxation rate, Eq. (25), is the same when calculated using either basis. Further,  $n_\beta^{[\pm 1]jj} - n_\beta^{[\pm 1]ii}$  is the same in either basis so the dephasing rate, Eq. (26), and conditional polarization, Eq. (15), are also unaffected.

On the contrary, the collision bounds of Table III do depend on the style of driving. The bounds for collision 8 depend on the magnitude of  $n_\beta^{[\pm 1]jj}$ ; and the bounds for collisions 1–4, involving only the control fluxonium, depend on the matrix elements of the drive operator (charge or phase) and the drive amplitude.

The equivalence between capacitive and inductive driving provides the freedom to choose either  $\hat{\mathcal{H}}$  or  $\hat{\mathcal{K}}$  when calculating the Floquet eigenstates. We find that, for the drive frequencies and amplitudes of interest, using the Hamiltonian with inductive driving requires a smaller Hilbert space to accurately compute the first few eigenstates [117, 118]. One rationale is that  $\hat{\varphi}$  couples the ground and first-excited states less strongly than  $\hat{n}$  does to the higher-excited states. Another justification comes from considering the energy offset proportional to  $(\Omega_{\text{ind}}/\omega_d)^2$  in Eq. (A4). For small  $\omega_d$ , the eigenenergies of  $\hat{\mathcal{H}}$  bend sharply as the drive amplitude increases, signaling increased mixing of basis states.

Finally, the apparent linear vanishing of  $\Delta p$  as  $\omega_d$  falls below the control-qubit frequency  $\omega_c$  can be elucidated in this section with a little further analysis. The relationship between the charge and phase matrix elements in the ‘ind’ eigenbasis can be derived from the commutation relation

$$[\hat{\varphi}, \hat{\mathcal{K}}] = i(8E_C)\hat{n}. \quad (\text{A8})$$

Evaluating the matrix elements in the ‘ind’ basis gives

$$\frac{i(\epsilon_j - \epsilon_i + k\omega_d)}{8E_C} \varphi_{\text{ind}}^{[k]ji} = n_{\text{ind}}^{[k]ji}, \quad (\text{A9})$$

which is a generalization of  $i\omega_c\varphi^{10}/(8E_C) = n^{10}$ . Define  $\Delta m := (\varphi_{\text{ind}}^{[1]11} - \varphi_{\text{ind}}^{[1]00})/\varphi^{10}$  as the magnetic analog to  $\Delta p$ . Equation (A9) implies that  $|\Delta p/\Delta m| = \omega_d/\omega_c$ . For  $\omega_d \ll \omega_c$ , the control qubit is magnetized adiabatically and  $\Delta m \approx 1$ . Hence, in the low drive frequency limit, we have  $|\Delta p| \approx \omega_d/\omega_c$ .

## Appendix B: Effective Hamiltonian derivation

In this section, we make the  $J$ -dependence of the system Hamiltonian in Eq. (1) explicit. For a fixed  $J \in \mathbb{R}$  and a time-dependent envelope  $\Omega(t)$ , the Schrödinger equation for the coupled system is

$$i\partial_t|\psi(t)\rangle = \hat{H}(J, \Omega(t), t)|\psi(t)\rangle. \quad (\text{B1})$$

Its solution is a path  $|\psi(t)\rangle$  in the combined Hilbert space  $\mathcal{H} = \mathcal{H}_c \otimes \mathcal{H}_t$ , where  $\mathcal{H}_q$  is the Hilbert space of qubit  $q$  in isolation. For a slowly varying envelope  $\Omega(t)$ , we might expect  $|\psi(t)\rangle$  to follow an adiabatic-like trajectory. However, standard adiabatic theory fails because the drive carrier  $\sin(\omega_d t)$  varies rapidly. Crucially though, since the carrier is periodic, its time-dependence can be separated from the envelope using Floquet theory [79].

By numerically solving the Floquet eigenproblem, constructed later, our approach enables a non-perturbative treatment of  $\Omega$ . Moreover, the derivation presented in this section provides a formal justification for the accuracy of the semi-analytical heuristic in Ref. [88]. Alternatively, a full perturbative treatment of both  $\Omega$  and  $J$  can be carried out using time-dependent Schrieffer–Wolff perturbation theory, as in Ref. [89].

### 1. Floquet theory in an extended Hilbert space

Consider a two-parameter Hamiltonian  $\hat{H}(J, \Omega(s), \tau)$ , where the time-dependence of the envelope and carrier has been separated into  $s$  and  $\tau$ , respectively. We can define the partial differential equation,

$$i(\partial_s + \partial_\tau)|\Psi(s, \tau)\rangle = \hat{H}(J, \Omega(s), \tau)|\Psi(s, \tau)\rangle, \quad (\text{B2})$$

whose solutions have the property that  $|\psi(t)\rangle = |\Psi(t, t)\rangle$  satisfies the original Schrödinger equation (B1) [79]. In addition, if  $|\Psi(s, \tau)\rangle$  is  $\tau$ -coperiodic with the Hamiltonian at some  $s$ ,  $|\Psi(s, \tau)\rangle = |\Psi(s, \tau + \frac{2\pi}{\omega_d})\rangle$ , then this property must extend to all  $s$ . This allows us to restrict the function space of Eq. (B2) to study only Fourier series solutions of the form

$$|\Psi(s, \tau)\rangle = \sum_{i,j \in \mathbb{N}_0} \sum_{k \in \mathbb{Z}} c_{ijk}(s) e^{ik\omega_d\tau} |ij\rangle \quad (\text{B3})$$

where  $c_{ijk}(s)$  are complex coefficients and  $\{|ij\rangle\}_{i,j \in \mathbb{N}_0}$  is the bare basis for  $\mathcal{H}$ .

One can view the complex exponentials  $\{e^{ik\omega_d\tau}\}_{k \in \mathbb{Z}}$  as a basis for an *auxiliary space*,  $\mathcal{T} := L^2([0, \frac{2\pi}{\omega_d}])$ , the space of  $(2\pi/\omega_d)$ -periodic square-integrable functions. In this context,  $|\Psi(s, \tau)\rangle$  is an  $s$ -parameterized path in the *extended Hilbert space*  $\mathcal{H}^{\text{ext}} := \mathcal{T} \otimes \mathcal{H}$  [119]. We adopt the double-ket notation to emphasize this point of view:

$$\mathcal{H}^{\text{ext}} \ni |\Psi(s)\rangle\rangle = \sum_{i,j \in \mathbb{N}_0} \sum_{k \in \mathbb{Z}} c_{ijk}(s) |e_k\rangle \otimes |ij\rangle, \quad (\text{B4})$$

where  $|e_k\rangle$  is simply the function  $(\tau \mapsto e^{ik\omega_d\tau}) \in \mathcal{T}$  in ket notation. The overlap of two states  $|\alpha\rangle\rangle, |\beta\rangle\rangle$  in  $\mathcal{H}^{\text{ext}}$  is inherited from its tensor product factors, so it is naturally

$$\langle\langle \alpha | \beta \rangle\rangle = \frac{\omega_d}{2\pi} \int_0^{\frac{2\pi}{\omega_d}} \langle \alpha(\tau) | \beta(\tau) \rangle d\tau. \quad (\text{B5})$$

In the extended Hilbert space, the two-time equation, Eq. (B2), is promoted to a genuine Schrödinger equation,

$$i\partial_s|\Psi(s)\rangle\rangle = \hat{\mathcal{H}}(J, \Omega(s))|\Psi(s)\rangle\rangle, \quad (\text{B6})$$

by defining the Floquet Hamiltonian  $\hat{\mathcal{H}} := \hat{H} - i\hat{\partial}_\tau$  where

$$\hat{\partial}_\tau := \sum_{k \in \mathbb{Z}} ik\omega_d |e_k\rangle\langle e_k| \quad (\text{B7})$$

acts on  $\mathcal{T}$ . The advantage of the extended space representation is that time-*dependent* Floquet modes become time-*independent* eigenstates of the Floquet Hamiltonian. Further, because  $\hat{\mathcal{H}}(J, \Omega)$  has no explicit time-dependence, the evolution is manifestly adiabatic if  $\Omega$  is slowly varying. As only the control qubit is driven, we can instead decompose the extended space as  $\mathcal{H}^{\text{ext}} = \mathcal{H}_c^{\text{ext}} \otimes \mathcal{H}_t$  where  $\mathcal{H}_c^{\text{ext}} := \mathcal{T} \otimes \mathcal{H}_c$ . The control qubit is then endowed with its own Floquet Hamiltonian,

$$\hat{\mathcal{H}}_c(\Omega) := \hat{H}_c^{\text{idle}} - i\hat{\partial}_\tau + \Omega \sin(\omega_d \hat{\tau}) \hat{n}_c, \quad (\text{B8})$$

where

$$\sin(\omega_d \hat{\tau}) = \frac{1}{2i} \sum_{k \in \mathbb{Z}} (|e_{k+1}\rangle \langle e_k| - |e_k\rangle \langle e_{k+1}|) \quad (\text{B9})$$

also acts on  $\mathcal{T}$ , and the total Floquet Hamiltonian can be reorganized as

$$\hat{\mathcal{H}} = \hat{\mathcal{H}}_c + \hat{H}_t + J \hat{n}_c \hat{n}_t. \quad (\text{B10})$$

This form lends itself to the direct application of time-independent perturbation theory. Once the eigensystems of  $\hat{\mathcal{H}}_c$  and  $\hat{H}_t$  are known, we can perturbatively incorporate the weak  $J$ -coupling to block-diagonalize  $\hat{\mathcal{H}}$ .

We adopt the conventional basis where  $\langle i | \hat{n}_q | j \rangle$  are purely imaginary. Consequently, the sinusoid in Eq. (B8) makes the Floquet Hamiltonian possess only real matrix elements in the *bare basis*,

$$\{|e_k\rangle \otimes |i\rangle \otimes |j\rangle \mid k \in \mathbb{Z} \text{ and } i, j \in \mathbb{N}_0\}, \quad (\text{B11})$$

i.e., it is manifestly time-reversal symmetric.

## 2. Semi-analytical block diagonalization

Let  $\{|\Phi_{j,k}(\Omega)\rangle\rangle\}_{j \in \mathbb{N}_0, k \in \mathbb{Z}}$  be instantaneous eigenstates of  $\hat{\mathcal{H}}_c(\Omega)$  with eigenvalues  $\epsilon_j(\Omega) + k\omega_d$ . The index  $j$  is defined such that the modes with  $k = 0$  are adiabatically connected to the undriven eigenstates:

$$|\Phi_{j,k=0}(\Omega = 0, \tau)\rangle\rangle := |j\rangle, \quad (\text{B12})$$

$$\epsilon_j(\Omega = 0) = E_c^j. \quad (\text{B13})$$

The phases of the  $\Omega \neq 0$  modes are chosen so that their Fourier coefficients in the bare basis remain real. Further, the  $k \neq 0$  modes are all defined to be in phase with the  $k = 0$  mode:

$$|\Phi_{j,k}(\Omega, \tau)\rangle\rangle := e^{ik\omega_d \tau} |\Phi_{j,0}(\Omega, \tau)\rangle\rangle. \quad (\text{B14})$$

Equations (B12) and (B14) uniquely fixes the Floquet eigenbasis, with the states automatically satisfying parallel transport,  $\langle\langle \Phi_{j,k}(\Omega) | \partial_\Omega | \Phi_{j,k}(\Omega) \rangle\rangle = 0$ , due to our phase choice [120].

The Floquet Hamiltonian in Eq. (B10) must be perturbatively block diagonalized because the target qubit

is resonantly driven by the CR pulse,  $\omega_d \approx E_t^1 - E_t^0$ . The eigensystem of  $\hat{\mathcal{H}}(J = 0, \Omega)$  therefore possesses a ladder of nearly-degenerate doublets:

$$|\uparrow_{j,k}(\Omega)\rangle\rangle := |\Phi_{j,k}(\Omega)\rangle\rangle \otimes |0\rangle, \quad (\text{B15a})$$

$$|\downarrow_{j,k}(\Omega)\rangle\rangle := |\Phi_{j,k-1}(\Omega)\rangle\rangle \otimes |1\rangle. \quad (\text{B15b})$$

These doublets also satisfy the parallel transport criteria within the subspace they span, i.e.,  $\langle\langle \sigma_{j,k} | \partial_\Omega | \varsigma_{j,k} \rangle\rangle = 0$  for  $\sigma, \varsigma \in \{\uparrow, \downarrow\}$ . This is because the diagonal entries,  $\sigma = \varsigma$ , are always zero by our phase convention and the off-diagonal entries are also zero because  $|0\rangle$  and  $|1\rangle$  are orthogonal.

A finite  $J$  coupling splits the near-degeneracies, mixing the bare doublets. Let  $\hat{S}(J, \Omega) = \sum_{n=1}^{\infty} J^n \hat{S}^{(n)}(\Omega)$  be the Schrieffer–Wolff (SW) generator that rotates the bare doublets into the dressed doublets:

$$|\uparrow/\downarrow_{j,k}(J, \Omega)\rangle\rangle := e^{-\hat{S}(J, \Omega)} |\uparrow/\downarrow_{j,k}(\Omega)\rangle\rangle, \quad (\text{B16})$$

such that

$$\mathcal{V}_{j,k}(J, \Omega) = \text{span}\{|\uparrow_{j,k}(J, \Omega)\rangle\rangle, |\downarrow_{j,k}(J, \Omega)\rangle\rangle\} \quad (\text{B17})$$

are invariant subspaces of  $\hat{\mathcal{H}}(J, \Omega)$ . Each  $(j, k)$ -block of the Hamiltonian is generally of the form

$$\hat{\mathcal{H}}_{j,k} = (\epsilon_j + \delta\epsilon_j + k\omega_d) + g_j \hat{X}_{j,k} + \frac{\Delta_d + \zeta_j}{2} \hat{Z}_{j,k}, \quad (\text{B18})$$

where

$$\hat{X}_{j,k} := |\downarrow_{j,k}\rangle\rangle \langle\langle \uparrow_{j,k} | + |\uparrow_{j,k}\rangle\rangle \langle\langle \downarrow_{j,k} |, \quad (\text{B19a})$$

$$\hat{Y}_{j,k} := i|\downarrow_{j,k}\rangle\rangle \langle\langle \uparrow_{j,k} | - i|\uparrow_{j,k}\rangle\rangle \langle\langle \downarrow_{j,k} |, \quad (\text{B19b})$$

$$\hat{Z}_{j,k} := |\downarrow_{j,k}\rangle\rangle \langle\langle \uparrow_{j,k} | - |\uparrow_{j,k}\rangle\rangle \langle\langle \downarrow_{j,k} | \quad (\text{B19c})$$

are the Pauli matrices in the dressed doublet basis (their dependence on  $J$  and  $\Omega$  have been omitted). Recall that  $\hat{\mathcal{H}}$  has only real matrix elements, which explains why  $\hat{Y}_{j,k}$  does not appear in the general form of each block, Eq. (B18). The interpretation of the coefficients are as follows. The parenthesized constant is the energy of the  $(j, k)$ -Floquet mode with a correction  $\delta\epsilon_j = O(J^2)$ . The induced Rabi rate on the target qubit is  $2g_j = O(J)$ , which may be positive or negative. The drive detuning from the bare target-qubit frequency is  $\Delta_d := \omega_d - (E_t^1 - E_t^0)$ . The control-dependent shift to the target-qubit frequency is  $\zeta_j = O(J^2)$ . Only  $g_j$  represents a resonant interaction and thus appears at first order. The non-resonant corrections  $\delta\epsilon_j$  and  $\zeta_j$  arise at second order.

The leading order contribution to  $g_j(J, \Omega)$  is simply

$$g_j(J, \Omega) = \langle\langle \downarrow_{j,0}(J, \Omega) | \hat{\mathcal{H}}(J, \Omega) | \uparrow_{j,0}(J, \Omega) \rangle\rangle \quad (\text{B20})$$

$$= J n_c^{10} n_t^{10} p_j(\Omega) + O(J^3), \quad (\text{B21})$$

where  $n_q^{10} := \langle 1 | \hat{n}_q | 0 \rangle$  and

$$p_j(\Omega) := \frac{1}{n_c^{10}} \langle\langle \Phi_{j,-1}(\Omega) | \hat{n}_c | \Phi_{j,0}(\Omega) \rangle\rangle \quad (\text{B22})$$

$$= \frac{1}{n_c^{10}} \frac{\omega_d}{2\pi} \int_0^{\frac{2\pi}{\omega_d}} \langle\langle \Phi_{j,0}(\Omega, \tau) | \hat{n}_c | \Phi_{j,0}(\Omega, \tau) \rangle\rangle e^{i\omega_d \tau} d\tau$$

is the charge expectation of the  $j$ th Floquet mode, oscillating at the frequency  $-\omega_d$  and normalized by  $n_c^{10}$ . Parity selection rules in  $\hat{n}_t$  forbid even powers of  $J$  from entering the perturbative expansion of  $g_j$ .

### 3. Parallel-transported basis

The dressed doublets satisfy parallel transport to first order in the  $J$ -direction. That is, for  $\sigma, \varsigma \in \{\uparrow, \downarrow\}$ ,

$$\langle\langle \sigma_{j,k}(J, \Omega) | \partial_J | \varsigma_{j,k}(J, \Omega) \rangle\rangle \quad (\text{B23})$$

$$= \langle\langle \sigma_{j,k}(0, \Omega) | e^{\hat{S}(J, \Omega)} \partial_J e^{-\hat{S}(J, \Omega)} | \varsigma_{j,k}(0, \Omega) \rangle\rangle \quad (\text{B24})$$

$$= \underbrace{\langle\langle \sigma_{j,k}(0, \Omega) | [-\hat{S}^{(1)}(J, \Omega) - 2J\hat{S}^{(2)}(J, \Omega)] | \varsigma_{j,k}(0, \Omega) \rangle\rangle}_{=0} + O(J^2). \quad (\text{B25})$$

The matrix element vanishes by virtue of the SW transformation being a direct rotation between degenerate subspaces, i.e., the bare doublets are in the kernel of  $\hat{S}^{(n)}$  for all orders [121]. Hence, the dressed doublets can alternatively be characterized as

$$|\uparrow/\downarrow_{j,k}(J, \Omega)\rangle\rangle = \hat{\Gamma}_{j,k}^A(J, \Omega) |\uparrow/\downarrow_{j,k}(0, 0)\rangle\rangle + O(J^3), \quad (\text{B26})$$

where  $\hat{\Gamma}_{j,k}^A(J, \Omega) : \mathcal{V}_{j,k}(0, 0) \rightarrow \mathcal{V}_{j,k}(J, \Omega)$  is an isomorphism of subspaces which parallel transports its input vector along a curve in the control space  $\{(J, \Omega) \in \mathbb{R}^2\}$ , defined as the polyline from  $(0, 0)$  to  $(0, \Omega)$  to  $(J, \Omega)$ . This is shown pictorially as the curve  $A$  in Fig. 16. Since Eq. (B23) vanishes up to  $O(J^2)$ , the discrepancy becomes  $O(J^3)$  in Eq. (B26) after integration over a length of  $J$ .

Another gauge choice performs the parallel transport  $\hat{\Gamma}_{j,k}^B$  along the other sides of the rectangle:  $(0, 0)$  to  $(J, 0)$  and then  $(J, \Omega)$ , see curve  $B$  in Fig. 16. We distinguish these states as the *primed* doublets,

$$|\uparrow'/\downarrow'_{j,k}(J, \Omega)\rangle\rangle := \hat{\Gamma}_{j,k}^B(J, \Omega) |\uparrow/\downarrow_{j,k}(0, 0)\rangle\rangle. \quad (\text{B27})$$

They satisfy, by construction, parallel transport along  $\Omega$ :

$$\langle\langle \sigma'_{j,k}(J, \Omega) | \partial_\Omega | \varsigma'_{j,k}(J, \Omega) \rangle\rangle = 0. \quad (\text{B28})$$

The naturalness of the primed doublets is apparent when considering the change of basis  $\hat{P}$ , whose  $(j, k)$ -blocks are

$$\hat{P}_{j,k}(J, \Omega) = \sum_{\sigma \in \{\uparrow, \downarrow\}} |\sigma_{j,k}(J, \Omega = 0)\rangle\rangle \langle\langle \sigma'_{j,k}(J, \Omega) |. \quad (\text{B29})$$

The inertial terms,  $i\hat{\Omega}\hat{P}_{j_1, k_1}\partial_\Omega\hat{P}_{j_2, k_2}^\dagger$ , introduced into the transformed Hamiltonian when  $\Omega$  is time-dependent vanish when  $(j_1, k_1) = (j_2, k_2)$  by virtue of Eq. (B28). The block-off-diagonal terms ( $j_1 \neq j_2$  or  $k_1 \neq k_2$ ) can be neglected by the adiabatic theorem provided they are much smaller than the inter-block energy gaps. The upshot is, in the adiabatic limit,  $\hat{P}$  may be regarded as a time-independent transformation.

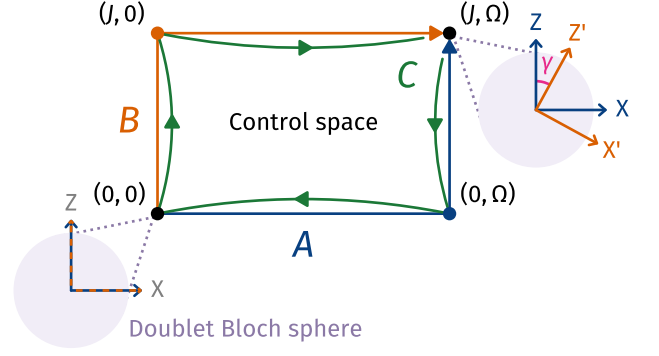


FIG. 16: Parallel transport of the nearly-degenerate doublets along different paths in control space. Transport along  $A$ , where  $\Omega$  is first increased followed by  $J$ , yields the **blue** axes in the Bloch sphere on the right. Transport along  $B$ , where  $J$  is first increased followed by  $\Omega$ , yields the primed **orange** axes. The primed axes are tilted relative to the unprimed axes by an angle  $\gamma$  (dependent on the control-qubit state). Parallel transport along the closed loop  $C$  rotates the unprimed axes into the primed axes.

Before transforming  $\hat{\mathcal{H}}$  by  $\hat{P}$ , we first establish the relationship between the primed and unprimed doublets. Let  $\hat{\Gamma}_{j,k}^C$  transform the unprimed to primed doublets:

$$|\uparrow'/\downarrow'_{j,k}(J, \Omega)\rangle\rangle =: \hat{\Gamma}_{j,k}^C(J, \Omega) |\uparrow/\downarrow_{j,k}(J, \Omega)\rangle\rangle. \quad (\text{B30})$$

Parallel transport, Eq. (B28), is satisfied if and only if, for  $\sigma, \varsigma \in \{\uparrow, \downarrow\}$ ,

$$\langle\langle \sigma_{j,k} | \hat{\Gamma}_{j,k}^{C\dagger}(\partial_\Omega \hat{\Gamma}_{j,k}^C) | \varsigma_{j,k} \rangle\rangle = -\langle\langle \sigma_{j,k} | \partial_\Omega | \varsigma_{j,k} \rangle\rangle. \quad (\text{B31})$$

This is essentially a two-by-two matrix differential equation and can be easily solved for  $\hat{\Gamma}_{j,k}^C$  up to an error of  $O(J^3)$ . First, note that the diagonal of the right-hand side is again zero due to normalization and the fact that the matrix elements are real. The off-diagonal term is

$$\begin{aligned} \langle\langle \uparrow_{j,k}(J, \Omega) | \partial_\Omega | \downarrow_{j,k}(J, \Omega) \rangle\rangle & \quad (\text{B32}) \\ & = -J \langle\langle \uparrow_{j,k}(\Omega) | [\partial_\Omega S^{(1)}(J, \Omega)] | \downarrow_{j,k}(\Omega) \rangle\rangle + O(J^3). \end{aligned}$$

Again, parity selection rules in  $\hat{n}_t$  forbid even powers of  $J$ . Define the integral over  $\Omega$  of the right-hand side as

$$\frac{\gamma_j(J, \Omega)}{2} := J \int_0^\Omega d\Omega' \langle\langle \uparrow_{j,k}(\Omega') | [\partial_{\Omega'} S^{(1)}(J, \Omega')] | \downarrow_{j,k}(\Omega') \rangle\rangle. \quad (\text{B33})$$

Equation (B31) can now be reformulated in a basis-independent way:

$$(\partial_\Omega \hat{\Gamma}_{j,k}^C) | \nu_{j,k} \rangle = -i \hat{\Gamma}_{j,k}^C \frac{\partial_\Omega \gamma_j}{2} \hat{Y}_{j,k} + O(J^3). \quad (\text{B34})$$

Its naive solution is

$$\hat{\Gamma}_{j,k}^C(J, \Omega) = \exp\left(-\frac{i\gamma_j}{2} \hat{Y}_{j,k}\right) + O(J^3), \quad (\text{B35})$$

which represents a rotation of  $\gamma_j$  around the  $Y$  axis of the Bloch sphere. Geometrically,  $\hat{\Gamma}_{j,k}^C(J, \Omega)$  is the holonomy acting on  $\mathcal{V}_{j,k}(J, \Omega)$  obtained by parallel transport around the rectangular loop, curve  $C$  in Fig. 16, with vertices, and in order:  $(J, \Omega)$ ,  $(0, \Omega)$ ,  $(0, 0)$ ,  $(J, 0)$ . This is also known as the Wilczek–Zee phase [122]. The loop collapses when  $\Omega = 0$  and we have, accordingly,  $\gamma_j = 0$  and  $\hat{\Gamma}_{j,k}^C$  acts trivially as expected.

The naive guess turns out to be correct despite  $\hat{Y}_{j,k}$  varying with  $\Omega$ . This is because  $\partial_\Omega \hat{Y}_{j,k}$  vanishes on  $\mathcal{V}_{j,k}$  for the following reasons. The operator  $i\hat{Y}_{j,k}$  is anti-Hermitian and has real matrix elements so  $i\partial_\Omega \hat{Y}_{j,k}$  must inherit this property. Since the dressed doublets are purely real and anti-Hermitian operators can only be imaginary along the diagonal, the diagonal of  $i\partial_\Omega \hat{Y}_{j,k}$  in the dressed doublet basis must be identically zero. A quick computation shows the off-diagonal also vanishes:

$$\begin{aligned} & \langle\langle \hat{\zeta}_{j,k} | (i\partial_\Omega \hat{Y}_{j,k}) | \hat{\zeta}_{j,k} \rangle\rangle \\ &= \langle\langle \hat{\zeta}_{j,k} | \partial_\Omega (i\hat{Y}_{j,k}) | \hat{\zeta}_{j,k} \rangle\rangle - \langle\langle \hat{\zeta}_{j,k} | i\hat{Y}_{j,k} \partial_\Omega | \hat{\zeta}_{j,k} \rangle\rangle \end{aligned} \quad (\text{B36})$$

$$= \langle\langle \hat{\zeta}_{j,k} | \partial_\Omega | \hat{\zeta}_{j,k} \rangle\rangle - \langle\langle \hat{\zeta}_{j,k} | \partial_\Omega | \hat{\zeta}_{j,k} \rangle\rangle, \quad (\text{B37})$$

where the last line is zero by our phase convention.

By analogy with the primed doublets, we can define the corresponding primed Pauli operators of Eq. (B30) as  $\hat{A}'_{j,k} := \hat{\Gamma}_{j,k}^C \hat{A}_{j,k} \hat{\Gamma}_{j,k}^{C\dagger}$  for  $A \in \{X, Y, Z\}$ . Because  $\hat{P}_{j,k}(J, \Omega)$  maps  $\hat{A}'_{j,k}(J, \Omega)$  to  $\hat{A}_{j,k}(J, 0)$ , it is helpful to first decompose the unprimed Pauli operators in terms of their primed counterparts as an intermediate step to transforming the Hamiltonian blocks:

$$\hat{X}_{j,k} = (1 - \frac{1}{2}\gamma_j^2)\hat{X}'_{j,k} + \gamma_j\hat{Z}'_{j,k} + O(J^3), \quad (\text{B38a})$$

$$\hat{Y}_{j,k} = \hat{Y}'_{j,k} + O(J^3), \quad (\text{B38b})$$

$$\hat{Z}_{j,k} = (1 - \frac{1}{2}\gamma_j^2)\hat{Z}'_{j,k} - \gamma_j\hat{X}'_{j,k} + O(J^3). \quad (\text{B38c})$$

It then follows that each block  $\hat{\mathcal{H}}_{j,k}$  transforms as

$$\hat{\mathcal{H}}_{j,k}^{\text{eff}}(J, \Omega) := \hat{P}_{j,k}(J, \Omega)\hat{\mathcal{H}}_{j,k}(J, \Omega)\hat{P}_{j,k}^\dagger(J, \Omega) \quad (\text{B39})$$

$$\begin{aligned} &= (\epsilon_j(\Omega) + \delta\epsilon_j(J, \Omega) + k\omega_d) \\ &+ g'_j(J, \Omega)\hat{X}'_{j,k}(J, 0) \\ &+ \frac{\Delta_d + \zeta'_j(J, \Omega)}{2}\hat{Z}'_{j,k}(J, 0) + O(J^3), \end{aligned} \quad (\text{B40})$$

where

$$g'_j(J, \Omega) := g_j(J, \Omega) - \frac{1}{2}\gamma_j(J, \Omega)\Delta_d, \quad (\text{B41})$$

$$\zeta'_j(J, \Omega) := \zeta_j(J, \Omega) + \gamma_j(J, \Omega)g_j(J, \Omega) \quad (\text{B42})$$

are modified rates due to the tilt of the unprimed  $X$  axis towards the primed  $Z$  axis, Eq. (B38). Importantly,  $\zeta'_j$  remains second order in  $J$ , so the axis correction does not change the perturbative order of the Hamiltonian coefficients. Although the drive detuning  $\Delta_d$  is non-perturbative, it is desirable to have it partially cancel

$\zeta'_j$  when implementing a CNOT gate. The induced Rabi rate  $g'_j$  is therefore unaffected to first order if we treat  $\Delta_d$  as a second-order term. We do not explicitly write down semi-analytic expressions for the second-order frequency shifts,  $\delta\epsilon_j$  and  $\zeta'_j$ , since they are not analyzed in this manuscript.

#### 4. Leaving the extended Hilbert space

The effective extended space Hamiltonian of Eq. (B40) is only physically relevant once we define how the states of the original space embed into the extended space. Consider an initial state  $|\Psi(0)\rangle\rangle$  in the subspace  $\mathcal{V}_{j=0,k=0}(J, 0) \oplus \mathcal{V}_{j=1,k=0}(J, 0)$ . We can parameterize its evolution in the basis of the undriven dressed doublets as

$$|\Psi(s)\rangle\rangle = \sum_{j \in \{0,1\}} c_{j,0}(s) |\hat{\zeta}_{j,0}(J, 0)\rangle\rangle + c_{j,1}(s) |\hat{\zeta}_{j,0}(J, 0)\rangle\rangle, \quad (\text{B43})$$

for complex coefficients  $c_{j,i}(s)$ . The diagonal trajectory  $|\psi(t)\rangle = |\Psi(t, t)\rangle\rangle$  in the original Hilbert space is then

$$|\psi(t)\rangle = \sum_{j \in \{0,1\}} c_{j,0}(t) |\tilde{j}0\rangle + c_{j,1}(t) e^{-i\omega_d t} |\tilde{j}1\rangle, \quad (\text{B44})$$

where the basis states are the dressed eigenstates of the coupled Hamiltonian, introduced in Section II A. (For consistency with the main text, the  $J$ -dependence of these states is omitted.) Define the time-dependent change of basis into the *cross-resonance frame*:

$$\hat{R}(t) := \exp\left(-\frac{i\omega_d t}{2} \tilde{I}\tilde{Z} + \frac{i\omega_d t}{2}\right), \quad (\text{B45})$$

where  $\hat{H}_{\text{CR}} := \hat{R}(\hat{H} - i\partial_t)\hat{R}^\dagger$  is the transformed Hamiltonian. A stationary target qubit in the CR frame precesses with frequency  $\omega_d$  in the lab frame, hence the state of Eq. (B44) transforms into

$$|\psi_{\text{CR}}(t)\rangle = \sum_{j \in \{0,1\}} c_{j,0}(t) |\tilde{j}0\rangle + c_{j,1}(t) |\tilde{j}1\rangle. \quad (\text{B46})$$

If we identify  $|\tilde{j}0\rangle \simeq |\hat{\zeta}_{j,0}(J, 0)\rangle\rangle$  and  $|\tilde{j}1\rangle \simeq |\hat{\zeta}_{j,0}(J, 0)\rangle\rangle$ , the CR frame solution is identical to Eq. (B43). Therefore, we can construct an effective Hamiltonian in the CR frame by directly taking the coefficients of Eq. (B40) for the  $k = 0$  band and projecting them onto the two-qubit Pauli basis, after which we obtain the Hamiltonian

$$\begin{aligned} \hat{H}_{\text{CR}}^{\text{eff}} &:= \left(\frac{g'_0 - g'_1}{2}\right) \tilde{Z}\tilde{X} + \left(\frac{g'_0 + g'_1}{2}\right) \tilde{I}\tilde{X} \\ &+ \left(\frac{\epsilon_0 + \delta\epsilon_0 - \epsilon_1 - \delta\epsilon_1}{2}\right) \tilde{Z}\tilde{I} + \left(\frac{\Delta_d}{2} + \frac{\zeta'_0 + \zeta'_1}{4}\right) \tilde{I}\tilde{Z} \\ &+ \left(\frac{\zeta'_0 - \zeta'_1}{4}\right) \tilde{Z}\tilde{Z}. \end{aligned} \quad (\text{B47})$$

This is essentially the same effective Hamiltonian as in Eq. (11) when  $\omega_d$  is equal to the average target-qubit

frequency  $\bar{\omega}_t$ . However, in the main text, we further subtract  $\bar{\omega}_c$  from the control-qubit frequency, leading to a shift in the  $ZI$  coefficient. This shift is trivial since a  $Z$  rotation on the control qubit commutes with the effective Hamiltonian.

We wish to emphasize that Eq. (B47) is an effective Hamiltonian in the sense that the following holds (up to global phase) on the computational subspace,

$$\begin{aligned} \mathcal{T} \exp\left(-i \int_{t_0}^{t_1} \hat{H}_{\text{CR}}^{\text{eff}}(J, \Omega(t)) dt\right) \\ \propto \mathcal{T} \exp\left(-i \int_{t_0}^{t_1} \hat{H}_{\text{CR}}(J, \Omega(t), t) dt\right), \end{aligned} \quad (\text{B48})$$

where  $\mathcal{T}$  indicates time ordering and  $\Omega(t_0) = \Omega(t_1) = 0$ .

### Appendix C: Double well renormalization

The potential energy for a fluxonium with inductive energy  $E_L$  and Josephson energy  $E_J$  at half-flux bias is

$$V_{E_L, E_J}(\varphi) := \frac{1}{2} E_L \varphi^2 + E_J \cos \varphi - E_J. \quad (\text{C1})$$

Contrary to convention, the extra  $-E_J$  is included to zero the potential energy at  $\varphi = 0$ . Instead of providing the inductive and Josephson energies, the double-well potential can alternatively be parameterized in terms of the interwell distance and barrier height. Let  $0 \leq a < \pi$  be the position of the first minima of the potential. It is related to the inductive-to-Josephson energy ratio transcendently through

$$\text{sinc } a = \frac{E_L}{E_J}, \quad (\text{C2})$$

where  $\text{sinc } x := \sin x/x$ . For the existence of at least two minima,  $E_L$  must be smaller than  $E_J$ . Typical fluxonium  $E_L/E_J$  ratios vary between 0.1 and 0.5 [23]. This corresponds to minimum positions in the range  $\frac{1}{2}\pi < a < \frac{11}{12}\pi$ . The depth  $b > 0$  of the two minima relative to zero is

$$b = -V_{E_L, E_J}(a) = E_J \left(1 - \cos a - \frac{a}{2} \sin a\right). \quad (\text{C3})$$

We can therefore reparameterize the fluxonium potential at half-flux bias in terms of  $a$  and  $b$  as

$$W_{a,b}(\varphi) := b \left[ \frac{\frac{1}{2}(\text{sinc } a)\varphi^2 + \cos \varphi - 1}{1 - \cos a - \frac{a}{2} \sin a} \right], \quad (\text{C4})$$

which equals  $V_{E_L, E_J}(\varphi)$  when Eqs. (C2) and (C3) hold.

For  $a \ll \pi$ , the wavefunction is confined to a region where the cosine is quartic. In this limit, the double-well potential is self-similar under simultaneous rescaling of  $a$  and  $\varphi$  since

$$W_{a,b}(\varphi) \approx b[(\varphi/a)^4 - 2(\varphi/a)^2]. \quad (\text{C5})$$

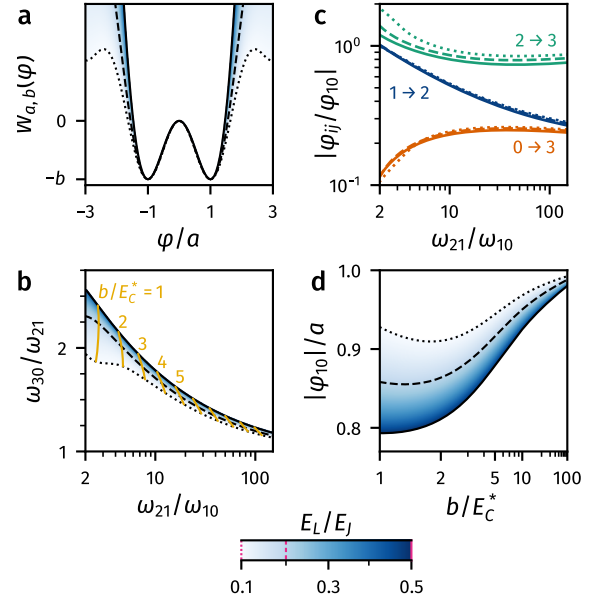


FIG. 17: (a) Comparison of the fluxonium double-well potential for varying  $E_L/E_J$  ratios and constant barrier height  $b$ . The horizontal axis is normalized by  $a$ . **Solid**, **dashed** and **dotted** traces correspond to  $E_L/E_J = 0.5$ ,  $0.2$  and  $0.1$ , respectively. The **blue gradient** interpolates between the discrete traces for intermediate  $E_L/E_J$  ratios with the corresponding scale given by the color bar at the bottom. (b) Ratio of the plasmon transition frequencies  $\omega_{30}/\omega_{21}$  as a function of  $\omega_{21}/\omega_{10}$ . **Yellow** contours denote lines of constant dimensionless barrier height  $b/E_C^*$ . (c) Normalized phase matrix elements  $|\varphi_{ij}/\varphi_{10}|$  as a function of  $\omega_{21}/\omega_{10}$ . (d) Qubit phase matrix element  $|\varphi_{10}|$ , normalized by half the interwell distance  $a$ , as a function of  $b/E_C^*$ .

For the typical inductive-to-Josephson energy ratios, the quartic approximation is crude. Figure 17a compares the potential landscape for  $E_L/E_J$  between 0.1 and 0.5 at a fixed barrier height  $b$ , with the  $\varphi$ -coordinate normalized by  $a$ . The solid, dashed and dotted traces represent the potential for  $E_L/E_J = 0.5$ ,  $0.2$  and  $0.1$ , respectively. Both potential curves for  $E_L/E_J = 0.5$  and  $0.2$  resemble a quartic double well in the region of interest. However,  $E_L/E_J = 0.1$  is qualitatively different as it has additional local minima near  $\varphi/a = \pm 3$ .

Figure 17b shows the relationship between the ratio of the plasmon transition frequencies  $\omega_{30}/\omega_{21}$ , and the ratio of the two lowest transition frequencies  $\omega_{21}/\omega_{10}$ . We see that  $\omega_{30}/\omega_{21}$  is well predicted by  $\omega_{21}/\omega_{10}$ , with increasing precision at larger values of  $\omega_{21}/\omega_{10}$ . The yellow contours denote lines of constant dimensionless barrier height  $b/E_C^*$ , where  $E_C^* := (\pi/a)^2 E_C$  is a renormalized charging energy, motivated by the squeezing of  $\varphi$  at larger  $E_L/E_J$ . Varying  $E_L/E_J$  at a fixed  $b/E_C^*$  only slightly varies  $\omega_{21}/\omega_{10}$ . Since the latter is directly measurable, it is a better defined characterization of the fluxonium

potential than the dimensionless barrier height  $b/E_C^*$ .

Figure 17c shows the magnitude of the phase matrix elements  $\varphi_{ij} := \langle i|\varphi|j\rangle$ , normalized by  $\varphi_{10}$ , as a function of  $\omega_{21}/\omega_{10}$  for  $E_L/E_J = 0.1, 0.2$  and  $0.5$ . Both  $\varphi_{21}/\varphi_{10}$  and  $\varphi_{30}/\varphi_{10}$  maintain very similar magnitudes across the three traces, indicating they are nearly independent of  $E_L/E_J$ . There is greater variation in  $\varphi_{32}/\varphi_{10}$ , as expected, since both 2- and 3-state wavefunctions are extended in  $\varphi/a$  and therefore sensitive to  $E_L/E_J$ . Figure 17d shows  $|\varphi_{10}|/a$  as a function of  $b/E_C^*$ . We see that  $\varphi_{10}$  scales roughly linearly with the minima position  $a$ , as expected. This approximation is more accurate in the heavy-fluxonium regime, where  $b/E_C^* > 10$ .

Our numerical study confirms the self-similarity predicted by Eq. (C5) holds well for typical fluxonium parameters. That is, the fluxonium eigenspectrum and relative phase matrix elements (for the first four levels) are only weakly dependent on  $E_L/E_J$ . Meanwhile, the absolute magnitude of the phase matrix elements scale approximately linearly with  $a$ .

The choice of  $E_L/E_J$  can be informed by the desire to minimize losses due to flux noise or quasiparticle tunneling through the array [24, 95, 123]. For a fixed qubit frequency and dimensionless barrier height  $b/E_C^*$ , Eq. (C3) implies that  $E_J$  scales approximately as  $a^{-4}$ , and by Eq. (C2),  $E_L$  scales as  $a^{-4} \text{sinc } a$ . Decay via flux noise or quasiparticle tunneling can be mitigated by decreasing  $E_L$  which implies increasing  $a$ , or equivalently, lowering  $E_L/E_J$ . Dielectric loss, in contrast, is largely independent of  $E_L/E_J$  since its rate is proportional to  $\varphi_{10}^2/E_C$ . For a fixed qubit frequency and  $b/E_C^*$ , the physical charging energy  $E_C$  scales as  $a^2$ , in the same way as  $\varphi_{10}^2$ .

#### Appendix D: Time-glide-reflection symmetry

The fluxonium Hamiltonian, Eq. (4), is invariant under parity inversion  $\hat{\mathcal{P}}$ , which maps the coordinate  $\varphi$  to  $-\varphi$ , when biased at half-flux quantum,  $\varphi_{\text{ext}} = \pi$ . We will only analyze the control fluxonium in this appendix, so we omit the ‘c’ subscripts for simplicity. The Hamiltonian with a time-periodic drive, Eq. (2), breaks parity symmetry because  $\hat{n}$  is odd under parity. However, the Hamiltonian is invariant under the combined transformation of a half-period translation in time followed by parity inversion:  $\hat{\mathcal{P}}\hat{H}(t + \pi/\omega_d)\hat{\mathcal{P}}^\dagger = \hat{H}(t)$ . This is also known as time-glide-reflection symmetry, in analogy with spatial glide reflection symmetry [124]. In the extended Hilbert space, time-glide-reflection is represented by the unitary transformation  $\hat{\mathcal{M}} = \exp(\pi\hat{\partial}_\tau/\omega_d)\hat{\mathcal{P}}$ . Likewise, the Floquet Hamiltonian, Eq. (B8), is invariant under  $\hat{\mathcal{M}}$ ; that is,  $\hat{\mathcal{M}}\hat{\mathcal{H}}\hat{\mathcal{M}}^\dagger = \hat{\mathcal{H}}$ . Since time-glide-reflection is self-inverse,  $\hat{\mathcal{M}}^2 = \hat{I}$ , its eigenvalues are either +1 or -1. The two eigenspaces of  $\hat{\mathcal{M}}$  are invariant subspaces of  $\hat{\mathcal{H}}$ , so it suffices to restrict our attention to only those eigenstates that are even under  $\hat{\mathcal{M}}$ .

To numerically obtain Floquet modes, one generally

first computes the time-evolution operator

$$\hat{U}(t_1, t_0) = \mathcal{T} \exp\left(-i \int_{t_0}^{t_1} \hat{H}(t) dt\right), \quad (\text{D1})$$

where  $\mathcal{T}$  indicates time ordering, over one full period,  $t_1 - t_0 = 2\pi/\omega_d$ . Then, solving the eigenequation

$$\hat{U}(t_0 + 2\pi/\omega_d, t_0)|\Phi_j(t_0)\rangle = e^{-i\epsilon_j(2\pi/\omega_d)}|\Phi_j(t_0)\rangle \quad (\text{D2})$$

produces the Floquet modes  $|\Phi_j(t)\rangle$  at  $t = t_0$  and their quasienergies  $\epsilon_j$ . The modes at later times can be reconstructed using

$$|\Phi_j(t_0 + t)\rangle = e^{i\epsilon_j t} \hat{U}(t_0 + t, t_0)|\Phi_j(t_0)\rangle. \quad (\text{D3})$$

Time-glide-reflection symmetric modes further satisfy

$$|\Phi_j(t_0)\rangle = \hat{\mathcal{P}}|\Phi_j(t_0 + \pi/\omega_d)\rangle. \quad (\text{D4})$$

Applying Eq. (D4) to Eq. (D3) when  $t = \pi/\omega_d$  gives

$$\hat{\mathcal{P}}\hat{U}(t_0 + \pi/\omega_d, t_0)|\Phi_j(t_0)\rangle = e^{-i\epsilon_j(\pi/\omega_d)}|\Phi_j(t_0)\rangle. \quad (\text{D5})$$

Solutions of this eigenequation are time-glide-reflection symmetric Floquet modes. Two benefits arise from this. First, the time-evolution operator only needs to be solved over half a period which is more computationally efficient. Second, accidental degeneracies between opposite parity modes are prevented because the quasienergies now wrap over  $2\omega_d$ . One drawback, however, is that  $|\Phi_j(t)\rangle$  can no longer connect to  $|j\rangle$  at zero drive amplitude since the odd excited states change sign under time-glide-reflection. In our calculations, we use an alternative convention where  $\epsilon_j + \omega_d$  for odd  $j$  correspond to the bare energy at zero drive.

#### Appendix E: Extra CNOT duration landscapes

In addition to the parameters in the main text, we have estimated the CNOT time for two fluxoniums with  $E_{L,q}/E_{J,q} = 0.25$ , detuned by  $(\omega_t^{10} - \omega_c^{10})/2\pi = 100$  MHz and 500 MHz, while fixing the sum of their frequencies at  $(\omega_c^{10} + \omega_t^{10})/2\pi = 1.3$  GHz, the same as in Section III B. The CNOT duration landscape for the small detuning case, Fig. 18a, is very similar to both panels of Fig. 5. For the larger detuning case, Fig. 18b, CNOT gates generally take longer but the overall trend remain similar for  $E_{J,c}/E_{C,c} > 3$ . For smaller  $E_{J,c}/E_{C,c}$ , the control qubit’s  $1 \rightarrow 2$  frequency lies closer to the target-qubit frequency, strengthening the residual ZZ interaction. Maintaining  $|\mu_{ZZ}|/2\pi$  at the 50 kHz threshold requires a reduction in  $J$ , which in turn increases the CNOT gate duration.

#### Appendix F: CNOT fidelity computation

When  $\mu_{IZ}$  and  $\mu_{ZZ}$  are both zero in the effective CR Hamiltonian, Eq. (11), the resulting gate takes the form

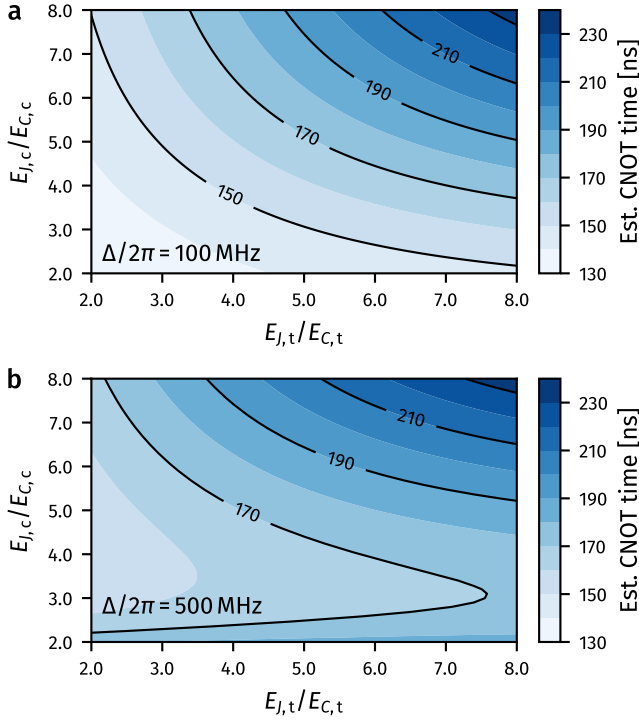


FIG. 18: Estimated CNOT time for two capacitively-coupled fluxonium qubits detuned by (a, b)  $\Delta/2\pi := (\omega_t^{10} - \omega_c^{10})/2\pi = (100, 500)$  MHz, for varying Josephson-to-charging energy ratios  $E_{J,q}/E_{C,q}$ . The sum of the two qubit frequencies is fixed at  $(\omega_c^{10} + \omega_t^{10})/2\pi = 1.3$  GHz, the inductive-to-Josephson energy ratio for both qubits is  $E_{L,q}/E_{J,q} = 0.25$  and the coupling strength  $J$  is determined by  $|\mu_{ZZ}|/2\pi = 50$  kHz.

of what we define to be an ideal CR unitary,

$$\hat{U}_{\text{CR}}(\chi, \theta, \phi) := \exp\left[-i\left(\frac{\chi}{2}\hat{Z}_c\hat{X}_t + \frac{\theta}{2}\hat{X}_t + \frac{\phi}{2}\hat{Z}_c\right)\right]. \quad (\text{F1})$$

For the purpose of this appendix, we set aside the distinction between dressed and bare states. The case  $\chi = \frac{\pi}{2}$  is locally equivalent to the CNOT gate, differing by only control-qubit  $Z$  and target-qubit  $X$  rotations. We view this to be a trivial difference, and therefore define a family of CNOT unitaries considered to be equivalent,

$$\hat{U}_{\text{CNOT}}(\theta, \phi) := \hat{U}_{\text{CR}}\left(\frac{\pi}{2}, \theta - \frac{\pi}{2}, \phi - \frac{\pi}{2}\right), \quad (\text{F2})$$

with the standard CNOT matrix given by  $\theta = \phi = 0$ , up to an overall phase. The average CNOT fidelity is then understood to mean the maximal average gate fidelity to  $\hat{U}_{\text{CNOT}}(\theta, \phi)$ , optimized over  $\theta$  and  $\phi$ :

$$F_{\text{CNOT}}(\hat{M}) := \max_{(\theta, \phi)} F(\hat{M}, \hat{U}_{\text{CNOT}}(\theta, \phi)), \quad (\text{F3})$$

where

$$F(\hat{M}, \hat{U}_0) = \frac{1}{20} [\text{Tr}(\hat{M}^\dagger \hat{M}) + |\text{Tr}(\hat{U}_0^\dagger \hat{M})|^2], \quad (\text{F4})$$

is a formula for calculating the average gate fidelity to an ideal two-qubit unitary  $\hat{U}_0$  [125]. The imperfect gate  $\hat{M}$  need not be unitary since it is usually obtained by truncating a unitary acting on the full Hilbert space to the computational subspace.

It follows from Eq. (F4) that the optimal angles  $\theta^*$  and  $\phi^*$  of Eq. (F3) satisfy

$$(\theta^*, \phi^*) = \arg \max_{(\theta, \phi)} |\text{Tr}(\hat{U}_{\text{CNOT}}^\dagger(\theta, \phi) \hat{M})|^2. \quad (\text{F5})$$

By decomposing the trace as

$$|\text{Tr}(\hat{U}_{\text{CNOT}}^\dagger(\theta, \phi) \hat{M})| = |z_+(\phi)e^{i\theta/2} + z_-(\phi)e^{-i\theta/2}| \quad (\text{F6})$$

where

$$z_\pm(\phi) := r_{0\pm}e^{i(\gamma_{0\pm} + \phi/2)} \pm r_{1\pm}e^{i(\gamma_{1\pm} - \phi/2)}, \quad (\text{F7})$$

$$r_{j\pm}e^{i\gamma_{j\pm}} := \langle j\pm | \hat{M} | j\pm \rangle, \quad (\text{F8})$$

we deduce the constraint  $\theta^* = \angle z_-(\phi^*) - \angle z_+(\phi^*)$ , which reduces Eq. (F5) to a one-dimensional maximization,

$$\phi^* = \arg \max_{\phi} \{|z_+(\phi)| + |z_-(\phi)|\}. \quad (\text{F9})$$

The magnitudes in Eq. (F9) in terms of  $r_{j\pm}$  and  $\gamma_{j\pm}$  are

$$|z_\pm(\phi)| = \sqrt{r_{0\pm}^2 + r_{1\pm}^2 \pm 2r_{0\pm}r_{1\pm} \cos(\phi - \delta_\pm)}, \quad (\text{F10})$$

where  $\delta_\pm := \gamma_{1\pm} - \gamma_{0\pm}$ . Equation (F9), in general, has no closed-form solution. However, if  $|j\pm\rangle$  are approximate eigenvectors of  $\hat{M}$ , we have  $r_{j\pm} \approx 1$  and this leads to

$$|z_+(\phi)| \approx 2 \left| \cos\left(\frac{\phi - \delta_+}{2}\right) \right|, \quad (\text{F11})$$

$$|z_-(\phi)| \approx 2 \left| \sin\left(\frac{\phi - \delta_-}{2}\right) \right|, \quad (\text{F12})$$

whose sum is maximized by

$$\phi^* \approx \delta_- + \frac{1}{2} \text{mod}(\delta_+ - \delta_-, 2\pi) + \frac{\pi}{2}, \quad (\text{F13})$$

where  $\text{mod}(x, y)$  is the modulo operator that wraps  $x$  within  $[0, y)$ . This approximation can then be used as an initial guess for solving Eq. (F9) iteratively.

In the presence of small  $\mu_{IZ}$  or  $\mu_{ZZ}$ , the final unitary will contain the Pauli products  $\hat{I}_c\hat{Z}_t$ ,  $\hat{Z}_c\hat{Z}_t$ ,  $\hat{I}_c\hat{Y}_t$  and  $\hat{Z}_c\hat{Y}_t$ . It is not possible to distinguish whether these errors originate from  $\mu_{IZ}$  or  $\mu_{ZZ}$  by examining the final unitary alone, as their effects are mixed by the dominant Hamiltonian terms. Hence, we refer to both contributions collectively as “phase error” in Fig. 7b.

### Appendix G: Effective energy spectral density derivation

The effective Hamiltonian of Eq. (11) is valid when only the target-qubit transition is resonantly driven. The

adiabatic theorem implies that off-resonant transitions do not induce population transfer in the instantaneous eigenbasis. Adiabaticity is violated when the instantaneous energy gaps narrow during the CR drive. This violation can occur in two ways. In the first case, ramping the drive too quickly leads to diabatic transitions between control-fluxonium eigenstates, as shown in Fig. 8b. In the second case, the control fluxonium *would* evolve adiabatically in the absence of coupling ( $J = 0$ ), but finite coupling permits joint transitions between control-fluxonium Floquet eigenstates and target-fluxonium eigenstates. Diabatic errors in the second case scale as  $O(J^2)$  and can be analyzed by building upon the semi-analytic framework developed in Appendix B.

### 1. Drive-activated scattering

As defined in Appendix B2, the Floquet Hamiltonian  $\hat{\mathcal{H}}_c(\Omega)$  has eigenstates  $\{|\Phi_{j,k}(\Omega)\rangle\rangle\}_{j \in \mathbb{N}_0, k \in \mathbb{Z}}$  with eigenvalues  $\epsilon_j(\Omega) + k\omega_d$ . Further, their phases are defined such that  $\text{Im}\langle\langle\Phi_{j,k}(\Omega)|\partial_\Omega|\Phi_{j,k}(\Omega)\rangle\rangle = 0$ . If the drive envelope  $\Omega(s)$  varies sufficiently slowly, the evolution of the driven control qubit *in isolation*, follows the adiabatic trajectory

$$\hat{U}_c(s_1, s_0) := \sum_{\substack{j \in \mathbb{N}_0 \\ k \in \mathbb{Z}}} \left\{ \exp\left(-i \int_{s_0}^{s_1} \epsilon_j(\Omega(s)) + k\omega_d ds\right) \times |\Phi_{j,k}(\Omega(s_1))\rangle\rangle\langle\langle\Phi_{j,k}(\Omega(s_0))|\right\}. \quad (\text{G1})$$

For the isolated target qubit, its evolution is simply

$$\hat{U}_t(s_1, s_0) := \sum_{j \in \mathbb{N}_0} \exp(-iE_t^j \times (s_1 - s_0)) |j\rangle\langle j|. \quad (\text{G2})$$

Our goal is to perturbatively study how the interaction  $J\hat{n}_c\hat{n}_t$  affects the joint evolution of the two qubits. To facilitate this, we move into an interaction picture where the isolated evolutions, Eqs. (G1) and (G2), are rendered static by transforming states from the Schrödinger picture by the unitary  $\hat{A}(s) := \hat{A}_c(s) \otimes \hat{A}_t(s)$  where

$$\hat{A}_q(s) := \hat{U}_q^\dagger(s, s_{\text{ref}}) \quad (\text{G3})$$

and  $s_{\text{ref}}$  is an arbitrary reference time when the drive is off,  $\Omega(s_{\text{ref}}) = 0$ . The full Hamiltonian, Eq. (B10), in this interaction picture is

$$\hat{\mathcal{H}}_I(s) := \hat{A}(s) [\hat{\mathcal{H}}(\Omega(s)) - i\partial_s] \hat{A}^\dagger(s) \quad (\text{G4})$$

$$\approx J [\hat{A}_c(s) \hat{n}_c \hat{A}_c^\dagger(s)] [\hat{A}_t(s) \hat{n}_t \hat{A}_t^\dagger(s)]. \quad (\text{G5})$$

The approximation in the last line follows from the adiabatic theorem, which states that

$$i\partial_s \hat{A}^\dagger(s) \approx \hat{\mathcal{H}}_0(\Omega(s)) \hat{A}^\dagger(s), \quad (\text{G6})$$

where  $\hat{\mathcal{H}}_0$  is the full Hamiltonian, Eq. (B10), with  $J = 0$ .

The true adiabatic limit is generally unattainable since small avoided crossings often appear in the quasienergy

spectrum (see, for example, Fig. 2d) [126, 127]. Very narrow gaps (e.g., less than  $2\pi \times 10$  MHz), are assumed to be traversed completely diabatically at the cost of introducing small discontinuities in the unitary of Eq. (G1). However, for ‘‘intermediate’’ gaps, the adiabatic approximation breaks down.

Let the evolution unitary of the coupled system in the interaction picture be

$$\hat{U}_I(s_1, s_0) = \mathcal{T} \exp\left(-i \int_{s_0}^{s_1} \hat{\mathcal{H}}_I(\Omega(s)) ds\right), \quad (\text{G7})$$

where  $\mathcal{T}$  indicates time ordering. Given two eigenstates of the idle Hamiltonian  $\hat{\mathcal{H}}(\Omega = 0)$ , say  $|\tilde{\text{in}}\rangle\rangle$  and  $|\tilde{\text{out}}\rangle\rangle$ , the probability  $|\tilde{\text{in}}\rangle\rangle$  is driven to  $|\tilde{\text{out}}\rangle\rangle$  is

$$P^{\text{in} \rightarrow \text{out}} := |\langle\langle\tilde{\text{out}}|\hat{U}_I(c, -c)|\tilde{\text{in}}\rangle\rangle|^2, \quad (\text{G8})$$

where  $c > 0$  is some arbitrary cutoff such that  $\Omega(s) = 0$  for  $|s| > c$ . The transition probability does not depend on the value of  $c$  because  $|\tilde{\text{in}}\rangle\rangle$  and  $|\tilde{\text{out}}\rangle\rangle$  are eigenstates of  $\hat{\mathcal{H}}(\Omega = 0)$ . To express Eq. (G8) in terms of bare eigenstates, we suppose the coupling strength  $J$  is adiabatically switched on by making the substitution  $J \mapsto w_{b,c}(s)J$  where  $w_{b,c}(s)$  is zero for  $|s| > c$  and ramps to unity for  $|s|$  smaller than another cutoff  $b < c$ . The new cutoff is still large enough such that  $\Omega(s) = 0$  for  $|s| > b$ . This ensures the fictitious tuning of  $J$  does not influence the drive-activated scattering process. The dressed states in Eq. (G8) are then replaced by their bare counterparts,  $|\text{in}\rangle\rangle$  and  $|\text{out}\rangle\rangle$ , which are eigenstates of the *uncoupled* idle Hamiltonian  $\hat{\mathcal{H}}_0(\Omega = 0)$ . By expanding Eq. (G7) as a Dyson series and assuming that  $|\text{in}\rangle\rangle$  and  $|\text{out}\rangle\rangle$  are orthogonal, we can compute the scattering probability to leading order as

$$P^{\text{in} \rightarrow \text{out}} = J^2 \left| \int_{-c}^c w_{b,c}(s) \langle\langle\text{out}|\hat{n}_{c,I}(s)\hat{n}_{t,I}(s)|\text{in}\rangle\rangle ds \right|^2, \quad (\text{G9})$$

where  $\hat{n}_{q,I} := \hat{A}_q \hat{n}_q \hat{A}_q^\dagger$  are the interaction-picture charge operators. (The equality in Eq. (G9), as well as in subsequent equations, should be understood to hold only to leading order in  $J$ .) In the limit  $b, c \rightarrow \infty$ , the integral can be replaced by a Fourier transform:

$$P^{\text{in} \rightarrow \text{out}} = J^2 |\mathcal{F}[\langle\langle\text{out}|\hat{n}_{c,I}(s)\hat{n}_{t,I}(s)|\text{in}\rangle\rangle](0)|^2, \quad (\text{G10})$$

where the Fourier transform is defined as  $\mathcal{F}[f(s)](\omega) = \int_{-\infty}^{\infty} f(s) e^{-i\omega s} ds$  for convergent improper integrals [128].

To utilize Eq. (G10) semi-analytically, suppose  $|\text{in}\rangle\rangle$  and  $|\text{out}\rangle\rangle$  are simple product states of the form  $|ij^k\rangle\rangle := |e_k\rangle \otimes |i\rangle \otimes |j\rangle$ . Since the Floquet Hamiltonian is invariant up to a global energy shift under the discrete translation  $|e_k\rangle \mapsto |e_{k+l}\rangle$ , it suffices to consider ‘in’ states of the form  $|ij^0\rangle\rangle$  and ‘out’ states of the form  $|fg^k\rangle\rangle$ . Equation (G10) then becomes

$$P^{ij^0 \rightarrow fg^k} = J^2 |n_t^{gj}|^2 |\tilde{n}_{c,I}^{[k]fi}(-\omega_t^{gj})|^2, \quad (\text{G11})$$

where  $\tilde{n}_{c,I}^{[k]fi}(\omega) := \mathcal{F}[n_{c,I}^{[k]fi}(s)](\omega)$  is the Fourier transform of  $n_{c,I}^{[k]fi} := \text{Tr}(\hat{n}_{c,I}|e_0\rangle\langle e_k| \otimes |i\rangle\langle f|)$ . This expression can be simplified by summing over the output indices:

$$P^{ij \rightarrow *k} := \sum_{f,g \in \mathbb{N}_0} \sum_{k \in \mathbb{Z}} P^{ij^0 \rightarrow fg^k} \quad (\text{G12})$$

$$= J^2 \sum_{g \in \mathbb{N}_0} |n_t^{gj}|^2 \mathcal{E}_i(-\omega_t^{gj}), \quad (\text{G13})$$

where

$$\mathcal{E}_i(\omega) := \sum_{k \in \mathbb{Z}} \sum_{f \in \mathbb{N}_0} |\tilde{n}_{c,I}^{[k]fi}(\omega)|^2 \quad (\text{G14})$$

is the *effective energy spectral density* for the control-qubit charge operator, when the qubit is in the  $i$  state. The summand in Eq. (G12) is zero when  $i = f$ ,  $j = g$  and  $k = 0$ , so  $P^{ij \rightarrow *k}$  equals the probability for an initial  $|ij^0\rangle$  to scatter to any *orthogonal* final state.

Since the target is resonantly driven, the non-separable states  $|i\pm^k\rangle := (|i0^k\rangle \pm |i1^{k-1}\rangle)/\sqrt{2}$  are also good ‘in’ and ‘out’ eigenstates. However, there is a minor subtlety in the calculation of  $P^{i+ \rightarrow *}$ , the scattering probability for a target qubit in the ‘+’ state. If the final state is an orthogonal product state, this probability is simply

$$P^{i+^0 \rightarrow fg^k} = \frac{1}{2} (P^{i0^0 \rightarrow fg^k} + P^{i1^0 \rightarrow fg^k}). \quad (\text{G15})$$

However, if the final state is  $|f\pm^k\rangle$ , the probability is

$$P^{i+^0 \rightarrow f\pm^k} = \frac{1}{4} (P^{i0^0 \rightarrow f1^{k-1}} + P^{i1^0 \rightarrow f0^{k+1}}) \pm \frac{J^2 |n_t^{10}|^2}{2} \text{Re} \left\{ \tilde{n}_{c,I}^{[k+1]fi}(\omega_t^{10}) \tilde{n}_{c,I}^{[k-1]fi}(-\omega_t^{10}) \right\}. \quad (\text{G16})$$

For the special case  $i = f$  and  $k = 0$ , we have

$$P^{i+^0 \rightarrow i\pm^0} = \frac{1}{2} P^{i0^0 \rightarrow i1^{-1}} \pm \frac{J^2 |n_t^{10}|^2}{2} \text{Re} \left\{ \tilde{n}_{c,I}^{[-1]ii}(-\omega_t^{10})^2 \right\}. \quad (\text{G17})$$

This can be simplified by noting that the reference time  $s_{\text{ref}}$  in Eq. (G3) is arbitrary. We can therefore choose  $s_{\text{ref}}$  such that the Fourier amplitude  $\tilde{n}_{c,I}^{[-1]ii}(-\omega_t^{10})$  is purely real, leading to the simplification  $P^{i+^0 \rightarrow i+^0} = P^{i0^0 \rightarrow i1^{-1}}$  and  $P^{i+^0 \rightarrow i-^0} = 0$ . We now have all the ingredients needed to sum  $P^{i+^0 \rightarrow \text{out}}$  over orthogonal ‘out’ states, which yields

$$P^{i+ \rightarrow *} = \frac{1}{2} (P^{i0 \rightarrow *} + P^{i1 \rightarrow *}) - P^{i0^0 \rightarrow i1^{-1}}. \quad (\text{G18})$$

If we assume  $\mathcal{E}_i(\omega)$  has only localized peaks centered on the transition energies between Floquet eigenstates, and that no accidental resonances exist, we can use the approximation  $\mathcal{E}_i(-\omega_t^{10}) \approx |\tilde{n}_{c,I}^{[-1]ii}(-\omega_t^{10})|^2$  to express Eq. (G18) also in terms of the effective ESD:

$$P^{i+ \rightarrow *} = \frac{J^2}{2} \sum_{g=2}^{\infty} \sum_{j=0}^1 |n_t^{gj}|^2 \mathcal{E}_i(-\omega_t^{gj}). \quad (\text{G19})$$

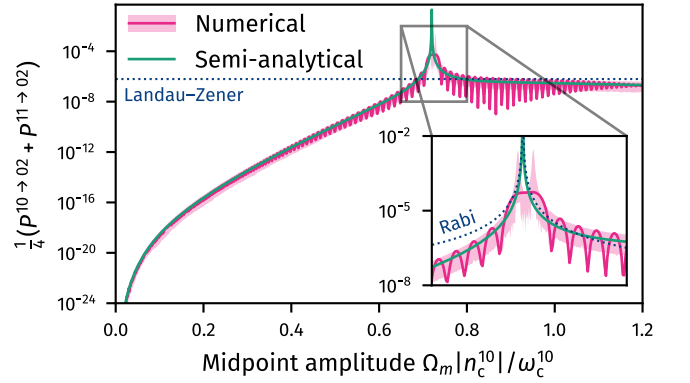


FIG. 19: Leakage error from Fig. 7b, shown in **solid pink**, for a calibrated CNOT gate between fluxonium qubits with parameters given in Table I. The **filled light pink** area shows the 90th percentile leakage error for a soft square CR pulse with plateau duration uniformly sampled up to 1 ms, and the same ramp duration and carrier frequency as the calibrated CNOT pulse. The **solid green** line uses the semi-analytic formula, Eq. (G11), to compute the leakage probabilities. The **dotted** lines correspond to predictions from the Landau-Zener formula and, in the inset, Rabi’s formula.

This sum is equal to the *leakage* probability of the target qubit, averaged over its initial qubit states. The formula is unchanged if the target qubit is initially in the ‘-’ state, that is,  $P^{i- \rightarrow *} = P^{i+ \rightarrow *}$ .

## 2. Comparison with numerical simulations

In Fig. 19, we compare the semi-analytic prediction of Eq. (G11), in solid green, to the leakage error first shown in Fig. 7b, reproduced here in solid pink. Leakage induced by the CR pulse depends on the exact pulse duration due to interference effects, resulting in visible ripples in the solid pink curve. To smooth over these transient features, we also show in filled light pink, the 90th-percentile range of leakage errors for a soft square CR pulse with a plateau duration uniformly sampled up to 1 ms, and the same ramp duration and carrier frequency as the calibrated CNOT pulse. In the semi-analytic calculation, the drive envelope is assumed to have an infinitely long plateau, which also eliminates transient effects. Computing the spectrum of a function with an infinitely long plateau is discussed in Appendix H. Away from resonance, the semi-analytical calculation agrees with the fully numerical result over many orders of magnitude, confirming its high accuracy. Near resonance (see inset) it qualitatively deviates from the numerical result, predicting only a single peak rather than the two observed numerically. The two peaks originate from the Rabi splitting of  $|1+^k\rangle$  and  $|1-^k\rangle$ , a feature not captured by leading-order perturbation theory.

Using Eq. (G11) requires numerically computing the

Fourier transform of interaction-picture matrix elements, a procedure that is technically involved. A simpler model treats the leakage process instead as adiabatic traversal of an avoided crossing in the Floquet quasienergy spectrum. Let the detuning between  $|11^4\rangle$  and  $|02^0\rangle$  be denoted by

$$\Delta(\Omega) = [\epsilon_1(\Omega) - \epsilon_0(\Omega) + 4\omega_d] - \omega_t^{21}, \quad (\text{G20})$$

and let  $\Omega_{\text{AC}}$  be the amplitude at the avoided crossing, which we define as minimizing  $|\Delta|$ . In this case,  $\Omega_{\text{AC}}|n_c^{10}/\omega_c^{10} = 0.72$  and  $|\Delta(\Omega_{\text{AC}})|/2\pi = 50$  kHz. The diabatic traversal probability can be approximated using the Landau-Zener formula [103]

$$P_{\text{LZ}} = \exp\left(-2\pi \frac{|\Delta(\Omega_{\text{AC}})|^2}{4v}\right), \quad (\text{G21})$$

where  $v = |\dot{\Omega} \times (d\Delta/d\Omega)(\Omega_{\text{AC}})|$  is the Landau-Zener velocity, which we approximate by assuming the slope of the envelope at the avoided crossing is  $\dot{\Omega} \approx \Omega_{\text{AC}}/t_r$ . Since the avoided crossing is traversed twice, once during each ramp of the pulse, the final leakage probability is  $P^{11 \rightarrow 02} \approx 2P_{\text{LZ}}(1 - P_{\text{LZ}})$  [103]. This approximation is shown as the dotted horizontal line in Fig. 19 and roughly matches the numerical result when the avoided crossing is fully traversed ( $\Omega_m > \Omega_{\text{AC}}$ ).

The Landau-Zener formula is inaccurate if the system dwells near the avoided crossing ( $\Omega_m \approx \Omega_{\text{AC}}$ ). In this case, we turn to the standard Rabi oscillation formula,

$$P^{11 \rightarrow 02}(\Omega_m) \approx \frac{|\Delta(\Omega_{\text{AC}})|^2}{4|\Delta(\Omega_m)|^2 + |\Delta(\Omega_{\text{AC}})|^2}. \quad (\text{G22})$$

We further simplify  $\Delta(\Omega_m)$  by Taylor-expanding  $\Delta(\Omega)$  to linear order around  $\Omega = \Omega_{\text{AC}}$ , making Eq. (G22) a Lorentzian in  $\Omega_m$ . The Rabi approximation is shown as the dotted curve in the inset of Fig. 19 and agrees well with the semi-analytical result when very close to resonance, but overestimates the error for  $\Omega < \Omega_{\text{AC}}$  and underestimates for  $\Omega > \Omega_{\text{AC}}$ .

## Appendix H: Infinite soft square pulse spectrum

The definition of the effective ESD contains the Fourier transform of terms like  $f(s) = a(s)e^{i\phi(s)}$ , where

$$a(s) = \langle\langle \Phi_{j,k}(\Omega(s)) | \hat{n}_c | \Phi_{i,0}(\Omega(s)) \rangle\rangle \quad (\text{H1})$$

is a charge matrix element in the instantaneous Floquet eigenbasis and

$$\phi(s) = \int_{s_{\text{ref}}}^s \Delta(\Omega(s')) ds', \quad (\text{H2})$$

$$\Delta(\Omega) = \epsilon_j(\Omega) - \epsilon_i(\Omega) - k\omega_d \quad (\text{H3})$$

is the dynamical phase accumulated by the interaction-picture matrix element and the Stark-shifted transition frequency, respectively. As we ultimately only care about

the spectral density, we set  $s_{\text{ref}} = 0$ , since this only affects the overall phase of  $f(s)$ . Let the drive envelope be a symmetric soft square pulse with plateau duration  $2\tau$  and midpoint amplitude  $\Omega_m$ , we express this as

$$\Omega(s) = \Omega_m [\mathcal{R}(s - \tau) + \mathcal{R}(-s - \tau) - 1], \quad (\text{H4})$$

where  $\mathcal{R}(s)$  is a ramp function that smoothly interpolates between  $\mathcal{R}(-\infty) = 1$  and  $\mathcal{R}(+\infty) = 0$  over a characteristic ramp duration; e.g., Eq. (31). We seek to compute the ESD of  $f(s)$  averaged over long  $\tau$ , such that the sinc ripples in the spectrum are also averaged away. This is not straightforward to directly calculate numerically, so we first perform a series of analytic transformations to relate the  $\tau$ -averaged spectrum to the spectrum of a compactly supported signal.

In the long  $\tau$  limit, we have the pointwise convergence

$$\lim_{\tau \rightarrow \infty} \Omega(s + \tau) = \Omega_m \mathcal{R}(s), \quad (\text{H5})$$

which implies

$$b(s) := \lim_{\tau \rightarrow \infty} a(s + \tau), \quad (\text{H6})$$

$$\theta(s) := \lim_{\tau \rightarrow \infty} \{\phi(s + \tau) - \phi(\tau)\} \quad (\text{H7})$$

are both well defined and given by

$$b(s) = \langle\langle \Phi_{j,k}(\Omega_m \mathcal{R}(s)) | \hat{n}_c | \Phi_{i,0}(\Omega_m \mathcal{R}(s)) \rangle\rangle, \quad (\text{H8})$$

$$\theta(s) = \int_0^s \Delta(\Omega_m \mathcal{R}(s')) ds'. \quad (\text{H9})$$

Define  $g(s) := b(s)e^{i\theta(s)}$ . For long  $\tau$ , we have

$$f(s + \tau) \approx g(s)e^{i\phi(\tau)} \approx g(s)e^{i[\Delta(\Omega_m)\tau + \delta]}, \quad (\text{H10})$$

where  $\delta := \lim_{\tau \rightarrow \infty} \{\phi(\tau) - \Delta(\Omega_m)\tau\}$ . At first sight, it appears this equation establishes a relation between  $\mathcal{F}[f(s)](\omega)$  and  $\mathcal{F}[g(s)](\omega)$ , however, it only holds for  $s$  greater than a finite lower bound when  $\tau$  is fixed. To address this, we perform the transformation

$$f_1(s) := \left( \Delta(\Omega_m) + i \frac{d}{ds} \right) f(s), \quad (\text{H11})$$

which corresponds to multiplication by  $\Delta(\Omega_m) - \omega$  in frequency space. Define  $g_1(s)$  analogously by replacing  $f$  with  $g$ . The benefit of doing this is that the following relation now holds for all  $s$ ,

$$f_1(s) \approx g_1(s - \tau)e^{i[\Delta(\Omega_m)\tau + \delta]} + g_1^*(-s - \tau)e^{-i[\Delta(\Omega_m)\tau + \delta]}. \quad (\text{H12})$$

The underlying idea is that  $f_1(s)$  is constructed to vanish on the pulse interior and  $g_1(s)$  corresponds to the positive half of  $f_1(s)$ , modulo the dynamical phase. It follows from Eq. (H12) that

$$|\mathcal{F}[f_1(s)](\omega)|^2 = 2|\mathcal{F}[g_1(s)](\omega)|^2 + \text{oscillatory}, \quad (\text{H13})$$

where the omitted terms are oscillatory in  $\tau$  and will be averaged away, except when  $\omega = \Delta(\Omega_m)$ . By using this

equation and dropping the oscillatory terms, the ESD of the original function  $f(s)$  can be expressed as

$$|\mathcal{F}[f(s)](\omega)|^2 = \frac{2|\mathcal{F}[g_1(s)](\omega)|^2}{[\omega - \Delta(\Omega_m)]^2}. \quad (\text{H14})$$

The contribution of the dropped terms when  $\omega = \Delta(\Omega_m)$  is irrelevant since the spectrum anyway diverges there.

We may factor  $g_1(s)$  into  $b_1(s)e^{i\theta(s)}$  where

$$b_1(s) := [\nu(s) - \Delta(\Omega_m)]b(s) + i\frac{db(s)}{ds}, \quad (\text{H15})$$

$$\nu(s) := \frac{d\theta(s)}{ds} = \Delta(\Omega_m \mathcal{R}(s)). \quad (\text{H16})$$

Notice that  $b_1(-\infty) = 0$  because the first term of Eq. (H15) vanishes due to  $\nu(-\infty) = \Delta(\Omega_m)$  and the second term vanishes in either limit  $s \rightarrow \pm\infty$ . This is consistent with the interpretation that  $g_1(s)$  corresponds to the positive half of  $f_1(s)$ . Further, if the matrix element is zero in the bare basis, the second term also vanishes as  $s \rightarrow \infty$  because  $b(\infty) = 0$ . When this is the case,  $b_1(s)$  acts as a finite window for the chirp  $e^{i\theta(s)}$ , and we refer to  $g_1(s)$  as the *first ramp chirplet*. Because the support of  $g_1(s)$  is effectively finite, its Fourier transform is readily computable numerically.

Otherwise, if the matrix element is nonzero in the bare basis, e.g. when  $i = 0$ ,  $j = 1$  and  $k = 0$ , then  $g_1(s)$  remains finite for positive  $s$ . We can play the same trick again and define

$$f_2(s) := \left( \Delta(0) + i\frac{d}{ds} \right) f_1(s), \quad (\text{H17})$$

likewise for  $g_2(s)$ . Factoring  $g_2(s)$  into  $b_2(s)e^{i\theta(s)}$  yields

$$b_2(s) := [\nu(s) - \Delta(0)]b_1(s) + i\frac{db_1(s)}{ds} \quad (\text{H18})$$

$$= C_0(s)b(s) + C_1(s)\frac{db(s)}{ds} - \frac{d^2b(s)}{ds^2}, \quad (\text{H19})$$

where

$$C_0(s) := [\nu(s) - \Delta(0)][\nu(s) - \Delta(\Omega_m)] + i\frac{d\nu(s)}{ds}, \quad (\text{H20})$$

$$C_1(s) := i[2\nu(s) - \Delta(0) - \Delta(\Omega_m)]. \quad (\text{H21})$$

The window  $b_2(s)$  is effectively finite since  $C_0(\pm\infty) = 0$ , so we call  $g_2(s)$  the *second ramp chirplet*. The ESD of  $f(s)$  is then recovered as

$$|\mathcal{F}[f(s)](\omega)|^2 = \frac{2|\mathcal{F}[g_2(s)](\omega)|^2}{[\omega - \Delta(0)]^2[\omega - \Delta(\Omega_m)]^2}. \quad (\text{H22})$$

As expected, if the matrix element does not asymptotically vanish, its ESD has poles at both the bare and Stark-shifted transition frequencies.

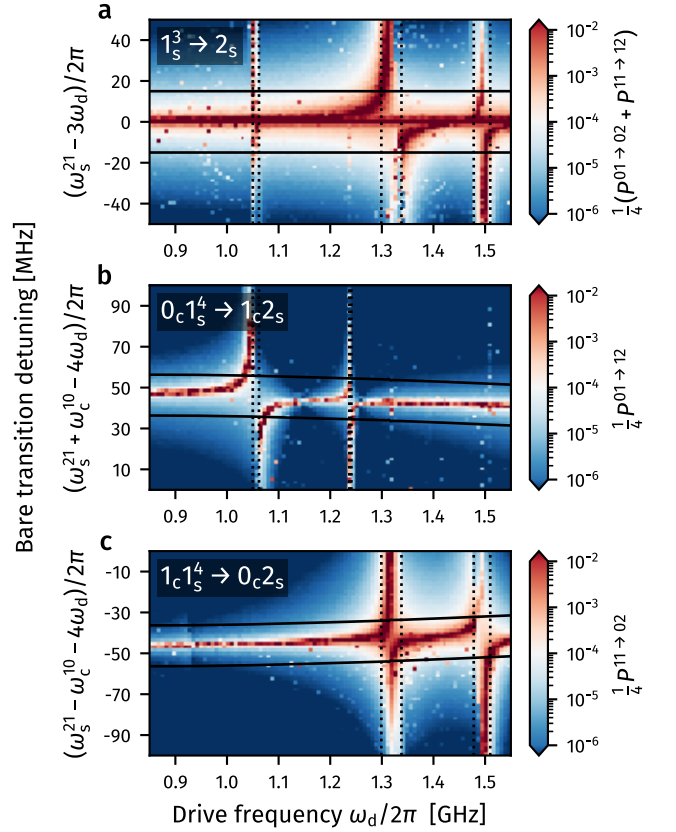


FIG. 20: Spectator-fluxonium  $1 \rightarrow 2$  error induced by driving (a) near the third subharmonic of its transition frequency, (b) near the fourth subharmonic and assisted by a control-qubit *excitation* and (c) near the fourth subharmonic and assisted by a control-qubit *decay*. The vertical axis is the detuning between the bare transition frequency and a drive harmonic. **Solid** black lines define a  $\pm 15$  MHz detuning window in (a) and a  $\pm 10$  MHz window centered on the Stark-shifted transition frequency in (b, c). **Dotted** black lines reproduce the collision windows from Table II for  $\Delta p = 0.8$ .

### Appendix I: Extra control–spectator transitions

In this appendix, we only consider the case where the CR drive amplitude induces  $\Delta p = 0.8$  and the control and spectator qubits are coupled with a strength of  $J/2\pi = 100$  MHz, consistent with Section IV E.

Beyond the errors discussed in the main text, we present here the leakage error induced when driving near the third subharmonic of a spectator's  $1 \rightarrow 2$  transition frequency, see Fig. 20a. These errors are almost identical to Fig. 10a, where a *target's*  $1 \rightarrow 2$  transition is driven. From this similarity, we assert that even though the spectator's qubit transition is not resonantly driven by the CR drive, its leakage probability is the same as if it were a resonantly driven target qubit. Figures 20b and 20c shows the  $01 \rightarrow 12$  and  $11 \rightarrow 02$  leakage errors, respec-

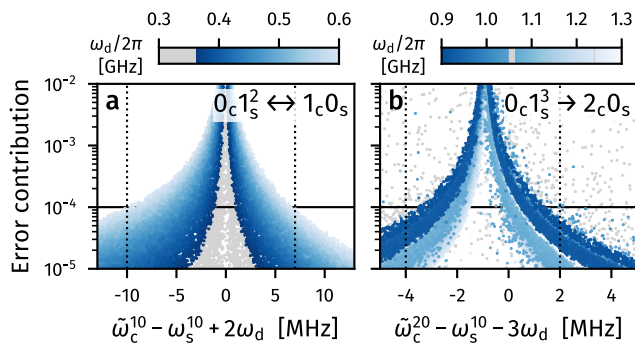


FIG. 21: (a) iSWAP error and (b) control-qubit leakage error assisted by a spectator decay when the detuning (horizontal axis) between the Stark-shifted transition frequency and (a) the second or (b) third drive harmonic is small. The vertical axis in (a) is  $\frac{1}{5}(P^{01 \rightarrow 10} + P^{10 \rightarrow 01})$  and in (b)  $\frac{1}{4}P^{01 \rightarrow 20}$ . The **blue shading** of the scatter points corresponds to the color bar above. The extracted collision bounds (**dotted vertical**) are: (a)  $(-10$  to  $+7)$  MHz and (b)  $(-4$  to  $+2)$  MHz.

tively, induced when driving near the fourth subharmonic of the transition frequencies. These plots are similar to Figs. 11a and 11b, except the figures in the main text correspond to a larger drive amplitude inducing  $\Delta p = 1.0$ . As expected, a smaller amplitude leads to narrower error peaks. Therefore, the  $\pm 10$  MHz collision bounds centered on the Stark-shifted transition frequency are the worst-case values, applicable when the drive amplitude must be increased beyond inducing  $\Delta p = 0.8$  to detune the resonance from occurring on the pulse plateau.

Driving near the second subharmonic of the  $01 \rightarrow 10$  frequency can induce iSWAP-like errors, see Fig. 21a. However, its collision bounds,  $(-10$  to  $+7)$  MHz, are not very large and the spectator frequency needs to be larger than around 1 GHz to satisfy this resonance condition. In the same vein, driving near the third subharmonic of the  $01 \rightarrow 20$  transition frequency can induce leakage, see Fig. 21b, but this resonance is narrow,  $(-4$  to  $+2)$  MHz, and requires a drive over 0.9 GHz. Because of the narrow bounds and high qubit frequencies involved, these two collisions were excluded from the final collision model.

## Appendix J: Target-qubit frequency allocation

The target-qubit parameters of Table IV are determined by minimizing the collision probability in one vertex neighborhood of a control qubit. We fix the nominal control-qubit parameters at  $E_{J,c}/2\pi = 4.0$  GHz,  $E_{C,c}/2\pi = 1.2$  GHz and  $E_{L,c}/2\pi = 0.4$  GHz, and the nominal target-qubit charging and inductive energies at  $E_{C,t}/2\pi = E_{L,t}/2\pi = 1$  GHz. Hence, we optimize over only the nominal target-qubit Josephson energies. The charging energies of the target qubits are chosen to be lower than that of the control qubit since we expect the capacitive loading on the targets to be greater in the heavy-hex lattice due to their higher neighbor count. The nominal inductive energy of the target qubits is set to ensure their qubit frequencies span 0.4 GHz to 1.0 GHz as  $E_{J,t}/2\pi$  varies from 3 GHz to 5 GHz.

When calculating the collision probability of one vertex neighborhood, we consider only collisions involving the qubit frequencies, corresponding to types 1, 8 and 9 of Table III. Additionally, any realized qubit frequency over 1 GHz is also considered unacceptable. In this simplified model, we represent the frequency detunings of the collisions as correlated Gaussian random variables, with their standard deviations calculated from first-order perturbation theory. Accordingly, the probability of *simultaneous* collisions is given by the integral of a multivariate Gaussian over a hyperrectangle. This can be computed with high numerical accuracy using the Genz algorithm, implemented in SciPy as `scipy.stats.multivariate_normal.cdf` (available since version 1.0.0) [129, 130]. The probability of *one or more* collisions is then computed using the inclusion-exclusion principle, which is tractable for up to roughly 10 random variables [131]. Compared to Section IV F, we use a more precise method here to calculate the zero-collision yield such that the objective function remains smooth even in the low-disorder regime.

In the low-disorder regime, each target qubit has a unique frequency assignment, see Fig. 22. However, as the disorder increases, the distinct frequencies spread and eventually coalesce, collapsing into a single nominal frequency when the RSD is at 10%. Since the optimal allocation in the low-disorder regime remains valid up to modest RSD values (around 3%), we take these to define the ideal target-qubit parameters in Table IV

- 
- [1] J. Koch, T. M. Yu, J. Gambetta, A. A. Houck, D. I. Schuster, J. Majer, A. Blais, M. H. Devoret, S. M. Girvin, and R. J. Schoelkopf, Charge-insensitive qubit design derived from the Cooper pair box, *Physical Review A* **76**, 042319 (2007).
- [2] M. AbuGhanem, Superconducting quantum computers: Who is leading the future?, *EPJ Quantum Technology* **12**, 102 (2025).
- [3] D. C. McKay, I. Hincks, E. J. Pritchett, M. Car-

- roll, L. C. G. Govia, and S. T. Merkel, Benchmarking Quantum Processor Performance at Scale (2023), arXiv:2311.05933 [quant-ph].
- [4] R. Acharya *et al.*, Quantum error correction below the surface code threshold, *Nature* **638**, 920 (2025).
- [5] A. G. Fowler, M. Mariantoni, J. M. Martinis, and A. N. Cleland, Surface codes: Towards practical large-scale quantum computation, *Physical Review A* **86**, 032324 (2012).

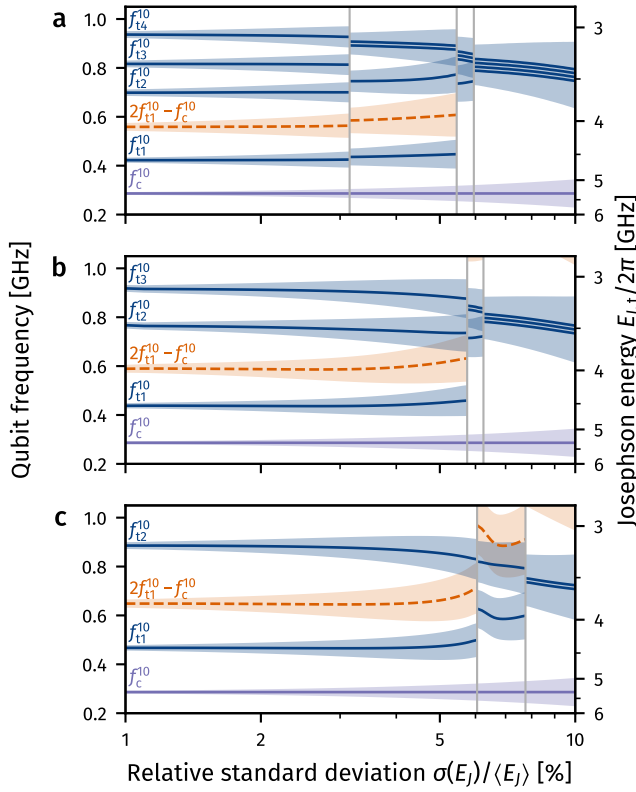


FIG. 22: Optimal nominal qubit frequencies (**solid blue** for the targets and **solid violet** for the fixed control) as a function of the Josephson-energy RSD that minimize the collision probability within a single vertex neighborhood of a control qubit in the (a) square lattice, (b) hexagonal lattice and (c) heavy-hexagonal lattice. Target-qubit frequencies should also avoid collision type 9 (**dashed orange**) from Table III. The **shaded** area around each line covers the region within one standard deviation of the mean. Discontinuities in the optimal allocation (**vertical lines**) occur when multiple frequencies overlap and merge with increasing RSD. When they merge, the nominal frequencies are artificially offset to visualize their multiplicity. A conversion to the corresponding target-qubit Josephson energy is shown on the right spine. The other qubit parameters are the same as in Table IV.

[6] Y. Zhao *et al.*, Realization of an Error-Correcting Surface Code with Superconducting Qubits, *Physical Review Letters* **129**, 030501 (2022).  
 [7] L. Abdurakhimov *et al.*, Technology and Performance Benchmarks of IQM’s 20-Qubit Quantum Computer (2024), arXiv:2408.12433 [quant-ph].  
 [8] C. Gidney and M. Ekerå, How to factor 2048 bit RSA integers in 8 hours using 20 million noisy qubits, *Quantum* **5**, 433 (2021).  
 [9] J. Lee, D. W. Berry, C. Gidney, W. J. Huggins, J. R. McClean, N. Wiebe, and R. Babbush, Even More Efficient Quantum Computations of Chemistry Through Tensor Hypercontraction, *PRX Quantum* **2**, 030305 (2021).  
 [10] A. M. Dalzell, S. McArdle, M. Berta, P. Bienias, C.-

F. Chen, A. Gilyén, C. T. Hann, M. J. Kastoryano, E. T. Khabiboulline, A. Kubica, G. Salton, S. Wang, and F. G. S. L. Brandão, Quantum algorithms: A survey of applications and end-to-end complexities, <https://arxiv.org/abs/2310.03011v2> (2023).  
 [11] S. Bravyi, O. Dial, J. M. Gambetta, D. Gil, and Z. Nazario, The future of quantum computing with superconducting qubits, *Journal of Applied Physics* **132**, 160902 (2022).  
 [12] S. Bravyi, A. W. Cross, J. M. Gambetta, D. Maslov, P. Rall, and T. J. Yoder, High-threshold and low-overhead fault-tolerant quantum memory, *Nature* **627**, 778 (2024).  
 [13] M. Mohseni *et al.*, How to Build a Quantum Supercomputer: Scaling from Hundreds to Millions of Qubits (2025), arXiv:2411.10406 [quant-ph].  
 [14] A. Gyenis, P. S. Mundada, A. Di Paolo, T. M. Hazard, X. You, D. I. Schuster, J. Koch, A. Blais, and A. A. Houck, Experimental Realization of a Protected Superconducting Circuit Derived from the  $0-\pi$  Qubit, *PRX Quantum* **2**, 010339 (2021).  
 [15] E. Hyppä *et al.*, Unimon qubit, *Nature Communications* **13**, 6895 (2022).  
 [16] R. A. Mencia, W.-J. Lin, H. Cho, M. G. Vavilov, and V. E. Manucharyan, Integer Fluxonium Qubit, *PRX Quantum* **5**, 040318 (2024).  
 [17] W. Ardatti, S. Léger, S. Kumar, V. N. Suresh, D. Nicolas, C. Mori, F. D’Esposito, T. Vakhtel, O. Buisson, Q. Ficheux, and N. Roch, Using Bifluxon Tunneling to Protect the Fluxonium Qubit, *Physical Review X* **14**, 041014 (2024).  
 [18] R. Rousseau *et al.*, Enhancing dissipative cat qubit protection by squeezing (2025), arXiv:2502.07892 [quant-ph].  
 [19] H. Putterman *et al.*, Hardware-efficient quantum error correction via concatenated bosonic qubits, *Nature* **638**, 927 (2025).  
 [20] H. Levine *et al.*, Demonstrating a Long-Coherence Dual-Rail Erasure Qubit Using Tunable Transmons, *Physical Review X* **14**, 011051 (2024).  
 [21] W. Huang *et al.*, Logical multi-qubit entanglement with dual-rail superconducting qubits, *Nature Physics* , 1 (2026).  
 [22] V. E. Manucharyan, J. Koch, L. I. Glazman, and M. H. Devoret, Fluxonium: Single Cooper-Pair Circuit Free of Charge Offsets, *Science* **326**, 113 (2009).  
 [23] L. B. Nguyen, G. Koolstra, Y. Kim, A. Morvan, T. Chistolini, S. Singh, K. N. Nesterov, C. Jünger, L. Chen, Z. Pedramrazi, B. K. Mitchell, J. M. Kreikebaum, S. Puri, D. I. Santiago, and I. Siddiqi, Blueprint for a High-Performance Fluxonium Quantum Processor, *PRX Quantum* **3**, 037001 (2022).  
 [24] H. Sun, F. Wu, H.-S. Ku, X. Ma, J. Qin, Z. Song, T. Wang, G. Zhang, J. Zhou, Y. Shi, H.-H. Zhao, and C. Deng, Characterization of Loss Mechanisms in a Fluxonium Qubit, *Physical Review Applied* **20**, 034016 (2023).  
 [25] Z.-T. Zhuang, D. Rosenstock, B.-J. Liu, A. Somoroff, V. E. Manucharyan, and C. Wang, Non-Markovian relaxation spectroscopy of fluxonium qubits, *Nature Communications* 10.1038/s41467-026-69910-2 (2026).  
 [26] G. Zhu, D. G. Ferguson, V. E. Manucharyan, and J. Koch, Circuit QED with fluxonium qubits: Theory of the dispersive regime, *Physical Review B* **87**, 024510

- (2013).
- [27] T. V. Stefanski, F. Yilmaz, E. Y. Huang, M. F. S. Zwanenburg, S. Singh, S. Wang, L. J. Splitthoff, and C. K. Andersen, Improved fluxonium readout through dynamic flux pulsing (2024), arXiv:2411.13437.
- [28] M. F. S. Zwanenburg, S. Singh, E. Y. Huang, F. Yilmaz, T. V. Stefanski, J. Hu, P. Kumaravadivel, and C. K. Andersen, Single-qubit gates beyond the rotating-wave approximation for strongly anharmonic low-frequency qubits, *Physical Review Research* **7**, 043290 (2025).
- [29] D. A. Rower, L. Ding, H. Zhang, M. Hays, J. An, P. M. Harrington, I. T. Rosen, J. M. Gertler, T. M. Hazard, B. M. Niedzielski, M. E. Schwartz, S. Gustavsson, K. Serniak, J. A. Grover, and W. D. Oliver, Suppressing Counter-Rotating Errors for Fast Single-Qubit Gates with Fluxonium, *PRX Quantum* **5**, 040342 (2024).
- [30] A. Somoroff, Q. Ficheux, R. A. Mencia, H. Xiong, R. Kuzmin, and V. E. Manucharyan, Millisecond Coherence in a Superconducting Qubit, *Physical Review Letters* **130**, 267001 (2023).
- [31] L. Ding, M. Hays, Y. Sung, B. Kannan, J. An, A. Di Paolo, A. H. Karamlou, T. M. Hazard, K. Azar, D. K. Kim, B. M. Niedzielski, A. Melville, M. E. Schwartz, J. L. Yoder, T. P. Orlando, S. Gustavsson, J. A. Grover, K. Serniak, and W. D. Oliver, High-Fidelity, Frequency-Flexible Two-Qubit Fluxonium Gates with a Transmon Coupler, *Physical Review X* **13**, 031035 (2023).
- [32] W.-J. Lin, H. Cho, Y. Chen, M. G. Vavilov, C. Wang, and V. E. Manucharyan, 24 Days-Stable CNOT Gate on Fluxonium Qubits with Over 99.9% Fidelity, *PRX Quantum* **6**, 010349 (2025).
- [33] R. Li, K. Kubo, Y. Ho, Z. Yan, Y. Nakamura, and H. Goto, Realization of High-Fidelity CZ Gate Based on a Double-Transmon Coupler, *Physical Review X* **14**, 041050 (2024).
- [34] F. Marxer *et al.*, Above 99.9% Fidelity Single-Qubit Gates, Two-Qubit Gates, and Readout in a Single Superconducting Quantum Device (2025), arXiv:2508.16437 [quant-ph].
- [35] K. C. Miao *et al.*, Overcoming leakage in quantum error correction, *Nature Physics* **19**, 1780 (2023).
- [36] L. B. Nguyen, Y.-H. Lin, A. Somoroff, R. Mencia, N. Grabon, and V. E. Manucharyan, High-Coherence Fluxonium Qubit, *Physical Review X* **9**, 041041 (2019).
- [37] M. D. Reed, B. R. Johnson, A. A. Houck, L. DiCarlo, J. M. Chow, D. I. Schuster, L. Frunzio, and R. J. Schoelkopf, Fast reset and suppressing spontaneous emission of a superconducting qubit, *Applied Physics Letters* **96**, 203110 (2010).
- [38] I. N. Moskalenko, I. A. Simakov, N. N. Abramov, A. A. Grigorev, D. O. Moskalev, A. A. Pishchimova, N. S. Smirnov, E. V. Zikiy, I. A. Rodionov, and I. S. Besedin, High fidelity two-qubit gates on fluxoniums using a tunable coupler, *npj Quantum Information* **8**, 1 (2022).
- [39] H. Zhang, C. Ding, D. Weiss, Z. Huang, Y. Ma, C. Guinn, S. Sussman, S. P. Chitta, D. Chen, A. A. Houck, J. Koch, and D. I. Schuster, Tunable Inductive Coupler for High-Fidelity Gates Between Fluxonium Qubits, *PRX Quantum* **5**, 020326 (2024).
- [40] P. Zhao, G. Zhao, S. Li, C. Zha, M. Gong, and X. Zhu, Scalable fluxonium qubit architecture with tunable interactions between non-computational levels (2025), arXiv:2504.09888 [quant-ph].
- [41] A. Chakraborty, B. Bhandari, D. D. Briseño-Colunga, N. Stevenson, Z. Pedramrazi, C.-H. Liu, D. I. Santiago, I. Siddiqi, J. Dressel, and A. N. Jordan, Tunable Superconducting Quantum Interference Device Coupler for Fluxonium Qubits (2025), arXiv:2508.16907 [quant-ph].
- [42] I. A. Simakov, G. S. Mazhorin, I. N. Moskalenko, N. N. Abramov, A. A. Grigorev, D. O. Moskalev, A. A. Pishchimova, N. S. Smirnov, E. V. Zikiy, I. A. Rodionov, and I. S. Besedin, Coupler Microwave-Activated Controlled-Phase Gate on Fluxonium Qubits, *PRX Quantum* **4**, 040321 (2023).
- [43] S. Singh, E. Y. Huang, J. Hu, F. Yilmaz, M. F. S. Zwanenburg, P. Kumaravadivel, S. Wang, T. V. Stefanski, and C. K. Andersen, Fast microwave-driven two-qubit gates between fluxonium qubits with a transmon coupler, *Physical Review Applied* **25**, 024020 (2026).
- [44] E. L. Rosenfeld, C. T. Hann, D. I. Schuster, M. H. Matheny, and A. A. Clerk, High-Fidelity Two-Qubit Gates between Fluxonium Qubits with a Resonator Coupler, *PRX Quantum* **5**, 040317 (2024).
- [45] N. D. Dimitrov, C. Wang, V. E. Manucharyan, and M. G. Vavilov, Cross-Resonant Gates in Hybrid Fluxonium-Transmon Systems (2025), arXiv:2509.07935 [quant-ph].
- [46] A. A. Kugut, G. S. Mazhorin, and I. A. Simakov, Interaction-Resilient Scalable Fluxonium Architecture with All-Microwave Gates (2025), arXiv:2512.21189 [quant-ph].
- [47] F. Lange, L. Heunisch, H. Fehske, D. P. DiVincenzo, and M. J. Hartmann, Cross-talk in superconducting qubit lattices with tunable couplers—comparing transmon and fluxonium architectures, *Quantum Science and Technology* **11**, 015020 (2025).
- [48] A. Ciani, B. M. Varbanov, N. Jolly, C. K. Andersen, and B. M. Terhal, Microwave-activated gates between a fluxonium and a transmon qubit, *Physical Review Research* **4**, 043127 (2022).
- [49] E. Dogan, D. Rosenstock, L. Le Guevel, H. Xiong, R. A. Mencia, A. Somoroff, K. N. Nesterov, M. G. Vavilov, V. E. Manucharyan, and C. Wang, Two-Fluxonium Cross-Resonance Gate, *Physical Review Applied* **20**, 024011 (2023).
- [50] F. Bao *et al.*, Fluxonium: An Alternative Qubit Platform for High-Fidelity Operations, *Physical Review Letters* **129**, 010502 (2022).
- [51] X. Ma *et al.*, Native Approach to Controlled-Z Gates in Inductively Coupled Fluxonium Qubits, *Physical Review Letters* **132**, 060602 (2024).
- [52] V. D. Moreno, N. D. Dimitrov, V. E. Manucharyan, and M. G. Vavilov, CNOT gates in inductively coupled multi-fluxonium systems (2025), arXiv:2512.11756 [quant-ph].
- [53] Q. Ficheux, L. B. Nguyen, A. Somoroff, H. Xiong, K. N. Nesterov, M. G. Vavilov, and V. E. Manucharyan, Fast Logic with Slow Qubits: Microwave-Activated Controlled-Z Gate on Low-Frequency Fluxoniums, *Physical Review X* **11**, 021026 (2021).
- [54] H. Xiong, Q. Ficheux, A. Somoroff, L. B. Nguyen, E. Dogan, D. Rosenstock, C. Wang, K. N. Nesterov, M. G. Vavilov, and V. E. Manucharyan, Arbitrary controlled-phase gate on fluxonium qubits using differential ac Stark shifts, *Physical Review Research* **4**, 023040 (2022).

- [55] K. N. Nesterov, Q. Ficheux, V. E. Manucharyan, and M. G. Vavilov, Proposal for Entangling Gates on Fluxonium Qubits via a Two-Photon Transition, *PRX Quantum* **2**, 020345 (2021).
- [56] C. Rigetti, A. Blais, and M. Devoret, Protocol for Universal Gates in Optimally Biased Superconducting Qubits, *Physical Review Letters* **94**, 240502 (2005).
- [57] S. Sheldon, E. Magesan, J. M. Chow, and J. M. Gambetta, Procedure for systematically tuning up crosstalk in the cross-resonance gate, *Physical Review A* **93**, 060302 (2016).
- [58] K. Heya and N. Kanazawa, Cross-Cross Resonance Gate, *PRX Quantum* **2**, 040336 (2021).
- [59] K. X. Wei, I. Lauer, E. Pritchett, W. Shanks, D. C. McKay, and A. Javadi-Abhari, Native Two-Qubit Gates in Fixed-Coupling, Fixed-Frequency Transmons Beyond Cross-Resonance Interaction, *PRX Quantum* **5**, 020338 (2024).
- [60] L. B. Nguyen, Y. Kim, A. Hashim, N. Goss, B. Marinelli, B. Bhandari, D. Das, R. K. Naik, J. M. Kreikebaum, A. N. Jordan, D. I. Santiago, and I. Siddiqi, Programmable Heisenberg interactions between Floquet qubits, *Nature Physics* , 1 (2024).
- [61] J. M. Chow, J. M. Gambetta, E. Magesan, D. W. Abraham, A. W. Cross, B. R. Johnson, N. A. Masluk, C. A. Ryan, J. A. Smolin, S. J. Srinivasan, and M. Steffen, Implementing a strand of a scalable fault-tolerant quantum computing fabric, *Nature Communications* **5**, 4015 (2014).
- [62] R. Barends *et al.*, Superconducting quantum circuits at the surface code threshold for fault tolerance, *Nature* **508**, 500 (2014).
- [63] S. Krinner, N. Lacroix, A. Remm, A. Di Paolo, E. Genois, C. Leroux, C. Hellings, S. Lazar, F. Swiadek, J. Herrmann, G. J. Norris, C. K. Andersen, M. Müller, A. Blais, C. Eichler, and A. Wallraff, Realizing repeated quantum error correction in a distance-three surface code, *Nature* **605**, 669 (2022).
- [64] J. F. Marques, B. M. Varbanov, M. S. Moreira, H. Ali, N. Muthusubramanian, C. Zachariadis, F. Battistel, M. Beekman, N. Haider, W. Vlothuizen, A. Bruno, B. M. Terhal, and L. DiCarlo, Logical-qubit operations in an error-detecting surface code, *Nature Physics* **18**, 80 (2022).
- [65] N. Acharya, R. Armstrong, Y. Balaji, K. G. Crawford, J. C. Gates, P. C. Gow, O. W. Kennedy, R. D. Pothuraju, K. Shahbazi, and C. D. Shelly, Integration of Through-Sapphire Substrate Machining with Superconducting Quantum Processors, *Advanced Materials* **37**, 2411780 (2025).
- [66] T. Ward, R. P. Rundle, R. Bounds, N. Deak, G. Dold, A. Hegde, W. Howard, A. Keyser, G. B. Long, B. Rogers, J. J. Burnett, and B. A. Bell, Echo Cross Resonance gate error budgeting on a superconducting quantum processor (2026), arXiv:2601.20458 [quant-ph].
- [67] L. Ateshian, M. Hays, D. A. Rower, H. Zhang, K. Azar, R. Assouly, L. Ding, M. Gingras, H. Stickler, B. M. Niedzielski, M. E. Schwartz, T. P. Orlando, J. Í.-j. Wang, S. Gustavsson, J. A. Grover, K. Serniak, and W. D. Oliver, Temperature and Magnetic-Field Dependence of Energy Relaxation in a Fluxonium Qubit (2025), arXiv:2507.01175 [quant-ph].
- [68] M. A. Rol, L. Ciorciaro, F. K. Malinowski, B. M. Tarasinski, R. E. Sagastizabal, C. C. Bultink, Y. Salathe, N. Haandbaek, J. Sedivy, and L. DiCarlo, Time-domain characterization and correction of on-chip distortion of control pulses in a quantum processor, *Applied Physics Letters* **116**, 054001 (2020).
- [69] C. Hellings, N. Lacroix, A. Remm, R. Boell, J. Herrmann, S. Lazar, S. Krinner, F. Swiadek, C. K. Andersen, C. Eichler, and A. Wallraff, Calibrating magnetic flux control in superconducting circuits by compensating distortions on timescales from nanoseconds up to tens of microseconds, *Physical Review Research* **7**, 043142 (2025).
- [70] D. Castelvecchi, IBM releases first-ever 1,000-qubit quantum chip, *Nature* **624**, 238 (2023).
- [71] C. Chamberland, G. Zhu, T. J. Yoder, J. B. Hertzberg, and A. W. Cross, Topological and Subsystem Codes on Low-Degree Graphs with Flag Qubits, *Physical Review X* **10**, 011022 (2020).
- [72] J. B. Hertzberg, E. J. Zhang, S. Rosenblatt, E. Magesan, J. A. Smolin, J.-B. Yau, V. P. Adiga, M. Sandberg, M. Brink, J. M. Chow, and J. S. Orcutt, Laser-annealing Josephson junctions for yielding scaled-up superconducting quantum processors, *npj Quantum Information* **7**, 1 (2021).
- [73] A. Morvan, L. Chen, J. M. Larson, D. I. Santiago, and I. Siddiqi, Optimizing frequency allocation for fixed-frequency superconducting quantum processors, *Physical Review Research* **4**, 023079 (2022).
- [74] W. C. Smith, A. Kou, U. Vool, I. M. Pop, L. Frunzio, R. J. Schoelkopf, and M. H. Devoret, Quantization of inductively shunted superconducting circuits, *Physical Review B* **94**, 144507 (2016).
- [75] A. Kandala, K. X. Wei, S. Srinivasan, E. Magesan, S. Carnevale, G. A. Keefe, D. Klaus, O. Dial, and D. C. McKay, Demonstration of a High-Fidelity cnot Gate for Fixed-Frequency Transmons with Engineered ZZ Suppression, *Physical Review Letters* **127**, 130501 (2021).
- [76] K. X. Wei, E. Magesan, I. Lauer, S. Srinivasan, D. F. Bogorin, S. Carnevale, G. A. Keefe, Y. Kim, D. Klaus, W. Landers, N. Sundaresan, C. Wang, E. J. Zhang, M. Steffen, O. E. Dial, D. C. McKay, and A. Kandala, Hamiltonian Engineering with Multicolor Drives for Fast Entangling Gates and Quantum Crosstalk Cancellation, *Physical Review Letters* **129**, 060501 (2022).
- [77] W.-J. Lin, H. Cho, Y. Chen, M. G. Vavilov, C. Wang, and V. E. Manucharyan, Verifying the analogy between transversely coupled spin-1/2 systems and inductively-coupled fluxoniums, *New Journal of Physics* **27**, 033012 (2025).
- [78] J. H. Shirley, Solution of the Schrödinger Equation with a Hamiltonian Periodic in Time, *Physical Review* **138**, B979 (1965).
- [79] M. Grifoni and P. Hänggi, Driven quantum tunneling, *Physics Reports* **304**, 229 (1998).
- [80] K. N. Nesterov, C. Wang, V. E. Manucharyan, and M. G. Vavilov, Cnot Gates for Fluxonium Qubits via Selective Darkening of Transitions, *Physical Review Applied* **18**, 034063 (2022).
- [81] N. Sundaresan, I. Lauer, E. Pritchett, E. Magesan, P. Jurcevic, and J. M. Gambetta, Reducing Unitary and Spectator Errors in Cross Resonance with Optimized Rotary Echoes, *PRX Quantum* **1**, 020318 (2020).
- [82] D. C. McKay, C. J. Wood, S. Sheldon, J. M. Chow, and J. M. Gambetta, Efficient Z gates for quantum computing, *Physical Review A* **96**, 022330 (2017).

- [83] P. S. Mundada, A. Gyenis, Z. Huang, J. Koch, and A. A. Houck, Floquet-Engineered Enhancement of Coherence Times in a Driven Fluxonium Qubit, *Physical Review Applied* **14**, 054033 (2020).
- [84] Z. Huang, P. S. Mundada, A. Gyenis, D. I. Schuster, A. A. Houck, and J. Koch, Engineering Dynamical Sweet Spots to Protect Qubits from  $1/f$  Noise, *Physical Review Applied* **15**, 034065 (2021).
- [85] Z. Wang and A. H. Safavi-Naeini, Quantum control and noise protection of a Floquet  $0 - \pi$  qubit, *Physical Review A* **109**, 042607 (2024).
- [86] T. Abad, Y. Schattner, A. F. Kockum, and G. Johansson, Impact of decoherence on the fidelity of quantum gates leaving the computational subspace, *Quantum* **9**, 1684 (2025).
- [87] H. Zhang, S. Chakram, T. Roy, N. Earnest, Y. Lu, Z. Huang, D. K. Weiss, J. Koch, and D. I. Schuster, Universal Fast-Flux Control of a Coherent, Low-Frequency Qubit, *Physical Review X* **11**, 011010 (2021).
- [88] V. Tripathi, M. Khezri, and A. N. Korotkov, Operation and intrinsic error budget of a two-qubit cross-resonance gate, *Physical Review A* **100**, 012301 (2019).
- [89] M. Malekakhlagh, E. Magesan, and D. C. McKay, First-principles analysis of cross-resonance gate operation, *Physical Review A* **102**, 042605 (2020).
- [90] M. Ware, B. R. Johnson, J. M. Gambetta, T. A. Ohki, J. M. Chow, and B. L. T. Plourde, Cross-resonance interactions between superconducting qubits with variable detuning (2019), arXiv:1905.11480 [quant-ph].
- [91] J. M. Chow, A. D. Córcoles, J. M. Gambetta, C. Rigetti, B. R. Johnson, J. A. Smolin, J. R. Rozen, G. A. Keefe, M. B. Rothwell, M. B. Ketchen, and M. Steffen, Simple All-Microwave Entangling Gate for Fixed-Frequency Superconducting Qubits, *Physical Review Letters* **107**, 080502 (2011).
- [92] D. P. Pappas, M. Field, C. J. Kopas, J. A. Howard, X. Wang, E. Lachman, J. Oh, L. Zhou, A. Gold, G. M. Stiehl, K. Yadavalli, E. A. Sete, A. Bestwick, M. J. Kramer, and J. Y. Mutus, Alternating-bias assisted annealing of amorphous oxide tunnel junctions, *Communications Materials* **5**, 150 (2024).
- [93] E. J. Zhang *et al.*, High-performance superconducting quantum processors via laser annealing of transmon qubits, *Science Advances* **8**, eabi6690 (2022).
- [94] N. Muthusubramanian, M. Finkel, P. Duivesteyn, C. Zachariadis, S. L. M. van der Meer, H. M. Veen, M. W. Beekman, T. Stavenga, A. Bruno, and L. DiCarlo, Wafer-scale uniformity of Dolan-bridge and bridgeless Manhattan-style Josephson junctions for superconducting quantum processors, *Quantum Science and Technology* **9**, 025006 (2024).
- [95] F. Wang *et al.*, High-coherence fluxonium qubits manufactured with a wafer-scale-uniformity process, *Physical Review Applied* **23**, 044064 (2025).
- [96] A. A. Pishchimova, N. S. Smirnov, D. A. Ezenkova, E. A. Krivko, E. V. Zikiy, D. O. Moskalev, A. I. Ivanov, N. D. Korshakov, and I. A. Rodionov, Improving Josephson junction reproducibility for superconducting quantum circuits: Junction area fluctuation, *Scientific Reports* **13**, 6772 (2023).
- [97] A. Osman, J. Simon, A. Bengtsson, S. Kosen, P. Krantz, D. P. Lozano, M. Scigliuzzo, P. Delsing, J. Bylander, and A. Fadavi Roudsari, Simplified Josephson-junction fabrication process for reproducibly high-performance superconducting qubits, *Applied Physics Letters* **118**, 064002 (2021).
- [98] K. N. Nesterov and I. V. Pechenezhskiy, Measurement-induced state transitions in dispersive qubit-readout schemes, *Physical Review Applied* **22**, 064038 (2024).
- [99] C. M. Le, R. Akashi, and S. Tsuneyuki, Defining a well-ordered Floquet basis by the average energy, *Physical Review A* **102**, 042212 (2020).
- [100] C. M. Le, R. Akashi, and S. Tsuneyuki, Missing quantum number of Floquet states, *Physical Review A* **105**, 052213 (2022).
- [101] G. Zheng, S. Lieu, E. L. Rosenfeld, K. Noh, and C. T. Hann, Cross-resonance control of an oscillator with an auxiliary fluxonium qubit, *Physical Review Applied* **23**, 024067 (2025).
- [102] T. Abad, J. Fernández-Pendás, A. Frisk Kockum, and G. Johansson, Universal Fidelity Reduction of Quantum Operations from Weak Dissipation, *Physical Review Letters* **129**, 150504 (2022).
- [103] S. N. Shevchenko, S. Ashhab, and F. Nori, Landau-Zener-Stückelberg interferometry, *Physics Reports* **492**, 1 (2010).
- [104] H. Bombin and M. A. Martin-Delgado, Optimal resources for topological two-dimensional stabilizer codes: Comparative study, *Physical Review A* **76**, 012305 (2007).
- [105] D. Horsman, A. G. Fowler, S. Devitt, and R. V. Meter, Surface code quantum computing by lattice surgery, *New Journal of Physics* **14**, 123011 (2012).
- [106] Y. Tomita and K. M. Svore, Low-distance surface codes under realistic quantum noise, *Physical Review A* **90**, 062320 (2014).
- [107] M. McEwen, D. Bacon, and C. Gidney, Relaxing Hardware Requirements for Surface Code Circuits using Time-dynamics, *Quantum* **7**, 1172 (2023).
- [108] A. Eickbusch *et al.*, Demonstration of dynamic surface codes, *Nature Physics* , 1 (2025).
- [109] C. Benito, E. López, B. Peropadre, and A. Bermudez, Comparative study of quantum error correction strategies for the heavy-hexagonal lattice, *Quantum* **9**, 1623 (2025).
- [110] A. Patterson, J. Rahamim, T. Tsunoda, P. Spring, S. Jebari, K. Ratter, M. Mergenthaler, G. Tancredi, B. Vlastakis, M. Esposito, and P. Leek, Calibration of a Cross-Resonance Two-Qubit Gate Between Directly Coupled Transmons, *Physical Review Applied* **12**, 064013 (2019).
- [111] F. Motzoi, J. M. Gambetta, P. Rebentrost, and F. K. Wilhelm, Simple Pulses for Elimination of Leakage in Weakly Nonlinear Qubits, *Physical Review Letters* **103**, 110501 (2009).
- [112] B. Li, T. Calarco, and F. Motzoi, Experimental error suppression in Cross-Resonance gates via multi-derivative pulse shaping, *npj Quantum Information* **10**, 1 (2024).
- [113] E. Hyyppä, A. Vepsäläinen, M. Papič, C. F. Chan, S. Inel, A. Landra, W. Liu, J. Luus, F. Marxer, C. Ockeloen-Korppi, S. Orbell, B. Tarasinski, and J. Heinsoo, Reducing Leakage of Single-Qubit Gates for Superconducting Quantum Processors Using Analytical Control Pulse Envelopes, *PRX Quantum* **5**, 030353 (2024).
- [114] E. Y. Huang and C. K. Andersen, Data underlying the publication: Exploration of Fluxonium Parameters for

- Capacitive Cross-Resonance Gates, <https://doi.org/10.4121/f74ed890-6fae-4595-933b-1be3d0473fde> (2026).
- [115] E. Y. Huang, Code for Exploration of Fluxonium Parameters for Capacitive Cross-Resonance Gates, <https://github.com/AndersenQubitLab/fluxonium-cross-resonance> (2026).
- [116] B. C. Hall, in *Quantum Theory for Mathematicians*, Graduate Texts in Mathematics, Vol. 267 (Springer, New York, NY, 2013) pp. 279–304.
- [117] D. De Bernardis, P. Pilar, T. Jaako, S. De Liberato, and P. Rabl, Breakdown of gauge invariance in ultrastrong-coupling cavity QED, *Physical Review A* **98**, 053819 (2018).
- [118] M. Roth, F. Hassler, and D. P. DiVincenzo, Optimal gauge for the multimode Rabi model in circuit QED, *Physical Review Research* **1**, 033128 (2019).
- [119] H. Sambe, Steady States and Quasienergies of a Quantum-Mechanical System in an Oscillating Field, *Physical Review A* **7**, 2203 (1973).
- [120] M. V. Berry, in *Geometric Phases In Physics*, edited by A. Shapere and F. Wilczek (World Scientific, Singapore, 1989) pp. 7–28.
- [121] S. Bravyi, D. P. DiVincenzo, and D. Loss, Schrieffer–Wolff transformation for quantum many-body systems, *Annals of Physics* **326**, 2793 (2011).
- [122] F. Wilczek and A. Zee, Appearance of Gauge Structure in Simple Dynamical Systems, *Physical Review Letters* **52**, 2111 (1984).
- [123] U. Vool, I. M. Pop, K. Sliwa, B. Abdo, C. Wang, T. Brecht, Y. Y. Gao, S. Shankar, M. Hatridge, G. Catelani, M. Mirrahimi, L. Frunzio, R. J. Schoelkopf, L. I. Glazman, and M. H. Devoret, Non-Poissonian Quantum Jumps of a Fluxonium Qubit due to Quasiparticle Excitations, *Physical Review Letters* **113**, 247001 (2014).
- [124] T. Morimoto, H. C. Po, and A. Vishwanath, Floquet topological phases protected by time glide symmetry, *Physical Review B* **95**, 195155 (2017).
- [125] L. H. Pedersen, N. M. Møller, and K. Mølmer, Fidelity of quantum operations, *Physics Letters A* **367**, 47 (2007).
- [126] P. Weinberg, M. Bukov, L. D’Alessio, A. Polkovnikov, S. Vajna, and M. Kolodrubetz, Adiabatic Perturbation Theory and Geometry of Periodically-Driven Systems, *Physics Reports* **688**, 1 (2017), arXiv:1606.02229 [cond-mat, physics:quant-ph].
- [127] D. W. Hone, R. Ketzmerick, and W. Kohn, Time-dependent Floquet theory and absence of an adiabatic limit, *Physical Review A* **56**, 4045 (1997).
- [128] M. J. Lighthill, *An Introduction to Fourier Analysis and Generalised Functions*, Cambridge Monographs on Mechanics (Cambridge University Press, Cambridge, 1958).
- [129] A. Genz and G. Trinh, in *Monte Carlo and Quasi-Monte Carlo Methods*, edited by R. Cools and D. Nuyens (Springer International Publishing, Cham, 2016) pp. 289–302.
- [130] P. Virtanen *et al.*, SciPy 1.0: Fundamental algorithms for scientific computing in Python, *Nature Methods* **17**, 261 (2020).
- [131] C. M. Grinstead and J. L. Snell, in *Introduction to Probability* (American Mathematical Society, 2003) 2nd ed.